

# Reservoir characterization of the Roar Field

Report to project: EFP-97 1313/97-005

Ole Valdemar Vejrbæk



# Reservoir characterization of the Roar Field

Report to project: EFP-97 1313/97-005

Ole Valdemar Vejbæk

# Contents

<b>1. Introduction</b>	<b>4</b>
1.1 Seismic data and location.....	5
<b>2. Interpretation of seismic data</b>	<b>7</b>
2.1 Top Jurassic .....	8
2.2 Base Chalk .....	9
2.3 Intra Chalk reflector.....	9
2.4 Top Chalk Reflector .....	10
2.5 Direct hydrocarbon indications.....	10
2.6 Top Maastrichtian .....	12
2.7 Cenozoic reflectors .....	15
2.8 Summary on interpretation of seismic data .....	19
2.9 Depth conversion.....	20
<b>3. Fracture mapping</b>	<b>23</b>
3.1 Summary on fracture mapping .....	26
<b>4. Fluid substitution</b>	<b>29</b>
4.1 General definitions.....	29
4.2 Roar case.....	32
4.3 Summary on fluid substitution.....	34
<b>5. Geostatistical modelling</b>	<b>35</b>
5.1 Porosity simulation.....	36
5.2 Permeability .....	47
5.2.1 Permeability anisotropy.....	50
<b>6. Saturation modelling</b>	<b>54</b>
<b>7. Summary</b>	<b>60</b>
<b>8. References:</b>	<b>61</b>
<b>9. Enclosures</b>	<b>64</b>
9.1 Enclosure 1 .....	65
9.2 Enclosure 2.....	66
9.3 Enclosure 3.....	67
9.4 Enclosure 4.....	68
9.5 Enclosure 5.....	69
9.6 Enclosure 6.....	70
9.7 Enclosure 7.....	71
9.8 Enclosure 8.....	72
9.9 Enclosure 9.....	73
9.10 Enclosure 10.....	74

9.11 Enclosure 11.....	75
9.12 Enclosure 12.....	76



# 1. Introduction

This report constitutes the final contribution to project EFP97 1313/97-005, by GEUS.

The purpose of the report is to present a reservoir characterisation study of the Roar Field (Fig. 1). The characterisation utilises inverted seismic data in conjunction with stochastic simulation, and attempts are made at assessing the importance of fracturing. The study encompasses seismic interpretation, depth conversion, seismic impedance correction by fluid substitution, geostatistical characterisation (of porosity and permeability), and water saturation modelling. The study is concluded with hydrocarbon pore volume calculations.

The Roar field is a low relief domal anticline of Upper Cretaceous and Danian chalk sealed by Paleocene clays and containing a large gas cap (containing condensate) with a thin basal oil zone. The anticline is a broad gentle four way dip closure caused by Cenozoic inversion movements with negligible fracturing (Andersen and Doyle 1990). Three saddle points to the NNE towards the Boje structure, to the NNW towards the Valdemar/N Jens structure and to the SE towards the Tyra Field may all define spill points.

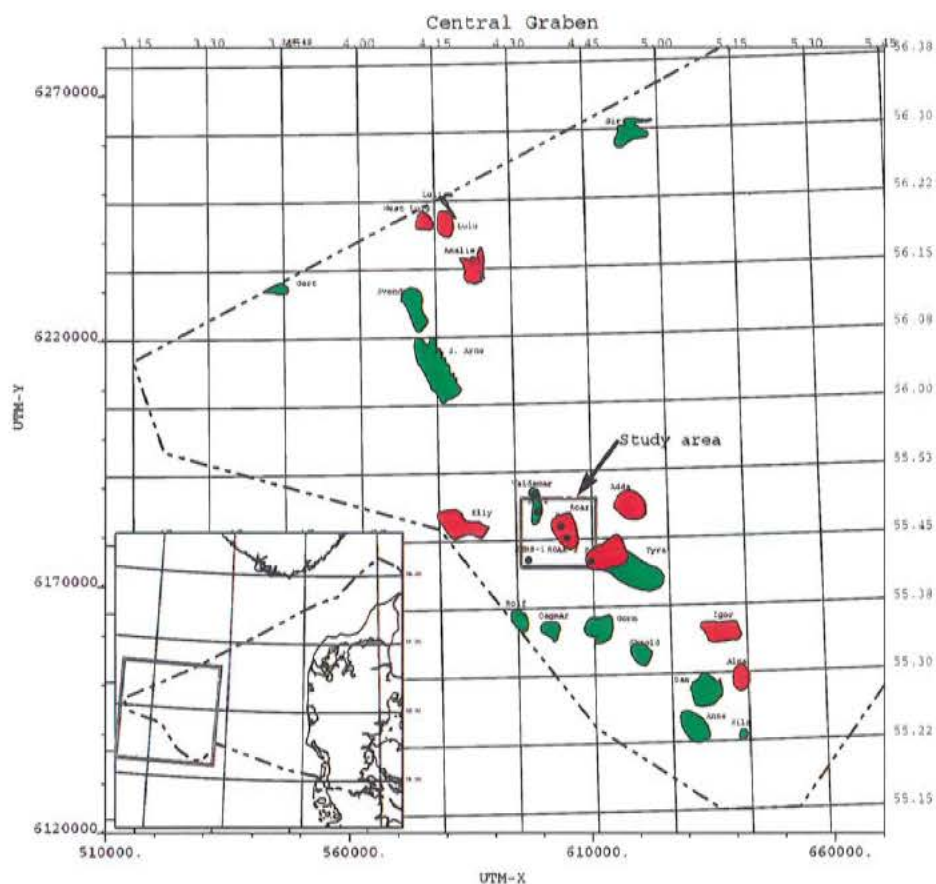


**Figure 1: Location of study area.**

The field was discovered in 1968 and was brought onstream in January 1996 as an unmanned satellite to the Tyra East Platform and is operated by Mærsk Olie og Gas A/S.

Gasproduction in 1996 was 1.33 billion Nm<sup>3</sup>, in 1997 it was 1.96 billion Nm<sup>3</sup> and in 1998 it was 1.46 billion Nm<sup>3</sup> (ENS 1996, 1997, 1998). Oil production was 0.32 million m<sup>3</sup> in 1996, 0.43 million m<sup>3</sup> in 1997 and 0.33 million m<sup>3</sup> in 1998. Water production was 0.01 million m<sup>3</sup> in 1996, 0.10 million m<sup>3</sup> in 1997 and 0.15 million m<sup>3</sup> in 1998, - thus indicating increasing problems with water influx. Two horizontal wells in the northern and southern parts respectively are used to produce gas and condensate at rates 50% higher than anticipated. Neither of these horizontal wells are included in this study. Only two vertical wells constitute the database within the area of the HC accumulation available for this study: The H-1x and the Roar-2 wells. However, the Bo-1, E-2x and Jens-1 wells in the vicinity of the field provide support for seismic interpretation.

The top of the reservoir is located at 1975 m (6480' SS), and the original gas-oil contact (GOC; initial conditions) was located at about 2028m (6775' below KB at 122'). The original OWC was estimated to be located around 2061 m (6762' SS) and 2063 m (6768' SS) in H-1x and Roar-2 respectively, thus suggesting a slight southward tilt as is also supported by seismic mapping (see below). The vertical distance between the free water level and the OWC is, however, quite large as capillary effects on saturation levels are significant over vertical distances in excess of 30 m (100'). Expected reserves have been estimated to 2·10<sup>6</sup> m<sup>3</sup> condensate (low 2, high 3) and 13 billion Nm<sup>3</sup> gas (low 9, high 17; ENS 1996). By January 1997 about 0.32 ·10<sup>6</sup> m<sup>3</sup> condensate and 1.33 billion Nm<sup>3</sup> gas was produced.

## 1.1 Seismic data and location

The main data base besides well data, are 3D seismic data. The data are a subset of a large seismic survey, which was derived by merging of several minor survey. The original survey in the study area consists of the Tyra-Roar-92 and Tyra-Roar-93 surveys. These two survey have the lines oriented East-West, they overlap centrally on the Roar structure with the younger to the north, but have been merged in the Contiguous Area-94 survey which kindly has been released for this public domain study by Mærsk Olie og Gas AS. The data were shot by Simon-Horizon Ltd.

Zero traces are located in the cross line interval from 880 to 908 and in-line interval from 4046 to 4457. This data gap is located along the southwestern edge of the used data set, well outside the Roar field, and thus of little significance.

Line spacing and trace spacing is 12,5 m, and the relationship between lines, traces and UTM-x, UTM-y is uniquely defined by the three point sets inTable 1.

**Table 1: Relationship between line, trace numbers and UTM coordinates.**

Line number	Trace number	UTM-x	UTM-y
4000	950	597868.97	6174998.00
4000	1900	609743.51	6174998.00
5000	950	597874.08	6187503.26

Besides a slight North South skewness in the order of 5 m over 505 m, lines and traces are oriented perfectly North-South, East-West. UTM co-ordinates in this report refer to UTM zone 31 (centre meridian 3°).

The area defined by the values listed in Table 1 are approximately defining the area covered by seismic interpretation, whereas the co-ordinates listed in Table 2 define the location of the quantitative reservoir characterisation study. This area is selected to be as small as possible, but still include the hydrocarbon accumulation and the adjacent water zone of significance for reservoir performance. The co-ordinates in columns 3 and 4 refer to centre points in the grid cells used for geostatistical reservoir characterisation as described later. As the cell size is 25.25.6 m, the total volume should be increased with 12.5 m along all edges in the x and y directions.

**Table 2: Corner points for the geostatistical study volume.**

UTM-x	UTM-y	X-Coord.	Y-Coord.	Trace no.	Line no.
606998.0	6185803.	6312.5	9312.5	1680	4864
600698.3	6185803.	12.5	9312.5	1176	4864
600694.5	6176499.	12.5	12.5	1176	4120
606994.3	6176499.	6312.5	12.5	1680	4120



## 2. Interpretation of seismic data

Seismic interpretation is performed on the first pass inversion result called “reflection strength volume”. This volume is comparable to a true zero-phase deconvolved data-set, and reflectors have accordingly been selected at peaks or troughs (effectively no zero-crossings). Some picks may locally appear to disobey this rule, which may be due to phase changes caused by hydrocarbons (Top Chalk reflector) or because the selected boundary (Base Chalk reflector) is weak and is followed by a close-lying strong reflector.

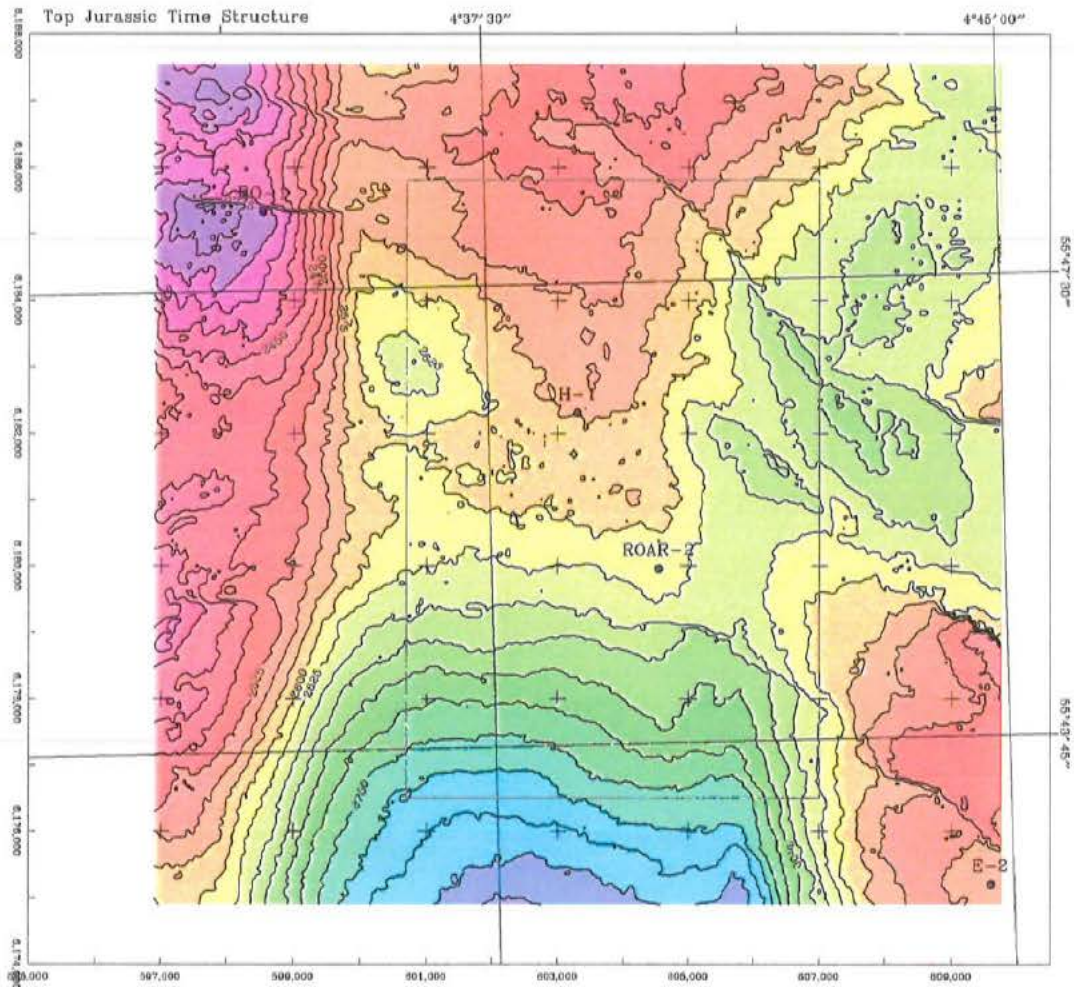


**Figure 2: Top Jurassic time structure map. Box shows location of simulation volume. C. I. is 25 msec.**

Faults are omitted from the automatic contouring to allow continuous definition of the interpreted horizons for the purpose of seismic inversion.

Every 5<sup>th</sup> line and cross-line has been interpreted in entire study area except for the Top Maastrichtian and the DHI reflections. The Top Maastrichtian has only been interpreted in the central parts over the Roar Field, because it has not been used in the seismic inversion. The direct hydrocarbon indicator (DHI) reflections are only traceable in central Roar Field area.

## 2.1 Top Jurassic

The base Cretaceous reflector is selected as a relatively strong peak (downward increase in acoustic impedance) with a clear baselapping reflection configuration above. In minor areas the reflection strength decreases due to side effects from adjacent strong reflections. Structural closure is only found in the north western corner, the North-Jens structure. Northwest Southeast oriented faults with offset of up to 50 msec are clearly seen in the eastern portion of the area (Fig. 2). The North-Jens structure is relatively strongly faulted in several directions (see below).

**Table 3: Tie to local wells (TD depths in brackets; data from Nielsen and Japsen 1991):**

	Bo-1	E-2x	H-1x	Jens-1	Roar-2
Line	4827		4585		4400
Trace	1000		1385		1485
Top Chalk (m)	2024-2245	1958-(2165)	1998.8-(2127)	2344-2617	1988-2476
Top Chalk (twf)	2022-2164	1954-(2104)	1991-(2082)	2301-2440	1885-2277
Top Maast.(m)	<i>(not used)</i>	<i>(not used)</i>	2008.9	<i>(not used)</i>	2016.2
Top Maast.(twf)	<i>(not used)</i>	<i>(not used)</i>	2000 msec	<i>(not used)</i>	2006 msec
Top L. Cret. (m)	2245-2511	Below TD	Below TD	2617-2853	2476-2683
Top L. Cret. (twf)	2164-2375	Below TD	Below TD	2440-2607	2277-2428
T. Chalk (seis.)	2022 msec.		1988 msec.		1982 msec.
B. Chalk (seis.)	2162 msec.				2274 msec.

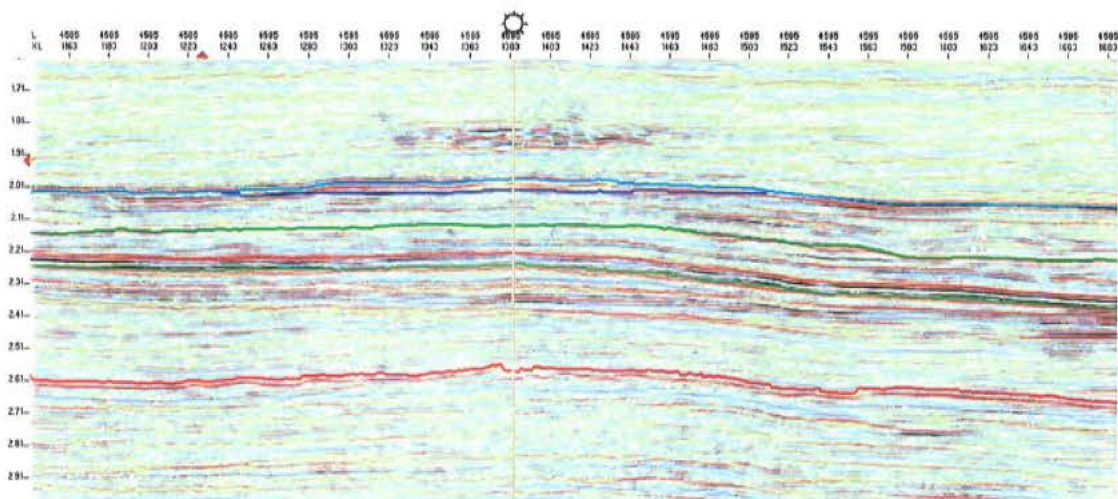


**Figure 3: West-East line through the H-1x well. Top Chalk is light blue, dark blue is the mapped GOC, green is Base Chalk, and red is Top Jurassic. Note the gas cloud above the chalk.**



## 2.2 Base Chalk

The Base Chalk is chosen at a relatively strong trough corresponding to a downward decrease in acoustic impedance, which makes it easily traceable. Reflection patterns are generally parallel to sub-parallel above and below the Base Chalk reflector. The closure defining the Roar Field is only weakly visible.

## 2.3 Intra Chalk reflector

The Intra Chalk reflector is a relatively weak reflector corresponding to a downward decrease in acoustic impedance; a trough. The reflector shows parallel to truncational relations to underlying reflections, which are parallel to sub-parallel. Reflections above show parallel to baselapping relations to the reflector. The tie in Roar-2 appear to approximately correspond to the top of Chalk Unit-2 equivalent to mid Hod Formation or near top Santonian (Lieberkind et al. 1982).

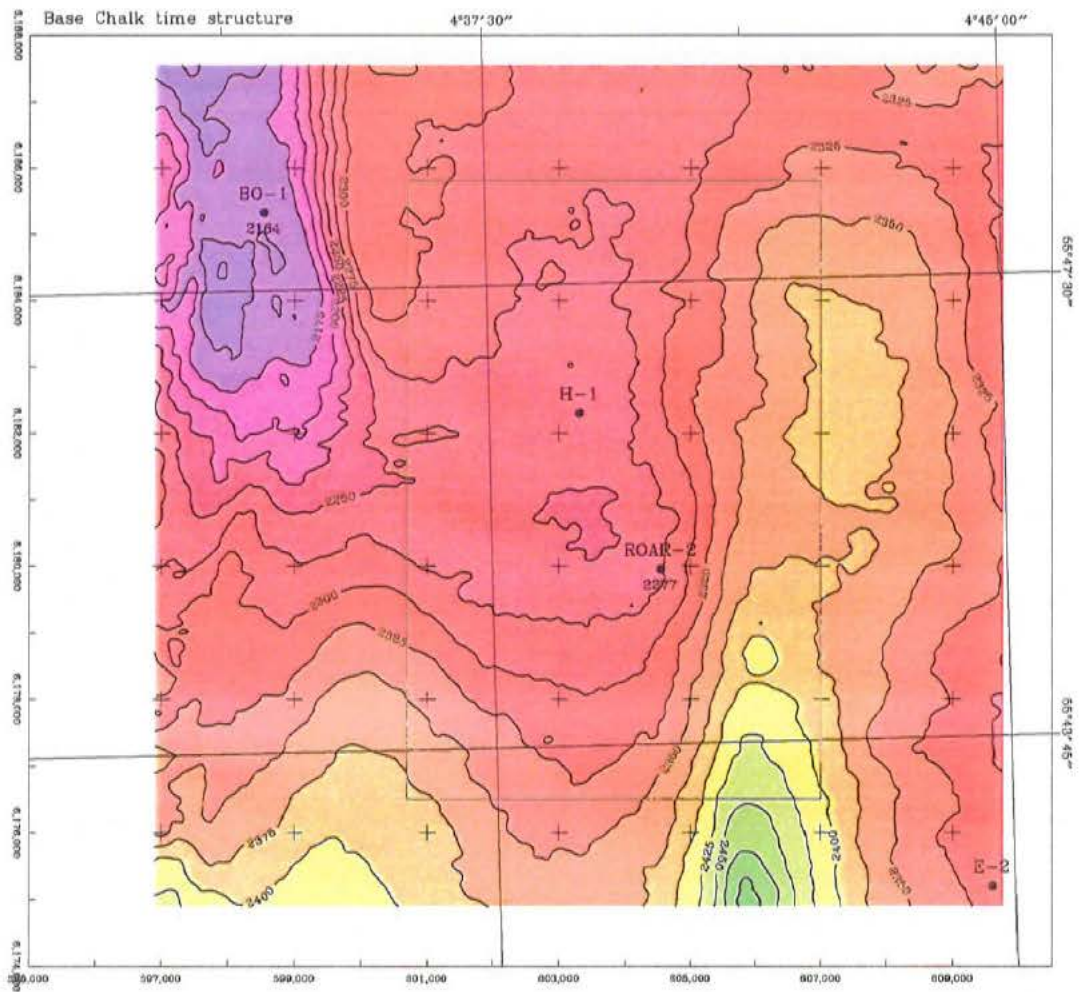


Figure 4: Base Chalk time structure map. Box shows location of simulation volume. C. I. is 25 msec.

## 2.4 Top Chalk Reflector

The Top Chalk Reflector is chosen as a positive reflector (peak) corresponding to a downward increase in acoustic impedance. However, in the south-eastern corner of the study area, corresponding to the north-western edge of the Tyra Field, a clear phase change takes place such that the Top Chalk corresponds to a trough (Fig. 9). This is also the case along the edges of the Roar field as defined by the direct hydrocarbon indicator (DHI) reflections (see below). However, the reflector is curiously again becoming positive in the crest area of the Roar Field where the gas is located. This may suggest that the amplitude variations in the Roar Field may not only be a direct consequence of changes in fluid content in the chalk. The Top Chalk reflector is generally showing conformable relations to internal reflection above and below. However, along the North Jens structure and to the North-east truncation relations are found below the reflector indicating erosion of the Top Chalk surface. This erosion is apparently only cutting down into the Danian, but is not affecting the Maastrichtian.

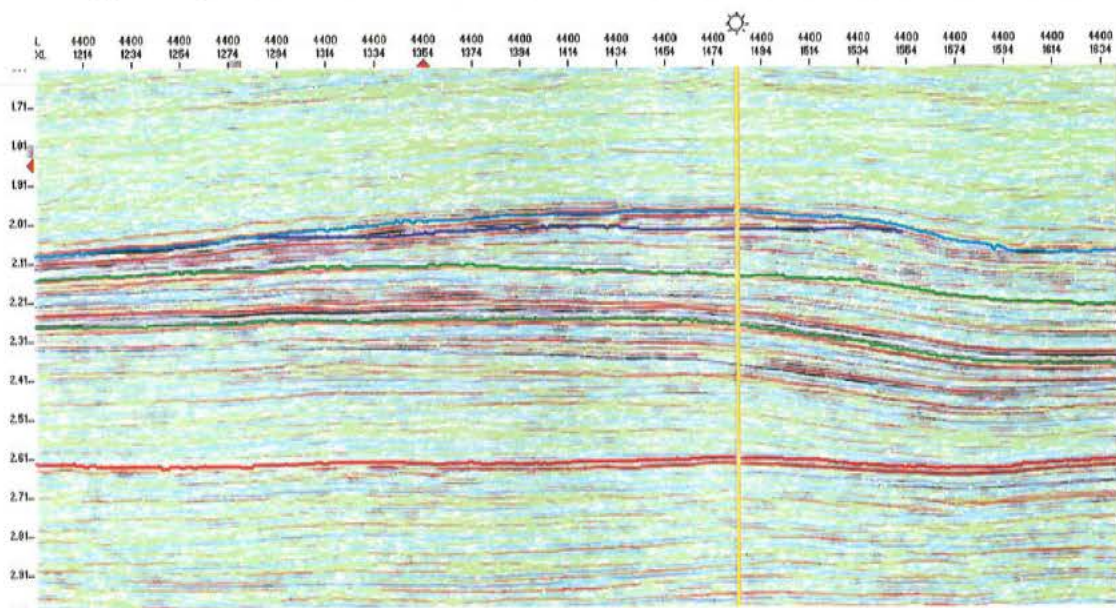


Figure 5: West-East line through the Roar-2 well.

## 2.5 Direct hydrocarbon indications

A small area in the succession above the Top Chalk reflector in the vicinity of the H-1x well show anomalously high amplitudes (Fig. 3). The log from H-1x (see enclosures 1 and 2) suggests that the anomaly is due to gas. This occurrence is not the target of this study. However, the anomaly is likely to be producing problems for the AVO analysis (Wagner 1999) and for depth conversion.

In the central Roar Field relatively strong positive sub-horizontal reflections and abrupt amplitude changes in dipping reflections line up along a near horizontal plane to suggest that they constitute a direct indication of the presence of hydrocarbons. This surface is mapped and seems to display a slight southward dip as consistent with suggested pressure gradient in the water phase resulting from southward porewater flow (e.g. Thomassen and Jacobsen



1994). As the chalk is strongly affected by capillary forces, it may also be an expression of higher porosities to the south resulting in deeper occurrences of relatively high hydrocarbon saturation.

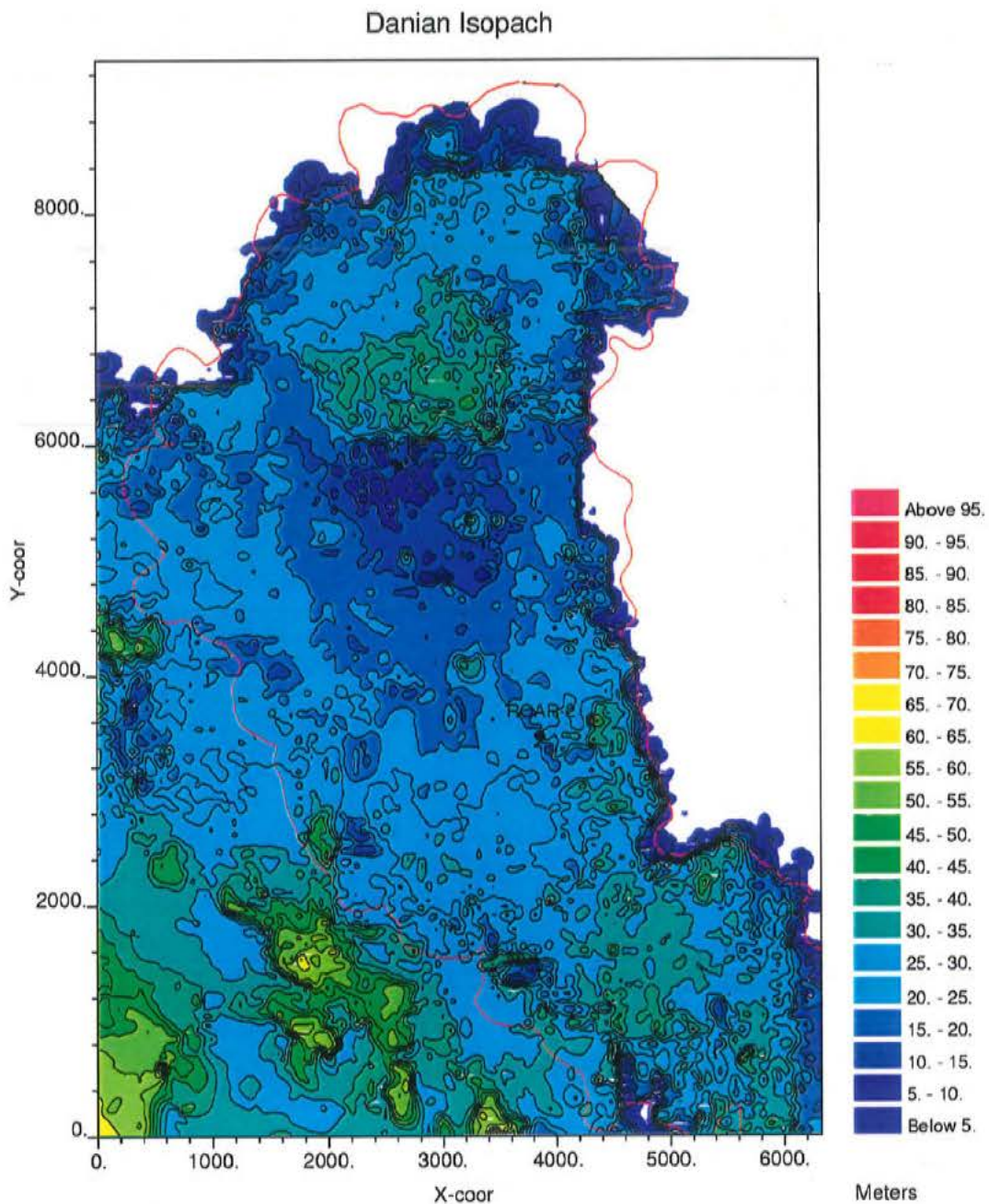


**Figure 6: Danian isopach map within simulation box. Red line shows the interface between Top Chalk and the DHI reflector. Note large area to the North and East where the Danian is below seismic resolution and assumed absent.**



## 2.6 Top Maastrichtian

The Top Maastrichtian is only interpreted in the central part, where the Roar Field accumulation is found. The reflector is a weak positive reflection (peak) more or less corresponding to the peg-leg below the Top Chalk reflector. For this reason, and because the Danian interval is just about the thickness that can be resolved in the seismic data, it is traced with some uncertainty. In addition errors may occur because of interference with the assumed direct hydrocarbon indicator.

The Top Maastrichtian reflector is interpreted because it together with the Top Chalk reflector defines the Danian equivalent to Chalk Unit 6 or the Ekofisk Formation (Lieberkind et al. 1982 and Nygaard et al 1983). The subdivision of the reservoir into a Danian and a Maastrichtian unit is required because different capillary pressure models apply to the Danian and the Maastrichtian (Engstrøm 1995), and because different porosity permeability relationships exist (e.g. Frykman 1996). The reflector is seen to become truncated towards the northern and eastern flank of the Roar Field as consistent with very thin Chalk Unit 6 in the Bo-1 and Boje-1 wells (2 and 4 m respectively).

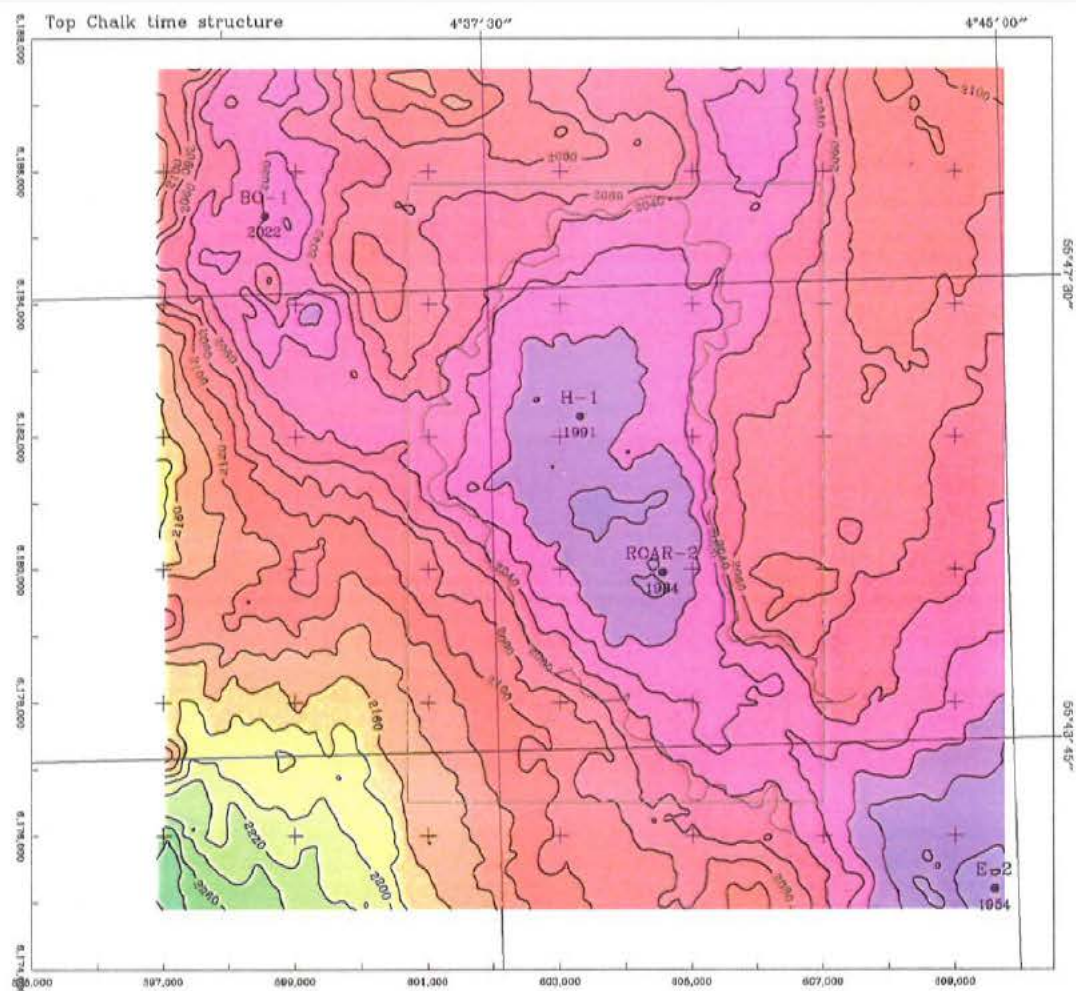


**Figure 7: Top Chalk time structure map. Intersection between this surface and the mapped DHI is shown as a grey line. This may indicate the extent of the HC accumulation. The box shows the locations of the area chosen for geostatistical modelling.**

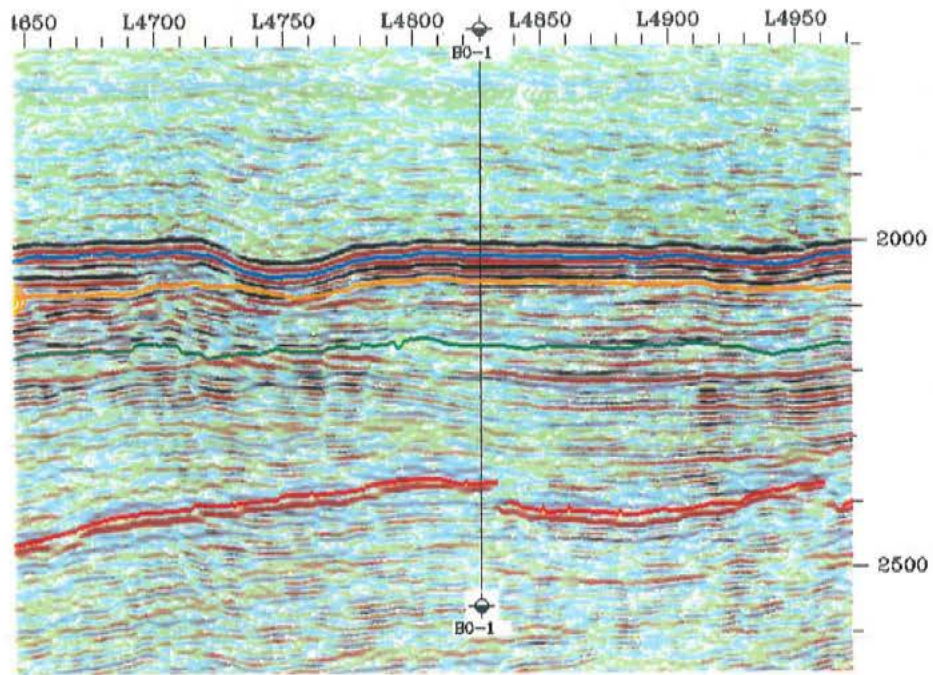


**Figure 8: South(left)-North cross line through the Bo-1 well. Note the unconformity at Base Chalk, where also prominent Top Jurassic faults terminate.**

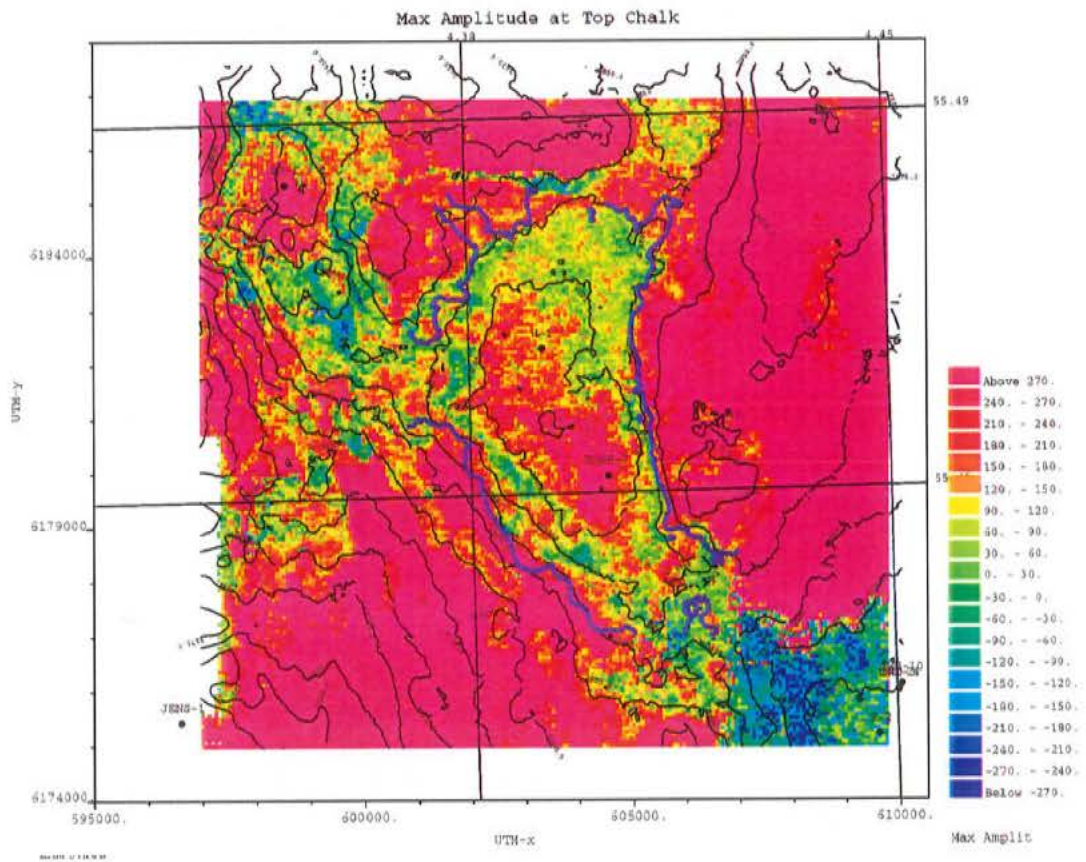


**Figure 9: Amplitudes at Top Chalk level. High amplitudes corresponds to yellow to red colours. Note similarity to Fig. 11.**



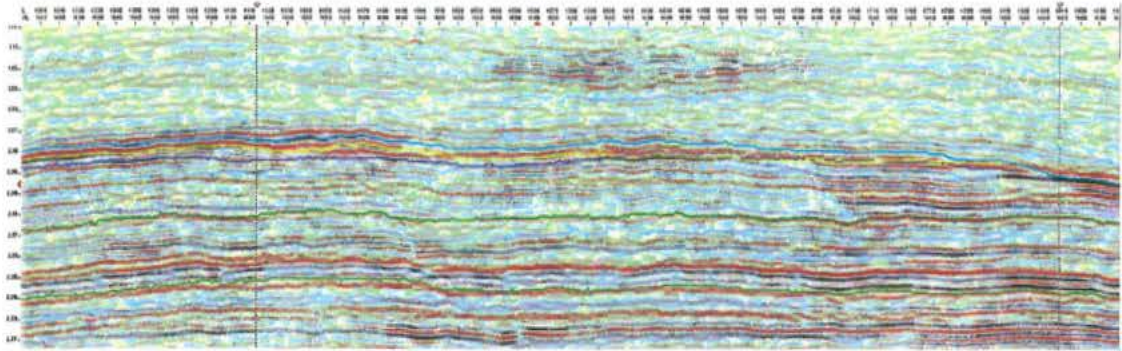


**Figure 10: South(left)-North cross line (trace 1440) across the central part of the field. Note faults at Base Chalk only produces flexure at Top Chalk level. Also note the gas cloud in the Post Chalk succession.**

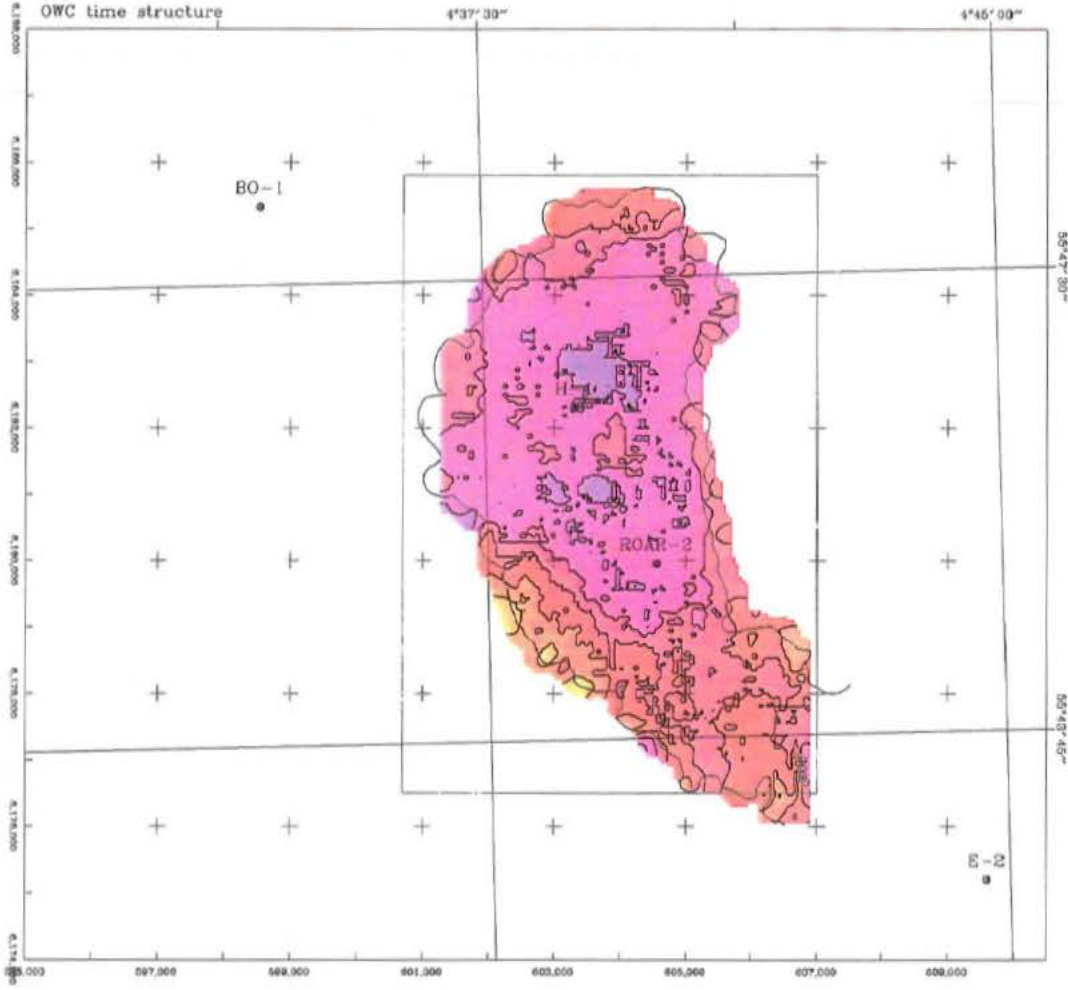


**Figure 11: Time structure map of the phase and/or amplitude change possibly corresponding to a direct hydrocarbon indication (DHI). Mapping extends to the intersection with the Top Chalk surface. Note depression to the Southwest.**

## 2.7 Cenozoic reflectors

In order to investigate post depositional tectonic movements, two Cenozoic reflectors have been interpreted. These are the Near Top Middle Miocene reflector (NTMM) and the Post TMM reflector (PTMM). The Near Top Middle Miocene reflector is located within approximately 40 msec of the Top Cen-4 Unit (Kristoffersen and Bang 1982; Nielsen and Japsen 1991; Table 4), and is corresponding to the top of the overpressured section of the Cenozoic succession (Jacobsen et al. 1982). This is also suggested from the discontinuous reflection patterns below the reflector (Fig. 16). The Post TMM reflector is located within the Cen-5 Unit.

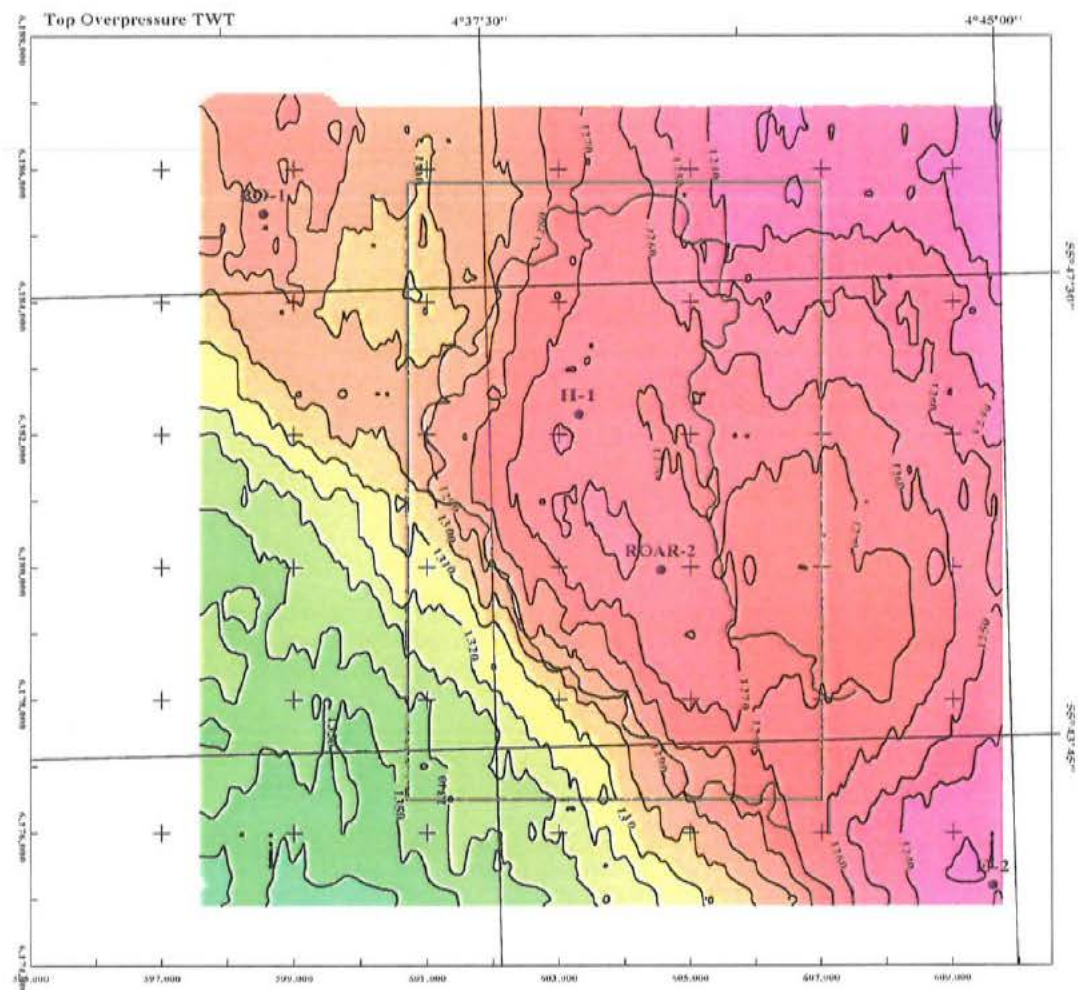


**Figure 12: Near Top Middle Miocene time structure map. The box shows the location of the simulation volume. The DHI edge is also shown to indicate the Roar Field location (C. I. =10 msec).**

The two reflectors have not been chosen in order to outline specific rock unit boundaries or biostratigraphic marks, but merely for the purpose of flattening the Top Chalk structure at these reflectors so that palaeo-structure configurations can be studied. This is done according to the assumption that the reflectors represent surfaces that were horizontal during the



time of deposition. There is, however reason to believe that the Post TMM reflector might have been inclined at the time of deposition (differential palaeo bathymetry may have existed). This is seen from the fact that this reflector is more inclined than some overlying and underlying reflectors. It may, however, also have been sub-horizontal, which leads to important conclusions as detailed below and in later chapters..

**Table 4: Depths to Cenozoic reflectors in msec. Last column is from Nielsen and Japsen (1991).**

Well	PTMM	NTMM	Top Cen-4 Unit
H-1	1117	1262	1301
ROAR-2	1106	1263	1291
BO-1	1129	1284	1321
E-2	1100	1231	1250

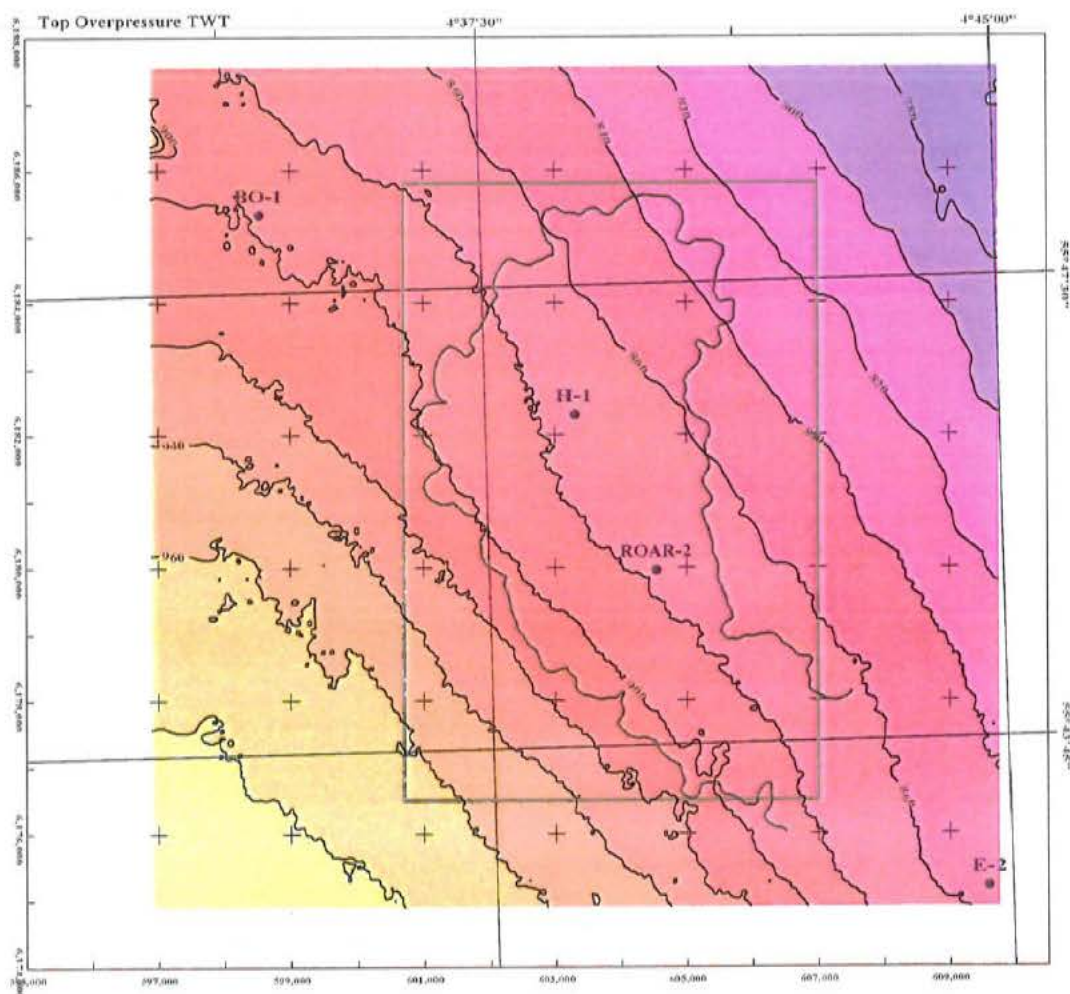


**Figure 13: Post Top Middle Miocene reflector. The box shows the location of the simulation volume. The DHI edge is also shown to indicate the Roar Field location (C. I. = 20 msec).**

The structure map of the Near Top Middle Miocene reflector suggest that the tectonic movements responsible for the formation of the Roar Field had not ceased yet, because the outline of the field is visible in the contour pattern. It is, however, evident that differential movements had ceased at the time corresponding to the Post TMM reflector, since only a gently sloping surface is seen. When the Top Chalk is flattened at the Near Top Middle Miocene reflector, it is clear, that some growth of the structure occurred prior to Middle Miocene times. The structure was more broad and flat than today. It is also interesting to see the much stronger slope to the Northeast away from the Roar Field structure as compared to the present configuration (Fig. 7).

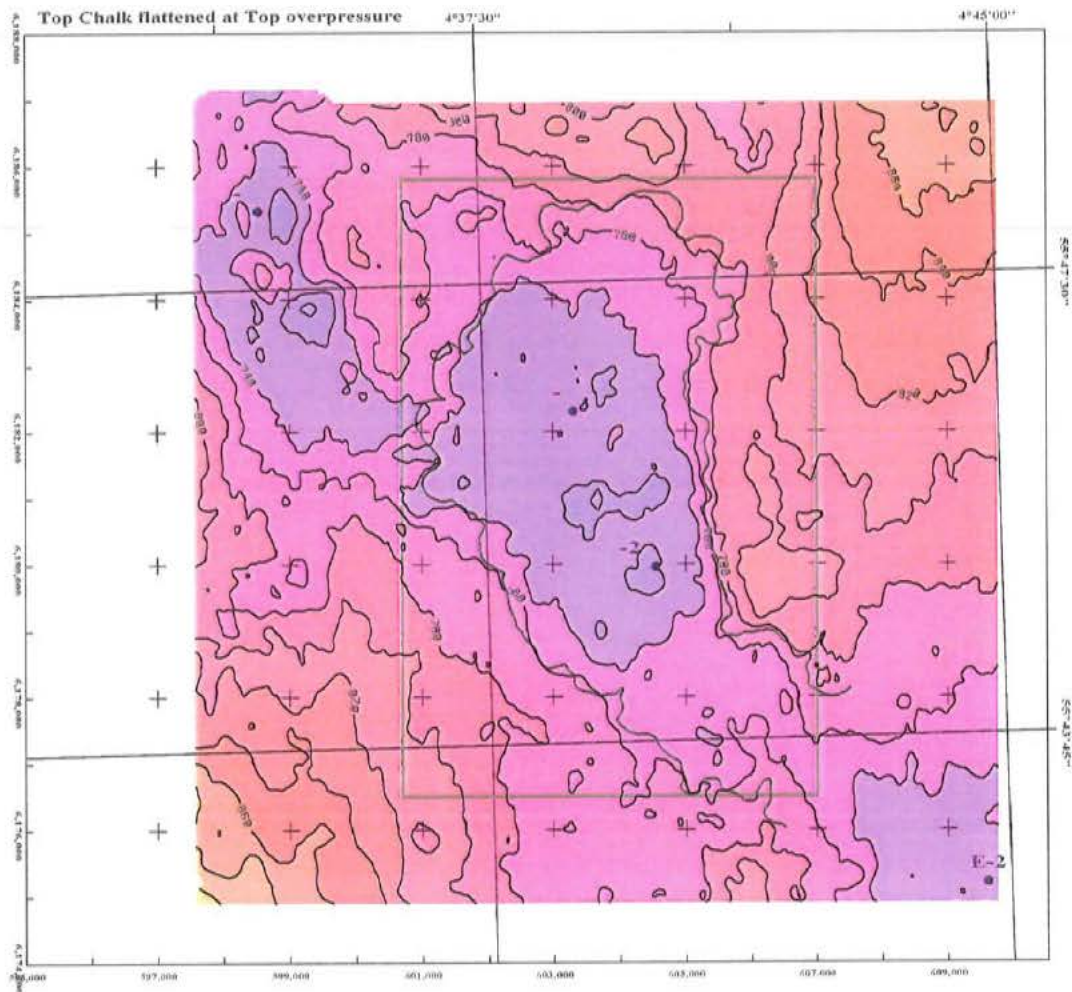


**Figure 14: Time structure map of the Top Chalk flattened at the Near Top Middle Miocene reflector (C. I. = 20 msec).**

It is therefore possible that this strong slope may have caused slope instability of the youngest chalk deposits, and thus explain the thin or absent Danian succession to the North and East (Fig. 6).



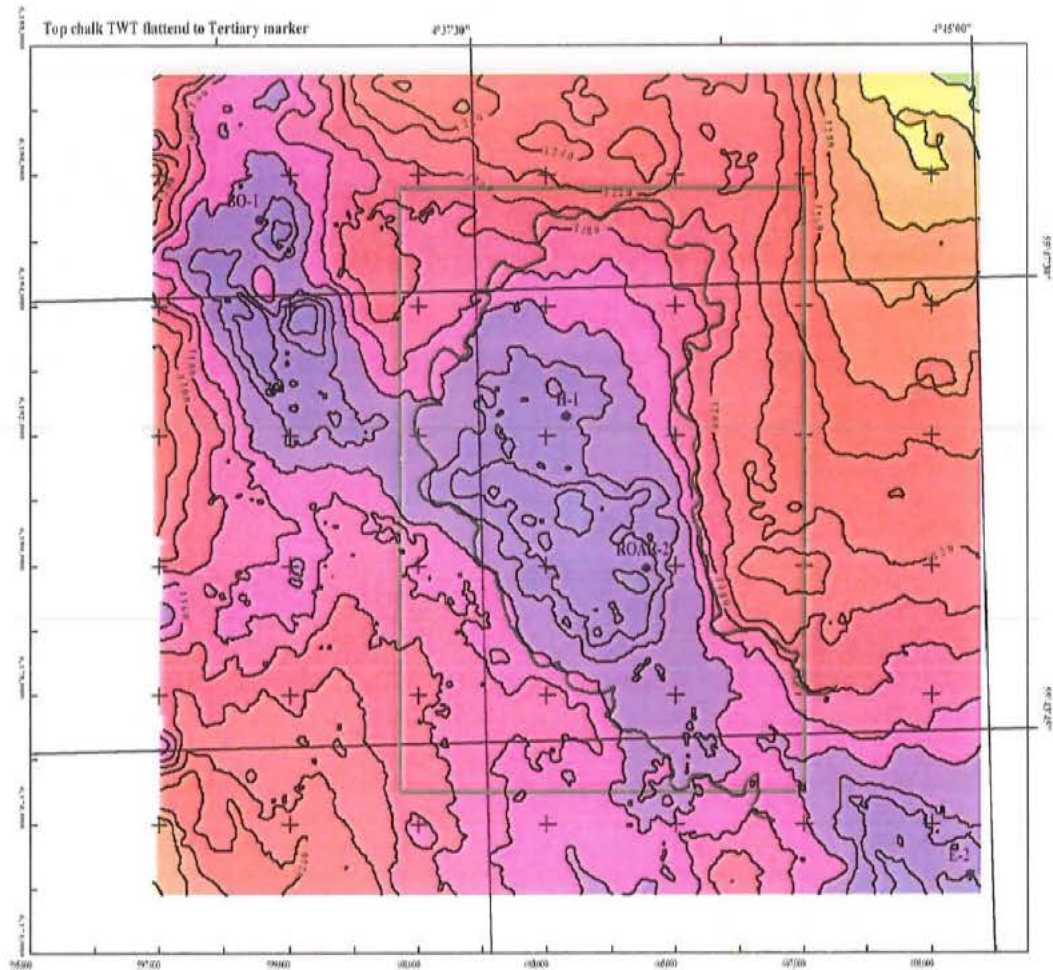


**Figure 15: Time structure map of the Top Chalk flattend at the Post Middle Miocene reflector (C. I.= 20 msec, but also including the 1110 msec contour).**

The Top Chalk time structure map flattend at the Post Middle Miocene reflector (Fig. 15) still displays a strong slope to the North East, but is generally illustrating the morphology seen today. An important difference, however, is that the crestal area is shifted to the Southwest. The anticline inflection axis is Southwest of the two wells, that are located on the crest of the present anticline as it appears on the time structure map (Fig. 7). In addition another structure is suggested due South of the Roar Field structure and west of the Tyra Field at the edge of the mapped area. As mentioned above, the reconstruction by flattening at the Post Middle Miocene reflector may be erroneous, because this reflector may never have been horizontal. The southwesterly shift of the crestal area would still occur with less tilt as suggested by the broad flat structure that results from flattening at Near Top Middle Miocene (Fig. 14).

This tilting effect may help explain the shape of the DHI reflector, if it is not representing a fluid boundary as of today (as discussed in chapter 6), but rather a palaeo fluid boundary. The DHI map shows a conspicuous depression at the southwestern edge. This depression might represent a previous flat lying fluid contact. This contact would then today represent a diagenetic boundary that therefore shows up on the seismic data, even though the fluids might have gone.



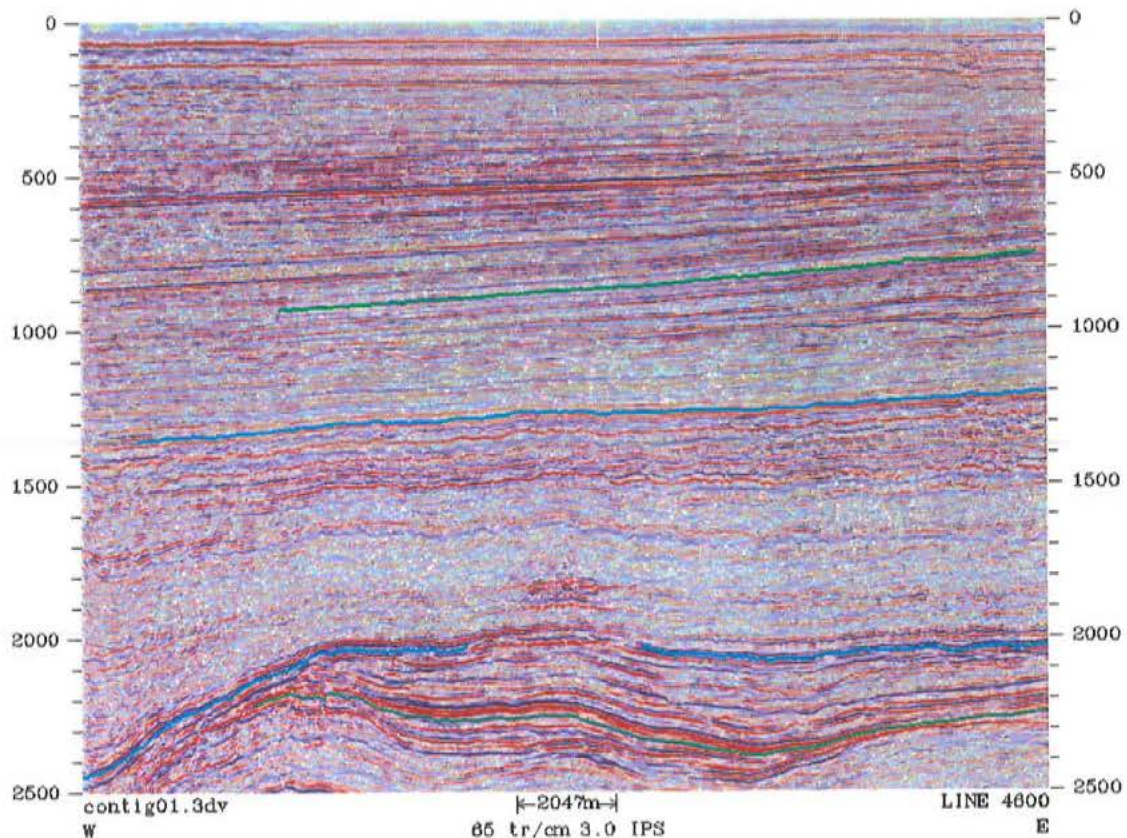


**Figure 16: Line 4600. Top Chalk is shown in light blue at about 2000 msec and is omitted at the Roar Field location to show phase and DHI effects. Near Top Middle Miocene is located at about 1300 msec (light blue). Post TMM reflector is located at 700-900 msec (light green). Note gas cloud centrally at around 1800 msec.**

## 2.8 Summary on interpretation of seismic data

The interpretation study shows that the Roar is a very gentle anticline, apparently with no significant faulting. The formation of the structure is probably due to inversion tectonism. Growth of the structure probably started penecontemporaneously with deposition of the chalk and continued until Middle to Late Miocene times. The early phases of inversion may have localized erosion of the Danian by causing slope instability (see also later chapters). A conspicuous southerly dip on the probable direct hydrocarbon indication (DHI) reflector either suggest strong southerly waterphase flow or, - more likely, -a small rotation to the Northeast after the first invasion of hydrocarbons. This means that the DHI reflector is a palaeo fluid contact. The alternative interpretation of the DHI reflector that it is representing the present fluid contact is unlikely, because it means the structure is filled to structural closure (and beyond), which is virtually impossible due to the strong capillary forces in the chalk (see later chapters). A conspicuous gas cloud is located above the northern portion of the field, - apparently and curiously not over the summit of the field structure (in time domain).



## 2.9 Depth conversion

The purpose of the depth conversion is not only to produce reliable depth structure maps, but also to produce reliable interval velocities in the reservoir zone for depth conversion of the inversion derived seismic impedances that comes with samples for every 4 msec roughly corresponding to every 6<sup>th</sup> meter (Wagner 1999).

Depth to the Top Chalk is calculated from average velocities given by a previously made regional mapping study (Britze et al., 1995a). The average velocity is calculated using a function of the type:

$$V_i = V_0 + dv + k \cdot Z$$

where  $V_i$  is the interval velocity,  $V_0$  and  $dv$  are surface velocity and associated anomaly (laterally varying),  $k$  is the velocity gradient, and  $Z$  is depth. The deviations from the average velocity function, the anomaly ( $dv$ ) is typically obtained from well data. The method is therefore capable of handling anomalies with a size larger than the well spacing.

The depth conversion for the Top Chalk applies a three layer model: The water column, the interval down to the base of the Nordland Group (Base Cen-5 unit) and an interval for the remaining overpressured interval (see Britze et al. 1995a for details).

Calculation of the depth to the top Maastrichtian and the velocities necessary to depth convert seismic impedances, cannot be based on simple use of interval velocities from the regional velocity studies of the Chalk Group (Britze et. 1995b) because they refer to the entire package and therefore would be too high for the reservoir interval. For the chalk,  $V_0$  is 2162 m/s (and  $k$  is 0.72 s<sup>-1</sup>), but the  $dv$  is derived from regional interpolation of velocity anomalies as they appear in the well data and  $V_i$  is influenced both by velocity anomalies and depth increase. The interval velocities from the earlier study is therefore back-calculated to surface velocities ( $V_0 + dv$ ) using:

$$V_0 + dv = \frac{V_i - kz_t}{(1 + k\Delta T / 4)}$$

where  $\Delta T$  is the time thickness. This expression is approximate. Using this equation, new interval velocities are calculated to find the Top Maastrichtian, and to use for depth conversion of the impedances derived by seismic inversion. Representative interval velocities for the reservoir interval below the Danian is based on calculations in the upper 60 msec of the Maastrichtian (90 m assuming a velocity of 3000 m/s). The new interval velocity map is thus calculated from:

$$V_i = \frac{2}{k\Delta T} (V_0 + dv + kz_t)(e^{k\Delta T / 2} - 1)$$

where  $z_t$  is the depth to the top of the interval,  $\Delta T$  is thickness of the Danian or equal to 60 msec for the Maastrichtian (upper portion roughly equivalent to the reservoir zone), and  $V_0 + dv$  is derived from the above back-calculation to surface velocities.

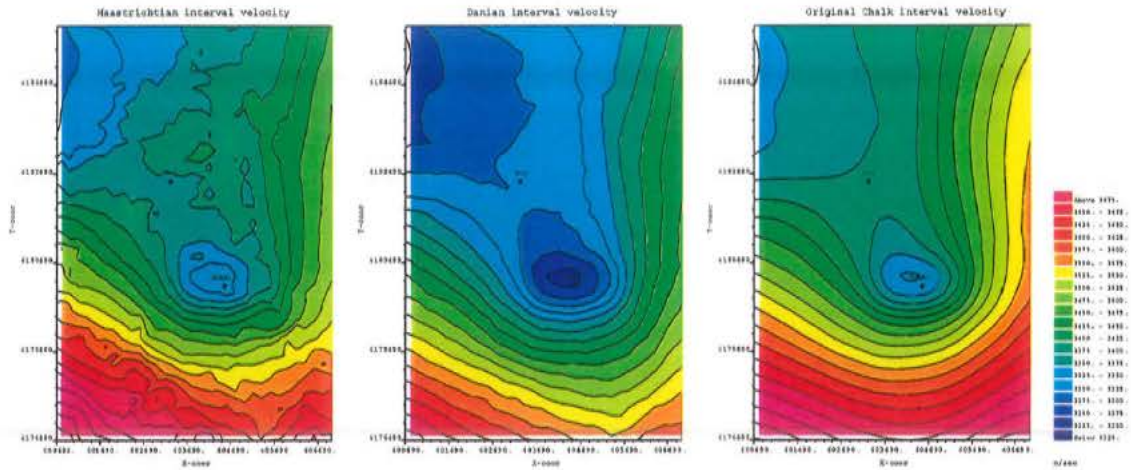


**Figure 17: Interval velocity in the chalk, the Danian and the upper 60 msec of the Maastrichtian within the simulation box.**

The resulting velocity fields for Danian and the upper Maastrichtian as compared to the entire Chalk Group average velocities are shown in Fig. 17. A result of the depth conversion is shown in Fig. 18, and depth structure maps of the Top Danian and Top Maastrichtian are also shown as enclosures 5 and 6.

It should be emphasized that velocity variations using this method are mere model based predictions, - not observations. Deviation from the model (velocities vary with depth and layer thicknesses and smooth regional changes) may occur, which are caused by phenomenon not monitored by well data. These phenomenon could be gas clouds and channel; features (other than structure) of little areal extent.

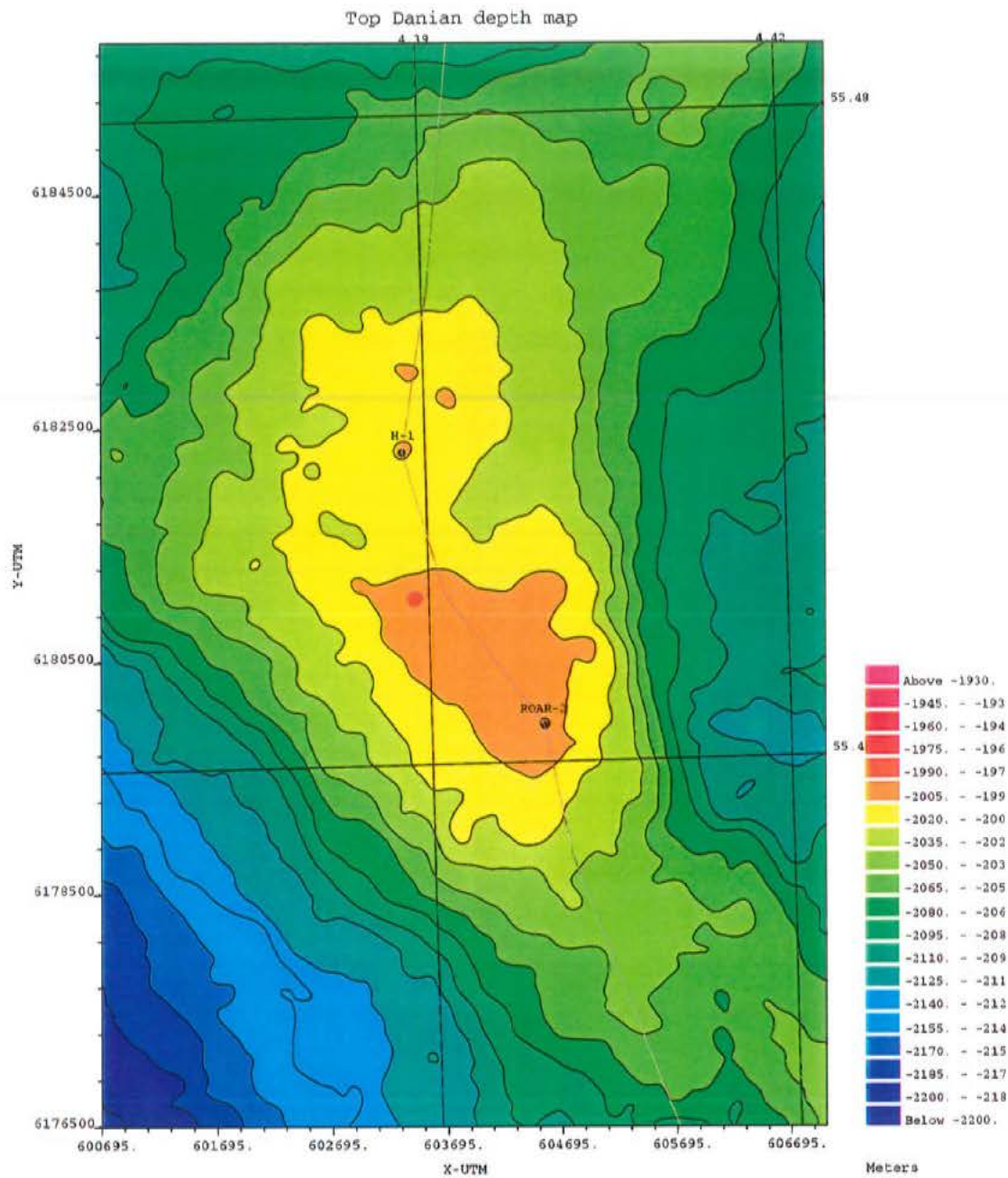
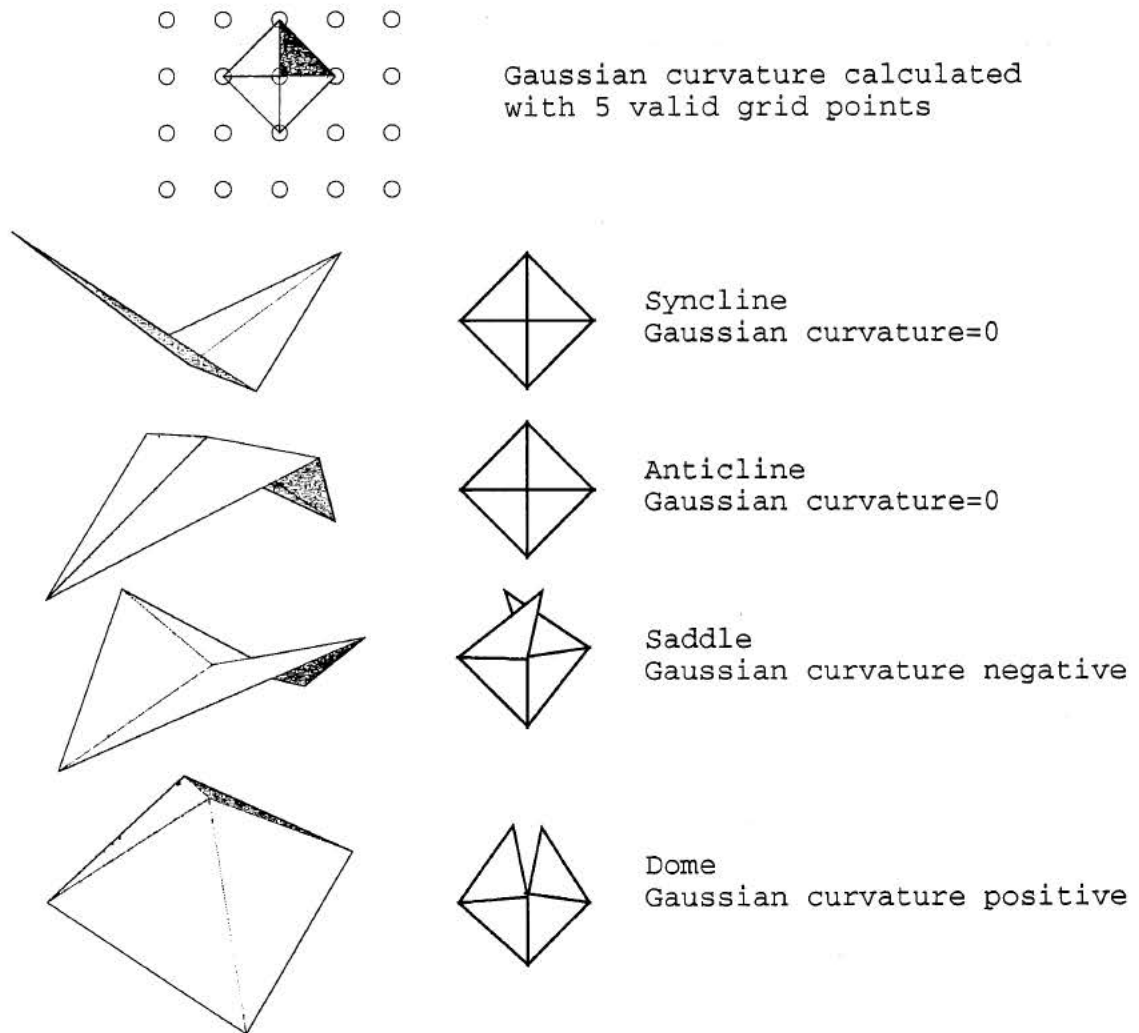


Figure 18: Depth structure map of the Top Chalk (see also appendix). Compare Fig. 7. Contour interval is 15 m. The map frame corresponds to the simulation volume. Location of a cross section showing simulation results is shown as a thin grey line

### 3. Fracture mapping

Fractures are not considered to be of major importance in the Roar Field (Andersen and Doyle 1990). It is, however, still considered important to assess the areal distribution of fractures away from wells in order to forecast reservoir performance. Major fractures may be given directly from the seismic data during mapping, some may be negligible in the seismic data and thus typically omitted, and some may be below seismic resolution. While only the first of these three groups may be identified during seismic mapping, all three groups of fractures may be important for the reservoir performance. For the purpose of assessing the areal distribution of the two latter groups of fractures, the gaussian curvature is calculated for each structure map as described by Lisle (1994). Gaussian curvature may indicate zone of abnormal strain, that accordingly are likely to be fractured even though these fractures might be below seismic resolution.



**Figure 19: Principle for calculating gaussian curvature from regular gridded surfaces. The curvature is given as the difference between 360° and the sum of the 3D angles from a centre point to the adjacent grid points**



Strain within the surfaces of single axis flexural slip folds may be negligible, but any surface involving double curvature cannot form without stretching or contraction along bedding planes. The degree of double curvature is given by the gaussian curvature, which is defined as the product of the curvature along two principal directions; if one direction is zero the gaussian curvature is zero. The method assumes negligible amounts of ductile deformation relative to elastic/plastic deformation, and is best applied to media with planar anisotropic material properties (well bedded sediments).

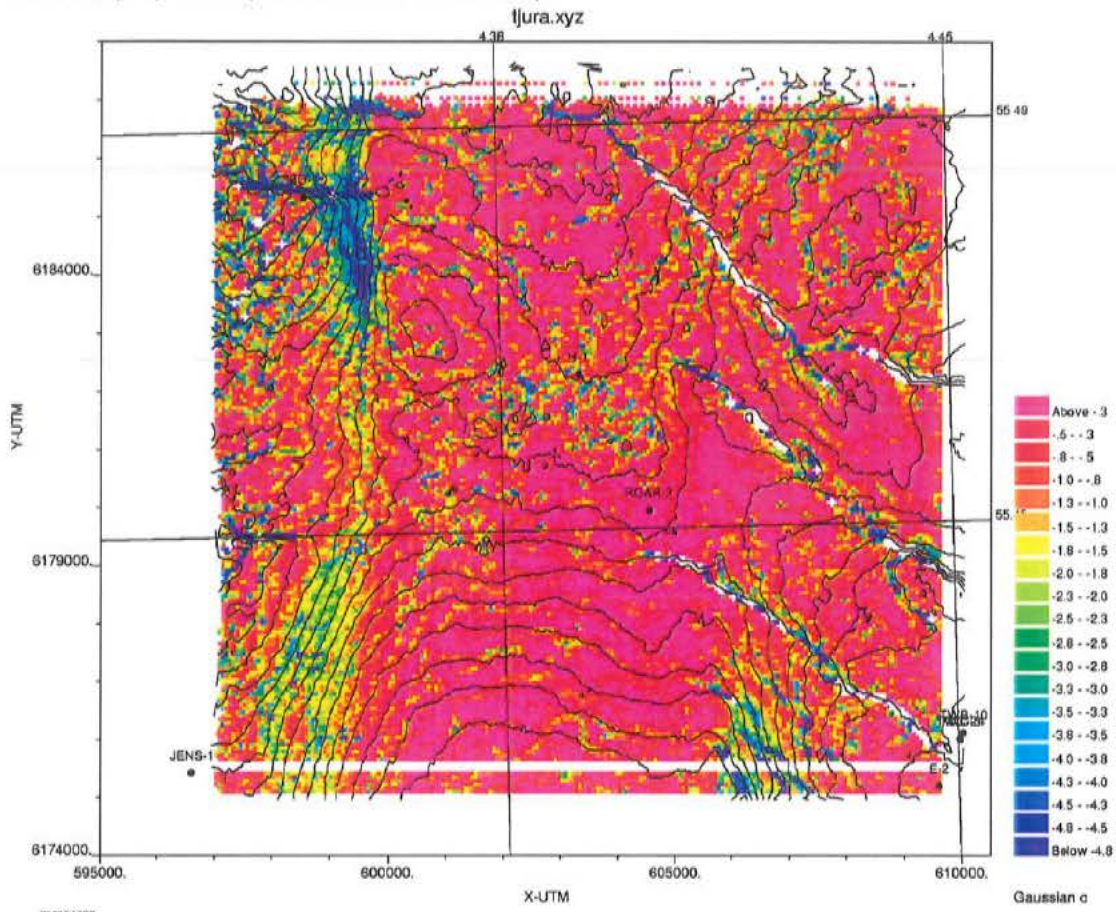


**Figure 20: Gaussian curvature at Top Jurassic. High strain areas are shown in yellow, green and blue, and low strain areas are shown in red. Comparison with Fig. 2 shows that major faults are clearly depicted in blue. Additional minor faults and fractures zones are detected by the degree of gaussian curvature.**

Even though no quantitative connection between the magnitude of gaussian curvature and the degree of strain may be erected, the magnitude may be a qualitative expression of the degree of strain. Gaussian curvature mapping provides an indirect measure of fracturing from seismically observable features: the local shape of the surface. It is thus useful in localising subseismic fracturing.

The gaussian curvature may be calculated on the basis of regular grids as shown in Fig. 19. In this study, these grids are generated in the ZMAP Plus mapping software, where the grid increment is selected to be approximately equal to the spacing of the interpreted lines and cross lines. It is calculated for all mapped surfaces; also for the lower non-reservoir levels to allow comparison of strain levels. As seen in Fig. 20, the main faults at Top Jurassic level are clearly automatically detected as blue high strain areas. In the Northwest part of the

map, which is coincident with the South part of the Valdemar Field, minor NE-SW striking faults are recognisable which not mapped here, but identified in other studies (e.g. Britze et al. 1995b).

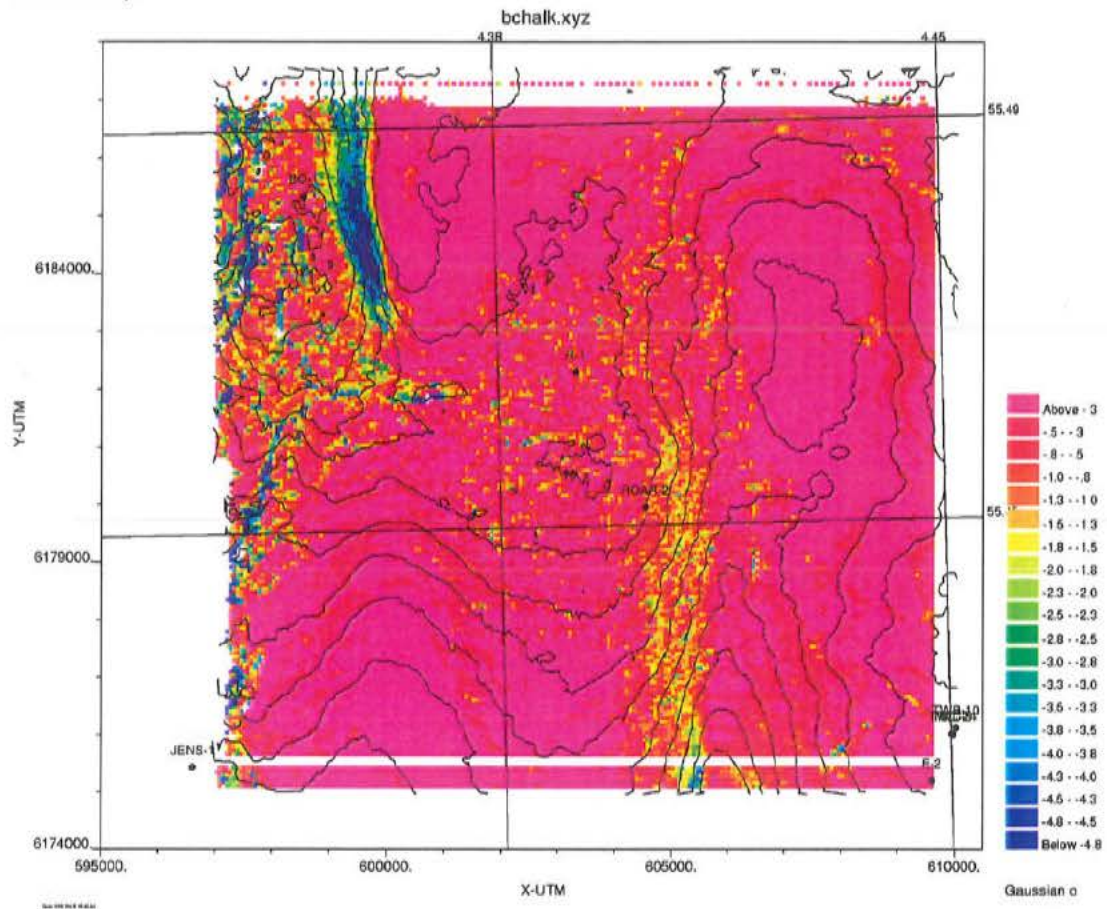


**Figure 21: Gaussian curvature at Base Chalk level. High strain areas are shown in yellow, green and blue, and low strain areas are shown in red. Contours represent 25 msec TWT contours of the Base Chalk level.**

The calculated gaussian curvature at Base Chalk level (Fig. 21) displays two major North South striking areas of abnormal strain with an intermediate area of minor strain coinciding with a culmination of the structure. The left-stepping configuration of the strained areas combined with the intermediate culmination strongly suggest minor right lateral movements along North South striking zones of weakness. These movements occurred during the Late Cretaceous and/or later, and may contribute to explaining the location of the Roar structure. An overall decrease in strain at the Base Chalk level as compared to the Top Jurassic level is indicated by decrease in blue and green colours. Major NW-SE striking faults at top Jurassic level as well as WNW-ESE major faults are not affecting the base Cretaceous as may also be observed in cross sections (Figs. 2, 4, 8).



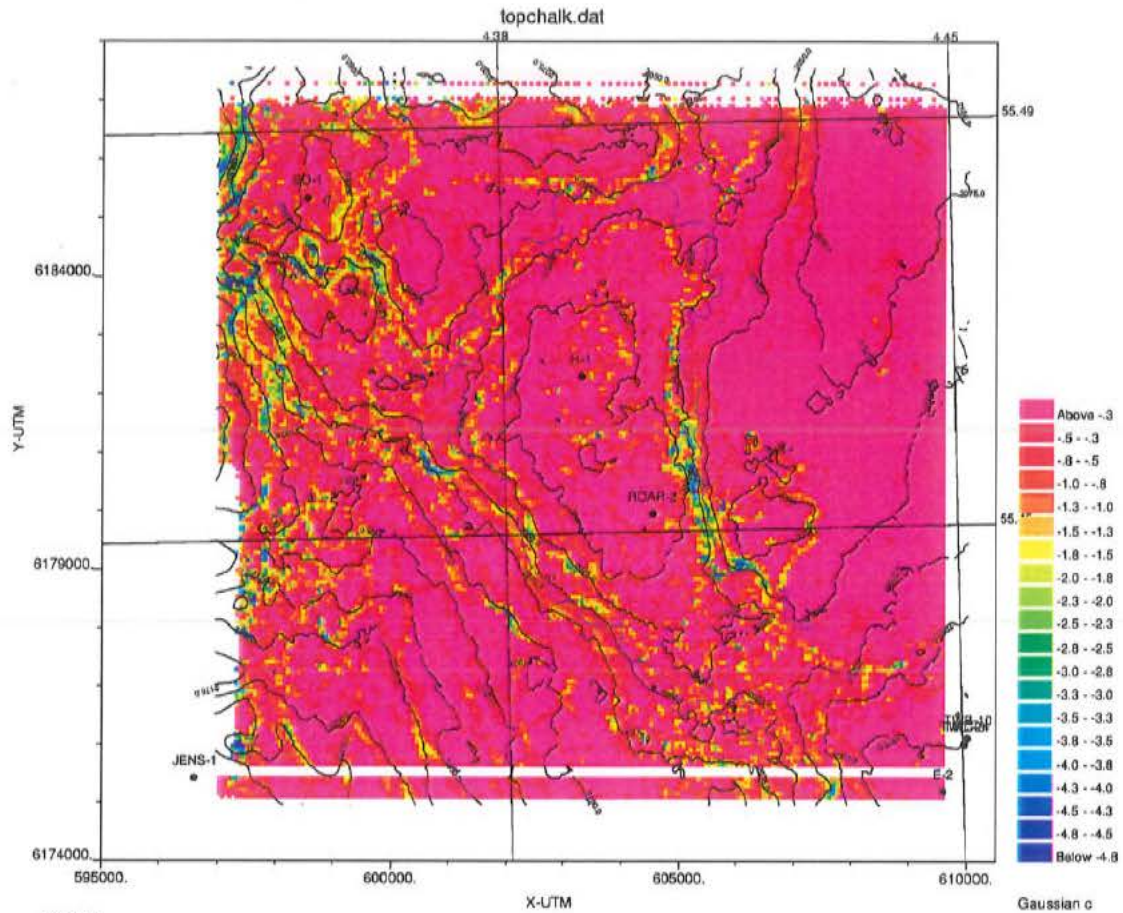


**Figure 22: Gaussian Curvature at Top Chalk level. TWT contours with 25 msec. intervals are also shown. The mapped limit of the HC accumulation (compare Fig. 9) is shown as a grey line.**

### 3.1 Summary on fracture mapping

The gaussian curvature may be used to locate zones of anomalous strain in the form of fracturing. An example of qualitative interpretation of location of fracture zones based on gaussian curvature is shown in Fig. 23. None of these fracture zones are large enough to be detectable during standard seismic interpretation. As may be evident, no major fracture zones are found inside the reservoir as indicated by the line showing the approximate intersection of the DHI reflections and the Top Chalk.

The relatively strong anomalies occurring along the eastern edge of the field (indicated by HC limit line) and to some extent at the northwestern edge coincide with the erosional limit of the Danian (Fig. 6). The gaussian curvature are therefore likely to represent a quassa-like erosion edge rather than fracturing in that case.

Since the gaussian curvature is at a negligible level inside the area of the accumulation, it is concluded that fracturing is insignificant for the reservoir performance.

Qualitative fracture zone interpretation

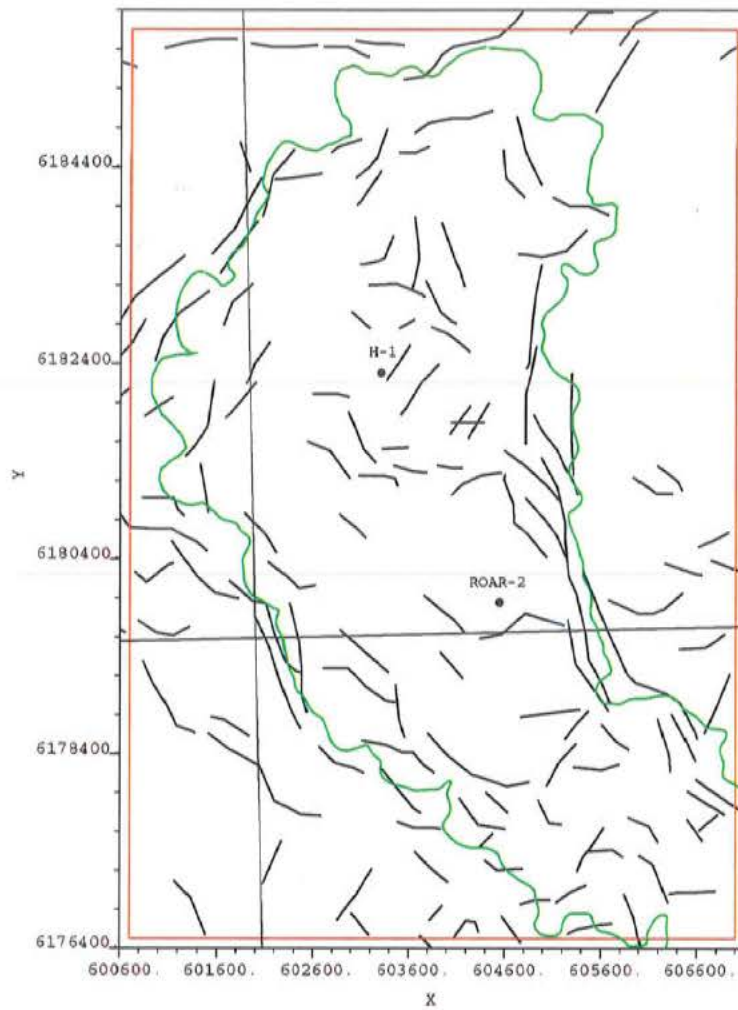


Figure 23: Qualitative interpretation of fractured zones at Top Chalk level inside the simulation volume.

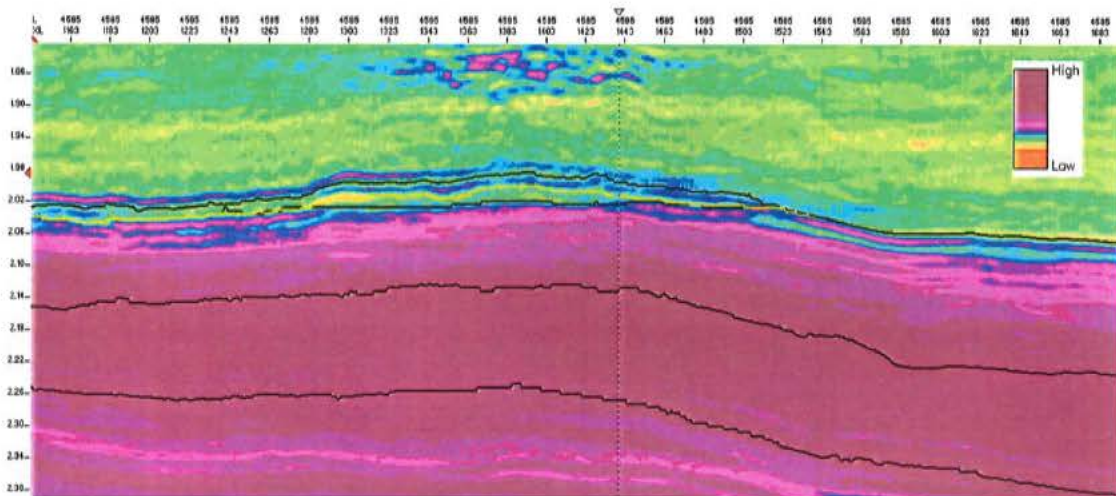
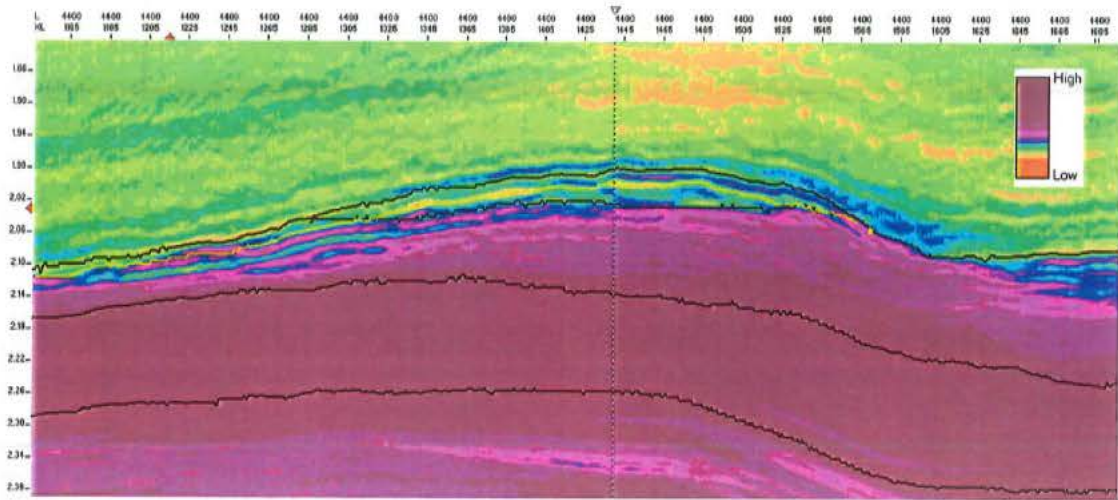


Figure 24: West East oriented Impedance cross section corresponding to Fig. 3 (line 4585). Note gas cloud anomaly centrally at about 1.86 sec.





**Figure 25: West East oriented impedance cross section corresponding to Fig. 5 (line 4400).**

## 4. Fluid substitution

The fact that the reservoir is clearly visible on a Top Chalk reflection amplitude map (Fig. 9) suggests that impedances within the chalk are reduced within the reservoir chalk as compared to the adjacent chalk or alternatively impedances are changing in the cap rock. On impedance profiles it is clear, however, that impedances are exceptionally low within the reservoir zone (Figs 24, 25 and 26). Horizons Top Chalk, Top Maastrichtian, the direct hydrocarbon indicator (the DHI), an Intra chalk reflector and Base Chalk are displayed in black on these profiles. The DHI seems to delineate a portion of the reservoir with abnormally low impedances suggesting high porosities. This may be an indication that seismic impedances are affected not only by variations in porosity, but are also lowered by variations in fluid content as indicated by the low amplitudes over the central part of the field. Alternatively the low impedances are indications of abnormally low porosities, - possibly preserved by early invasion of hydrocarbons, as is suggested by the exceptionally high porosities in excess of 50% (see enclosed logs). Possible influences of fluids on impedances may not be detrimental to the possible correlation between porosity and seismic impedance (as is used in the geostatistical reservoir characterisation), but it may cause differences in the relationship between the reservoir zone and the water zone.

As it is intended to produce realisations of porosity (and permeability) covering both the reservoir and the water zone, an attempt is made and described below to calculate the impedances for a totally water (brine) filled reservoir.

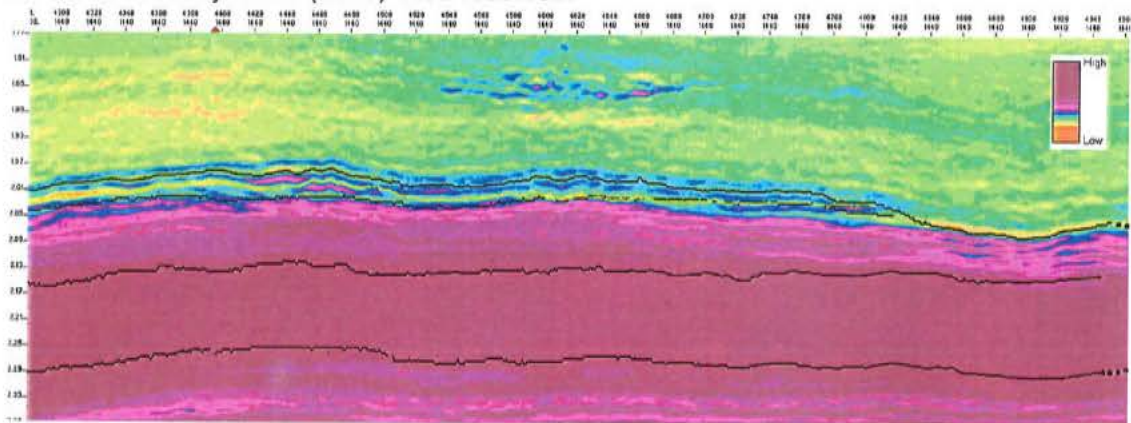


Figure 26: South-North impedance profile following cross line 1440 corresponding to Fig. 10.

### 4.1 General definitions

First basic definitions and symbols are outlined (see Mavko, Mukerji and Dvorkin, 1998 for further detail):

Bulk modulus ( $K$ ) is defined as the ratio of hydrostatic stress ( $\sigma_0$ ) to volumetric strain ( $\epsilon_{\alpha\alpha}$ ):

$$\sigma_0 = \frac{1}{3} \sigma_{\alpha\alpha} = K \epsilon_{\alpha\alpha}$$

and is related to seismic velocities according to:

$$K = \rho(V_p^2 - \frac{4}{3}V_s^2)$$

where  $\rho$  is density,  $V_p$  is pressure wave velocity and  $V_s$  is shear wave velocity. The second term disappears in the case of fluids because  $V_s \rightarrow 0$  for fluids.

Shear modulus ( $G$ ) is defined as the ratio of shear stress ( $\sigma_{ij}$ ) to shear strain ( $\epsilon_{ij}$ ):

$$\sigma_{ij} = 2G\epsilon_{ij}, i \neq j$$

which is related to seismic shear velocity according to:

$$G = \rho V_s^2$$

It is seen that  $G$  also becomes zero for fluids (or extremely non-coherent materials).

Rearranged  $V_p$  and  $V_s$  can be expressed in terms of  $K$  and  $G$ :

$$V_p = \sqrt{\frac{K + (4/3)G}{\rho}}$$

$$V_s = \sqrt{\frac{G}{\rho}}$$

The P-wave or compressional modulus, which is more directly related to the seismic data, is given by.

$$M = \rho V_p^2 = K + \frac{4}{3}G$$

which is defined as the axial stress to axial strain in a uniaxial stress state:

$$\sigma_{zz} = M\epsilon_{zz}; \epsilon_{xx} = \epsilon_{yy} = \epsilon_{yx} = \epsilon_{xz} = \epsilon_{yz} = 0$$

Note that all moduli have the same units (force/area;  $GPa$  typically). Seismic impedances ( $I$ ) obtained from seismic inversion is given by:

$$I = V_p \rho$$

and the density is dependent on the porosity ( $\phi$ ) given by:

$$\rho = \phi \rho_f + (1 - \phi) \rho_r$$

In this study the best *in-situ* estimates on the fluid densities ( $\rho_f$ ) are conveniently obtained from the RFT pressure gradients:

$$\rho_f = \frac{\Gamma \cdot C \cdot 1000}{0.3048 \cdot g}$$

where  $\Gamma$  is the pressure gradient in  $psi/ft$ ,  $C$  is the  $psi$  to  $kPa$  conversion factor (6.894757) and  $g$  is the gravity constant ( $9.82 \text{ m/sec}^2$ ). Rock densities ( $\rho_r$ ) are calculated from the mineral constituents.

With a knowledge of  $V_p$ ,  $V_s$ ,  $\rho$  and porosity ( $\phi$ ), we can perform fluid substitutions using Gassmann's equation by first calculating the relevant bulk moduli (e.g. Mavko, Mukerji and Dvorkin 1998, p.169):

$$\frac{K_{sat}}{K_0 - K_{sat}} = \frac{K_{dry}}{K_0 - K_{dry}} + \frac{K_f}{\phi(K_0 - K_f)}; G_{sat} = G_{dry}$$

or:

$$K_{sat} = K_{dry} + \frac{\left(1 - \frac{K_{dry}}{K_0}\right)^2}{\frac{\phi}{K_{fl}} + \frac{1-\phi}{K_0} + \frac{K_{dry}}{K_0^2}}$$

or:

$$K_{dry} = \frac{X \cdot K_0}{1 + X}; X = \frac{K_{sat}}{K_0 - K_{sat}} - \frac{K_{fl}}{\phi(K_0 - K_{fl})}$$

where:

$K_{dry}$	=	bulk modulus of dry rock
$K_{sat}$	=	bulk modulus of rock with pore fluids
$K_0$	=	bulk modulus of rock at zero porosity
$K_{fl}$	=	bulk modulus of pore fluids
$\phi$	=	porosity (fractions)
$G_{dry}$	=	shear modulus of dry rock
$G_{sat}$	=	shear modulus of rock with pore fluids

This equation is valid for low frequency (<100Hz) deformations like seismic signals. As it appears, results are independent of the shear modulus. Values of  $K_{sat}$  and  $G_{sat}$  are estimated from  $V_p$ ,  $V_s$ , and  $\rho$  using the above equations. The zero porosity bulk modulus ( $K_0$ ) acts as a constant in the calculation and is found using the Voight-Reuss-Hill average of the individual components:

$$M_{VRH} = \frac{M_V + M_R}{2}$$

where

$$M_V = \sum_i f_i M_i$$

$$\frac{1}{M_R} = \sum_i \frac{f_i}{M_i}$$

where  $f_i$  and  $M_i$  are volume fraction and moduli of the  $i$ 'th component (Mavko, Mukerji and Dvorkin 1998).

When  $V_s$  is unknown, approximate methods as described by Mavko, Chan and Mukerji (1995) becomes the only alternative. The desired moduli changes resulting from changes in pore space compressibility are assumed to be equivalent to corresponding changes in Reuss type materials. This gives us the advantage that shear moduli can be assumed to be zero at high porosities and thus  $M_{sat} = K_{sat}$  such that relevant moduli can be estimated from impedance and porosity data directly.

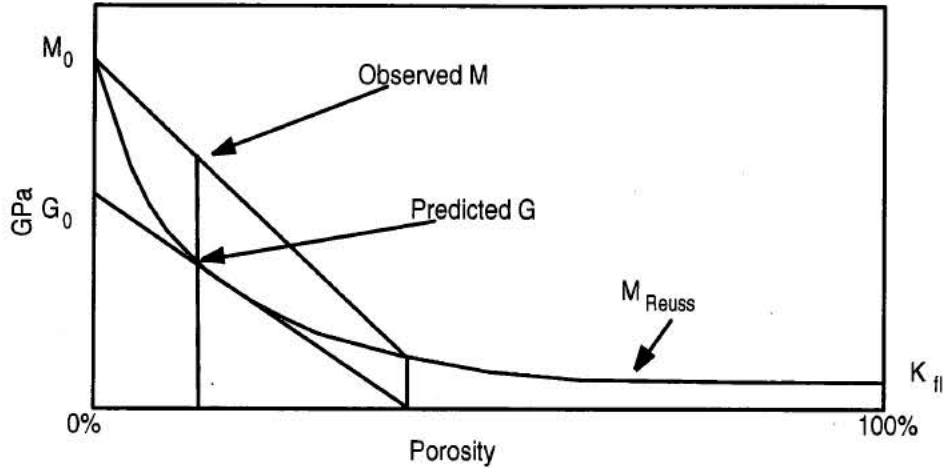


**Figure 27: Principle of the approximate method used here for estimating shear compressibilities.**

In this study the following method is applied: The shear modulus ( $G(\phi)$ ) is linearly interpolated between the incoherent type material (on the Reuss curve) where it is zero and the zero porosity type material where it is estimated from the mineral constituents properties (Fig. 27). This method seems to be the most robust (as compared to other methods quoted by Mavko, Chan and Mukerji, 1995) since it is not very sensitive to the expected errors in the porosity estimate as obtained directly from inversion.

First the special point where the extrapolation from  $M_0$  at zero porosity over  $M_{sat}$ , the observational modulus to  $M_{Reuss}$  (the modulus on the Reuss curve) is made. This point is estimated from:

$$\phi_R = \frac{\phi M_0^2 - M_0(1 + \phi)M_{fl} + M_{sat}M_{fl}}{(M_0 - M_{sat})(M_0 - M_{fl})}$$

Similar to values of  $M_{sat}$  a linear trend is assumed for  $G_{sat}$  in the range  $0 < \phi < \phi_R$ . Therefore  $G_{sat}$  can be estimated from:

$$G(\phi) = G_0 \left( 1 - \frac{\phi}{\phi_R} \right)$$

Because  $G(\phi_R)_{sat}$  is zero on the Reuss curve (non coherent material). Having thus obtained  $G(\phi)$ ,  $K(\phi)$  is estimated from:

$$K(\phi) = M(\phi) - \frac{4}{3}G(\phi)$$

We thus obtain all prerequisites for using the Gassmann equation. A key assumption is that  $M(\phi)$  and  $G(\phi)$  have the same functional form in the interval  $0 < \phi < \phi_R$ , which is equivalent to assuming that dry and mineral Poisson's ratios are the same.

## 4.2 Roar case

In our case porosities can be obtained from Ødegaard's porosity inversion. This "porosity" inversion assumes a one to one correspondance between inversion derived seismic imped-



ance and porosity as can be obtained from well data (see Fig. 31; Wagner 1999). The used porosities are therefore only approximative and gives rise to minor uncertainty. We obtain gross average fluid densities from RFT data (estimated to  $0.11 \text{ psi/ft}$  above the GOC/GWC and  $0.438 \text{ psi/ft}$  in the brine zone). It must, however, be emphasized that a substitution from pure gas to pure brine inevitably will result in overestimation of the substitution effect, since possible irreducible water saturations in the reservoir zone, that are disregarded, may reduce the difference. Since  $V_s$  is unknown, we use the above mentioned method where  $G(\phi)$  is indirectly estimated. We can then use traditional Gassmann calculations to obtain values for  $K_{sat}$  assuming different pore fluids, since  $G_{sat}$  is assumed to be unaffected by fluids. The fluid compressibility in the gas zone is calculated from the PVT laboratory estimated value of  $7.9 \cdot 10^{-6} \text{ psi}^{-1}$ . The average shale content is used to calculate  $K_0$  and  $G_0$  for the matrix using a Voight-Reuss-Hill average for the entire reservoir matrix rock. The mean shale content (bulk) is 4.4% with a mean porosity of 40 %. The resulting constants to be used in the Roar case are listed in Table 5. The upper four components are literature values from Walls, Dvorkin and Smith (1998), and the lower three components are the ones used in this study.

**Table 5: Material properties from Walls, Dvorkin and Smith (1998) and as used in the study (lower 3 components).**

Component	$K$ (GPa)	$G$ (GPa)	$\rho$ (g/cm <sup>3</sup> )
Calcite	65	27.1	2.71
Clay	20.9	6.85	2.58
Brine	2.627	0	0.997
Oil	0.997	0	0.650
Rock	59	24	2.70
Brine	2.627	0	1.0089
Gas condensate	0.873	0	0.2534

The fluid substitution calculation of the impedances is carried out for the reservoir zone above an average estimated GOC at 2027m SS. The oil zone is not included in the fluid substitution calculation since oil saturations are not very high (see later chapters) and because the effects from substituting oil with water on impedances is rather small.

An attempt to visualise the effect of the substitution is shown in Fig. 29, where the amplitude of the Top Chalk reflection is estimated by calculating the normal incidence reflection coefficient using

$$Rf = \frac{I_2 - I_1}{I_2 + I_1}; I_i = \rho_i \cdot V_p$$

The impedances were taken 2m above and below the Top Chalk surface to avoid errors relating to limitations in the high frequency content of the impedance data.

The reflection coefficient is calculated for the uncorrected seismic impedances for comparison with the Top Chalk amplitude map extracted from the seismic data (Fig. 9). The calculated map is based on the Danian impedance volume. The white areas to the Northwest and the East to Northeast therefore represent the areas where the Danian is removed (below seismic resolution) by erosion (Fig. 6). Comparison to the depth map shows that only the central portion of the field is affected by fluid substitution as defined by the 2027m depth contour (the GOC). The increased reflectivity centrally is obviously approaching the level

found outside the reservoir zone after the substitution calculation. A zone below the GOC where oil occur in modest saturations (see later chapters), which were kept out of the substitution calculation, has remarkably low amplitudes/reflectivity coefficients. This may be interpreted as a zone where oil has enhanced preservation of porosity. The preservation of porosity has apparently not occurred to the same extent neither in the gas zone, nor in the water zone.

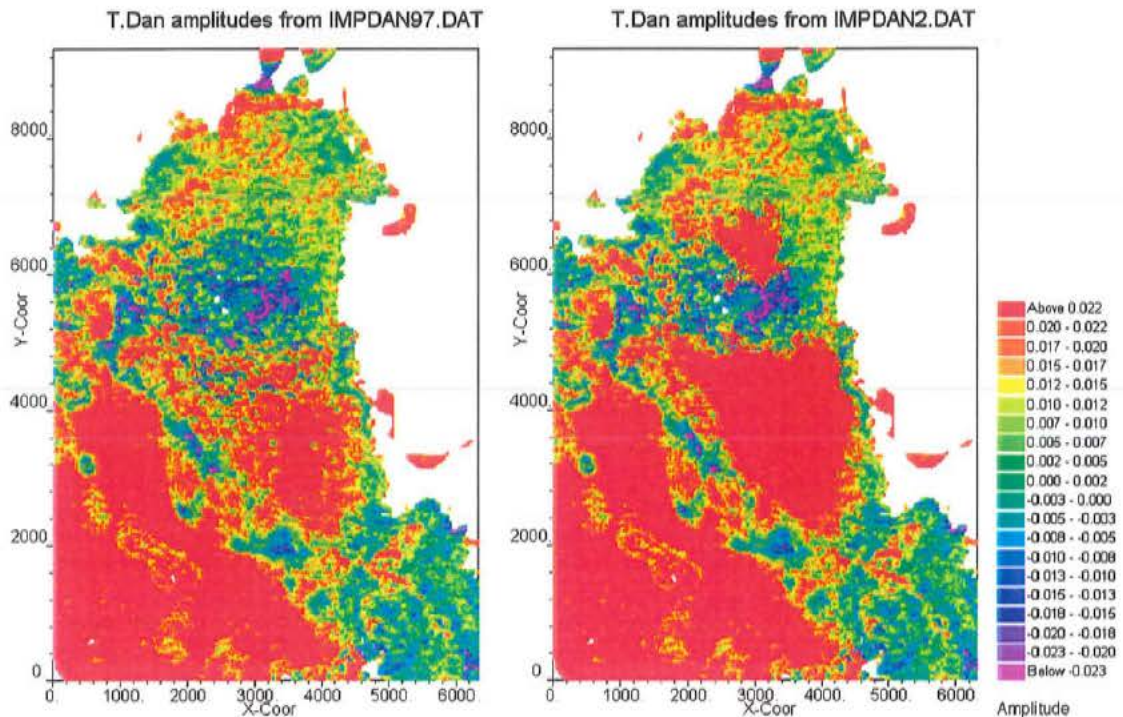


**Figure 28: Reflection coefficient map at Top Chalk level before and after fluid substitution.**

### 4.3 Summary on fluid substitution

The fluid substitution calculations show that the changes in amplitude at Top Chalk level is partly due to fluid changes. However, low or negative also occur where fluid effects are unlikely, which suggest preservation of abnormally high porosities. These high porosities are documented to occur by the well data.

The substitution calculation is based on an approximative method because shear wave data are not available. A likely source of error is that only single phase pore fluid compositions had to be assumed. This is probably causing to strong corrections towards the fluid contacts where multiple phase pore fluids are likely. Data for the oil zone could not be fixed and it was kept out of the calculation, because uncertainties in the substitution method are likely to overshadow the expected negligible effect of a change.

## 5. Geostatistical modelling

The geostatistical modelling is restricted to encompass the simulation of the porosity and permeability fields in this study. The applied method is stochastic simulation using a sequential gaussian co-located co-kriging technique (SGCOSIM; Deutsch and Journel 1992, Journel et al. 1992, and Xu et al. 1992). This method uses a soft (secondary) data set to support the prediction. The soft data set needs to have a value at all locations that are being simulated, hence the term co-located kriging. The modelling is carried out as two simulations; the first focuses on simulation of the porosity field, where the soft data are the inversion derived seismic impedances; the second focuses on simulation of the permeability field where the soft are constituted by the porosities simulated in the first step. In this way the link between porosity and permeability is preserved. The method can honour the well data, utilise soft data to the degree that it correlate with the parameter of interest, a target histogram can condition the simulation, and it can reproduce the spatial coherency of a parameter as given by variograms.

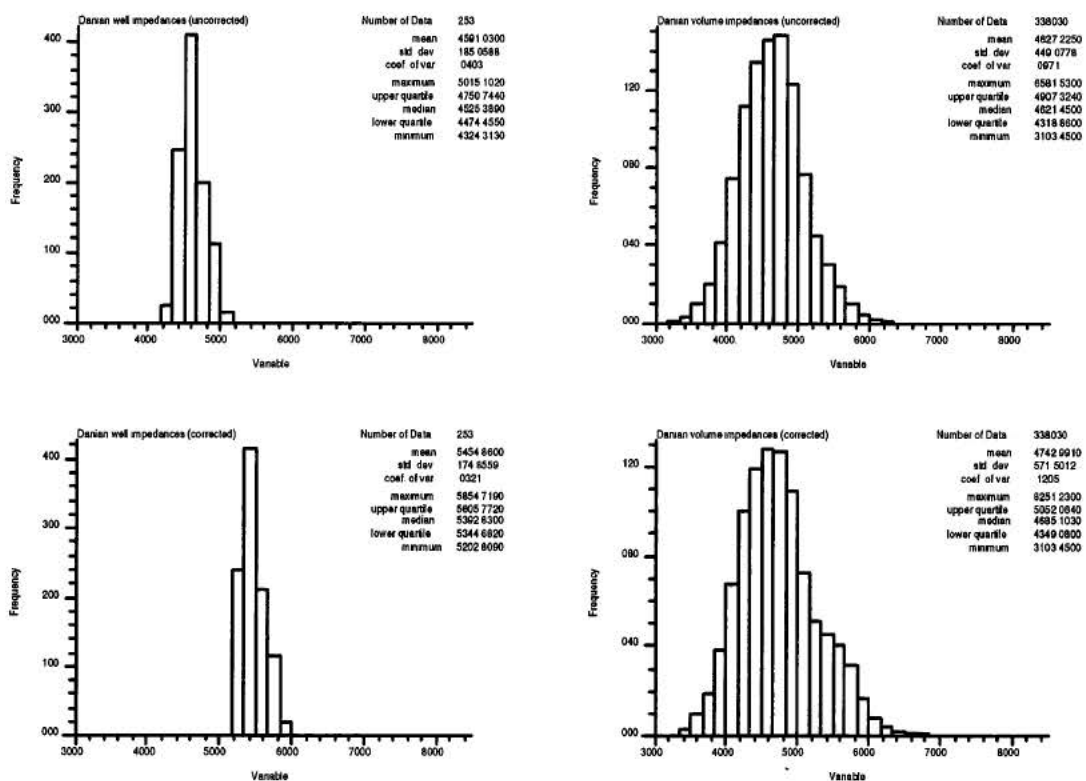


**Figure 29: Impedance distribution in the Danian. Total populations before and after fluid substitution calculations, and the corresponding populations as obtained by backinterpolation to well data points (cells checked by wells).**

Before simulation, both primary and soft data need to be transformed into gaussian populations (normal score distributions). This transformation removes skewness or other non-gaussian features in the data populations, which is re-introduced to the simulation results by back-transformation afterwards (Deutsch and Journel 1992). The problem about estimating



the shape of the population distribution (the shape of the histogram) for the entire volumes (the target population) on the basis of only very few well data points should be handled during this transformation. The small well data base is unrepresentative but is still the main clue to the target population . This problem is handled by model based declustering as described by Frykman and Deutsch (1996), - it is thus kept outside of the simulation procedure itself. and is detailed below.

## 5.1 Porosity simulation

The porosity distribution is modelled with the support of inversion derived impedances as soft data. This approach relies on a (albeit weak) correlation between porosity and seismic impedance, which is warranted by the rather uniform rock type in this study. This correlation shall be found with well data porosity versus inversion derived seismic impedances because they are used in simulation and not impedances as calculated from well data. Because of a too small population in this study, the previously estimated correlation coefficient of -0.45 is used (Vejbæk 1995).

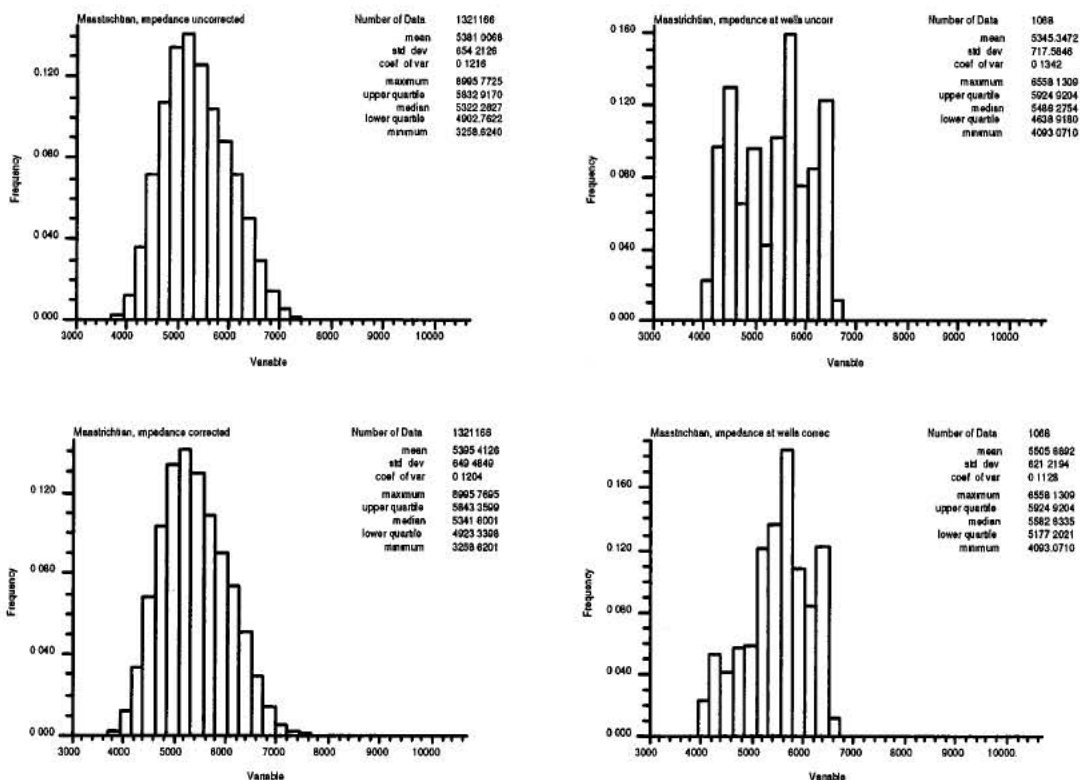


**Figure 30: Impedance distribution in the Maastrichtian. Total populations before and after fluid substitution calculations, and corresponding populations for cells checked by wells.**

The inversion derived impedances are also used to obtain a first impression of how representative the porosity population given by well data is, as compared to the target population (porosity in the entire simulation volume), because of the correlation to seismic impedance. Inspection of the impedance histograms (Figs. 29 and 30) shows that the well data have

somewhat higher median impedances as compared to the entire population. This well data bias mainly applies to the Danian unit, and is negligible for the Maastrichtian unit. This shows that the target porosity population for the Danian is expected to have somewhat higher mean or median porosity than the well data because of the inverse relationship between seismic impedance and porosity. The bias in the well data is getting more pronounced after the fluid substitution calculation is carried out as seen in the lower set of histograms in Figs. 29 and 30.

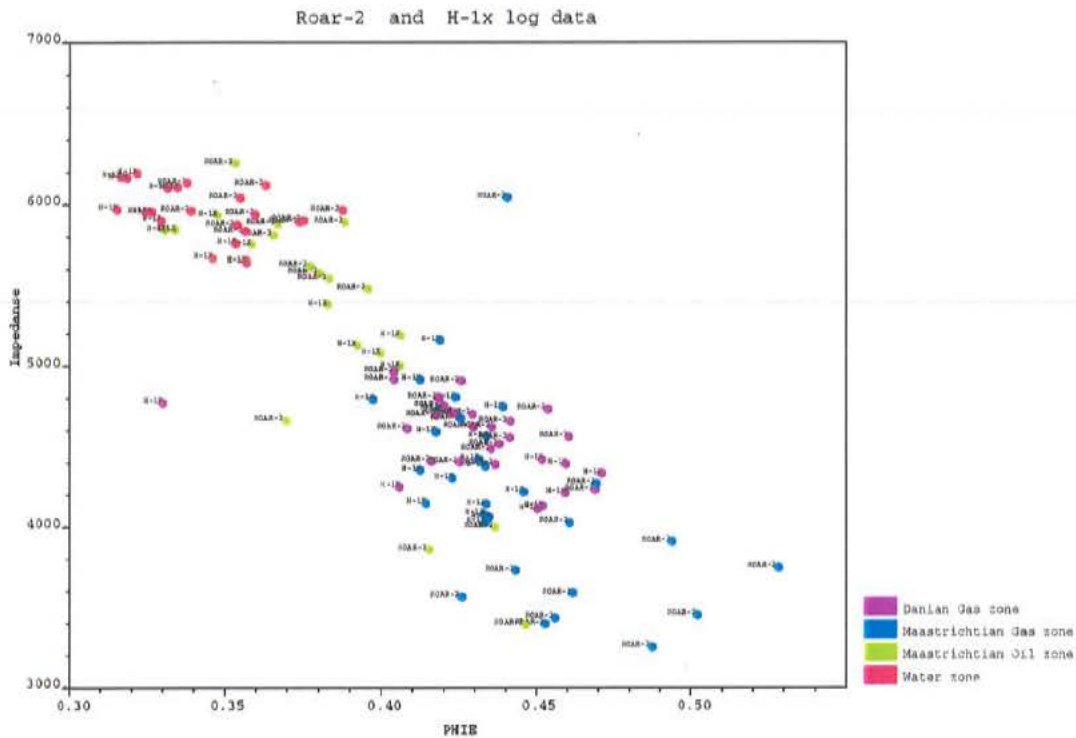


**Figure 31: Crossplot of log derived impedance and porosity from the H-1 and Roar-2a wells. The colour coding shows the reservoir zone of origin.**

The rather clear delineation of the reservoir by the seismic amplitude map (Fig. 9) suggests that a simple relationship between seismic impedance, and porosity may not exist, but that also variations in fluid compositions influence impedance. This seems to be contradicted by a crossplot between log derived seismic impedance and log derived porosity shows that only minor scatter around a simple inverse relationship exist, irrespective of the presence of gas, oil or water, and even irrespective of Danian or Maastrichtian chalk.

There is a clear tendency for gas zone data points to plot with low impedance and high porosity, but still a clear inverse relationship between impedance and porosity irrespective of the fluid content. Since the presence of gas does not break down the porosity/impedance relationship, it could be surmised that the seismic anomaly is primarily an effect of higher porosities being preserved by hydrocarbons. The occurrence of low amplitudes and even phase reversals close to the DHI and somewhat higher amplitudes in the crest area suggests that the presence of oil enhances porosity preservation relative to gas in the Roar Field. However, since inversion derived seismic impedances are intended for use as soft data in the SGCOSIM method applied here, these impedance are only used for this purpose

after fluid substitution calculations as described previously. This is also prudent with respect to obtain results that are consistent between the gas, oil and water zones. The fluid substitution correction has not been applied to log derived seismic impedances, but it seems likely that for example the Maastrichtian gas zone data points on Fig. 31 would move up during such a correction and thus improve the correlation in that plot.

The validity of the interpreted porosities from log data is confirmed by the combined plots of log porosities and core analysis data given in enclosures 1 and 3. The porosity distribution interpreted from petrophysical logs shows remarkably high porosities in general as compared to for instance the Dan Field data (e.g. Frykman 1996; Vejrbæk and Kristensen 1999; Fig. 32)

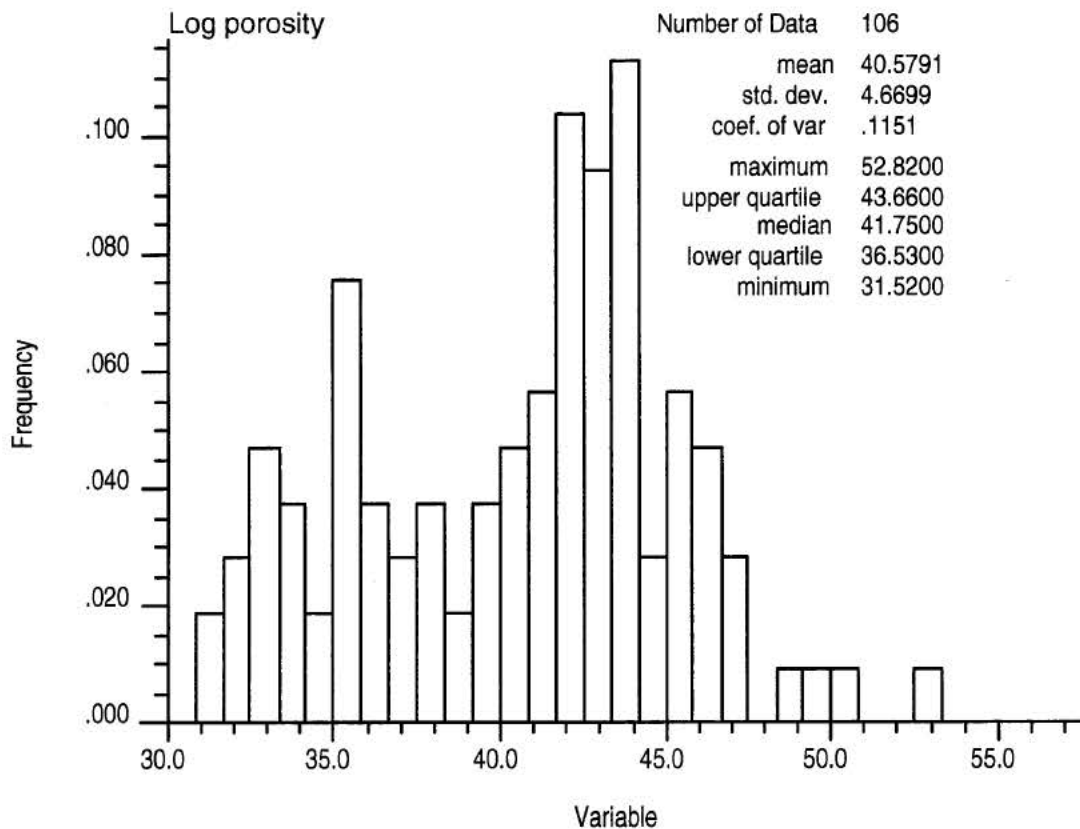


**Figure 32: Histogram of log-derived porosities from Danian and Maastrichtian both from H-1X and Roar-2.**

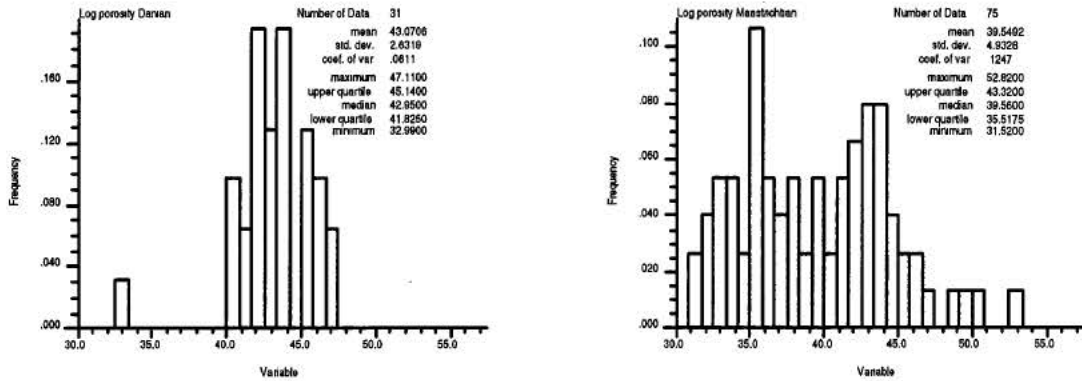


**Figure 33: Log derived porosities divided into the Danian and the Maastrichtian por-tion.**

When porosity data are separated into Danian and Maastrichtian, it is seen that these two populations mainly differ in terms of spread. The Danian has a narrow distribution with one relatively low value originating from uppermost in the H-1 well. The Maastrichtian has a rather wide distribution, with a lower mean than for the Danian, but still with higher porosities than for the Danian. For this reason it could be speculated that the porosity simulation could be simulated for the Danian and the Maastrichtian combined in one batch.

However, due to differences in the porosity permeability relationships for the Maastrichtian and Danian, the simulations needs to be subdivided into the two units (e.g. Frykman 1996). The simulation grid specifications for these two units are given in Table 6, and the relation-ship to world co-ordinates are given in Table 2.

**Table 6: Simulation grid dimensions.**

Dimension	Cell size	No. cells.	Size
X (West to East)	25m	253	6325m
Y (South to North)	25m	373	9325m
Z (Danian)	6m	11	66m
Z (Maastrichtian)	6m	14	84

The two simulation grids constitute 1038059 and 1321166 cells for the Danian and Maas-trichtian volume respectively, totalling 2359225 cells. The simulation grids are Cartesian (orthogonal axes and no topography), which have been flattened from stratiform topography. This is done because spatial continuity is assumed to be highest along bedding surfaces and smallest perpendicular to bedding planes and because the simulation is aimed at repro-ducing this variation in spatial continuity. This flattening is performed by the use of the Top Maastrichtian surface for both volumes, which is equivalent to assuming that the internal bedding planes in the Danian and Maastrichtian are conformable with this surface. The thickness variation in the Danian are thus assumed to be caused by Post Danian erosion (Fig. 6). A substantial part of upper portion of the Danian volume therefore needs to be cut away after simulation.



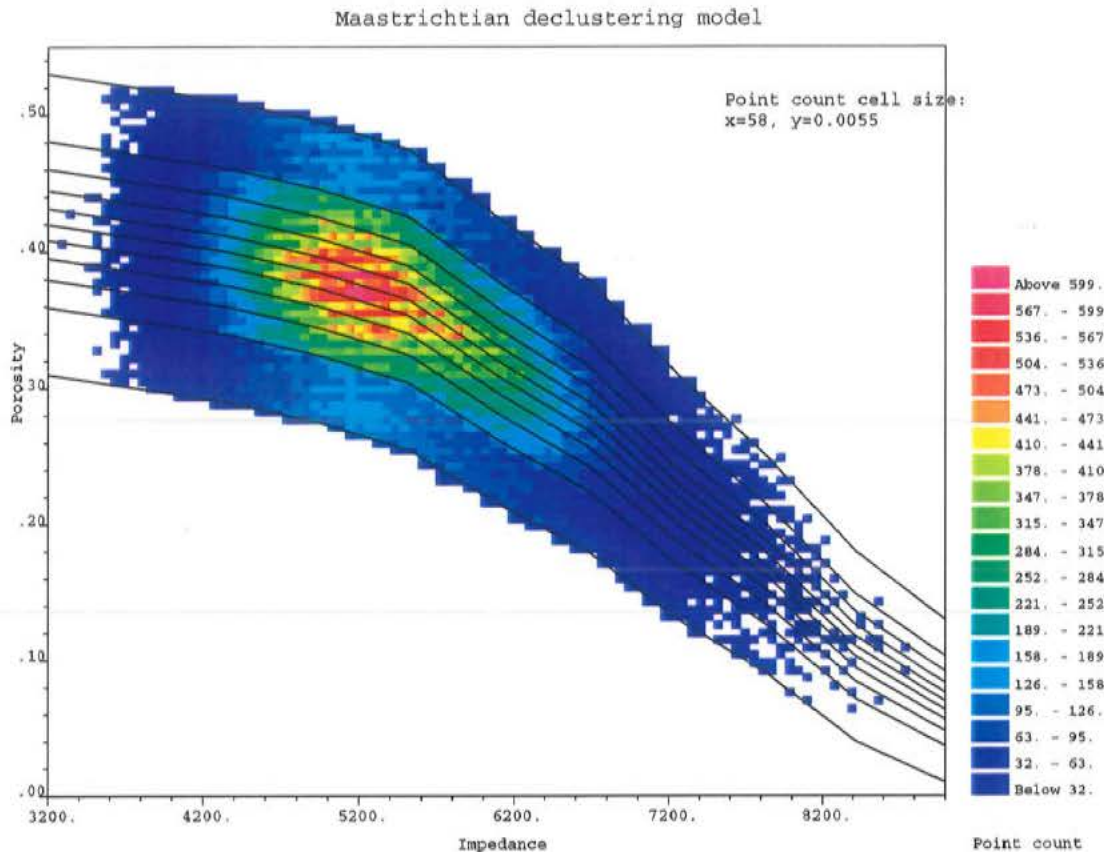


**Figure 34: Maastrichtian porosity declustering model. The constructed target population of 330327 points is shown as colour coded point density.**

The very modest well data base as compared to the number of cells that are to be assigned porosity and permeability values (the target populations) calls for means to bridge the gap in population size (3 orders of magnitude). The very few well are highly unlikely to have captured the entire width and shape of the porosity populations that occur in the rock volumes to be simulated. To overcome this problem, model-based de-clustering was applied to subjectively construct a likely porosity population for the entire volume, here called the target population (e.g. Frykman & Deutsch 1996; Vejrbæk 1996) and as described by Vejrbæk and Kristensen (1999). Based on the moderate correlation between log porosity (hard data) and inversion-derived seismic impedance (soft data) decile (10 % fractile) lines are subjectively drawn in a cross plot of these quantities, encompassing the soft data span, and guided by the available hard data. These lines define the likely porosity span that may occur for a given impedance value. The histograms resulting from the SGCOSIM simulation as shown in Figs. 36 and 37, indicate some success in the reconstruction, but also some discrepancies. In both the Danian and especially in the Maastrichtian, deviation occur because of excess data in the high and the low end. This is due to the larger populations in the final volumes than the constructed populations, and because especially the Maastrichtian volume is suffering from a vertical trend imposed by the soft data (seismic impedances) resulting in high porosities in the top and low porosities in the bottom.



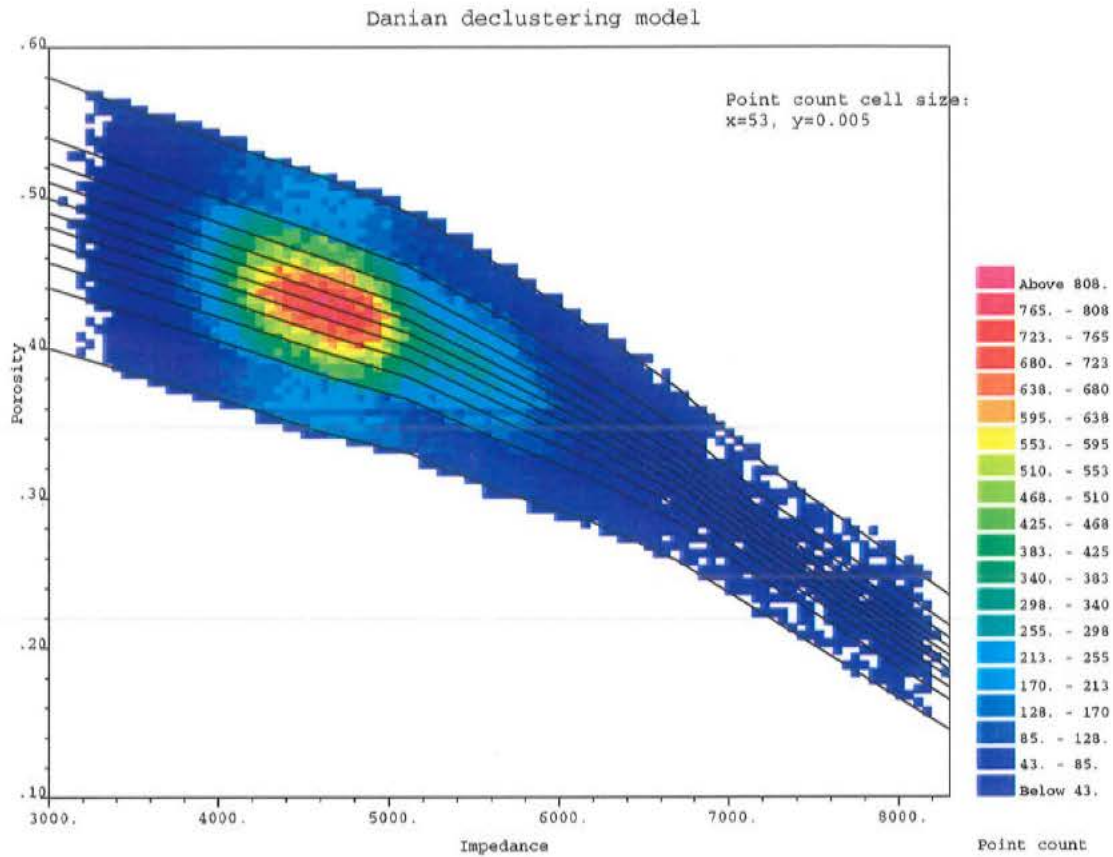


**Figure 35: Danian porosity declustering model. The constructed target population of 338030 points is shown as colour coded point density.**

Soft data (seismic impedances) are present at all locations to be simulated and thus provide valuable information on the porosity population that may be expected in the entire simulation volume; i.e. the target population. The target porosity population is then produced by randomly selecting porosity values so that they honour the designed decile bands. The target porosity population is produced by using all, or a major part of, the soft data. In this way the scatter in the porosity impedance relationship is reproduced (Figs. 34, 35).

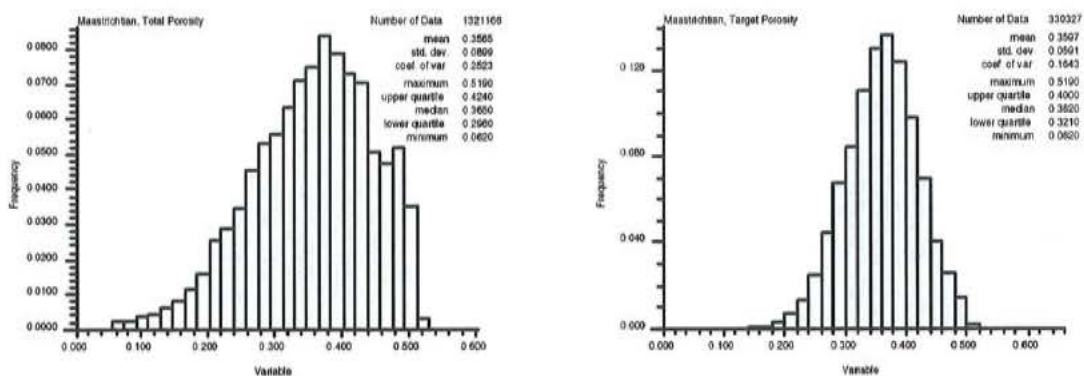


**Figure 36: Histograms of the resulting simulated (left), and the constructed target porosity populations for the Maastrichtian (right).**

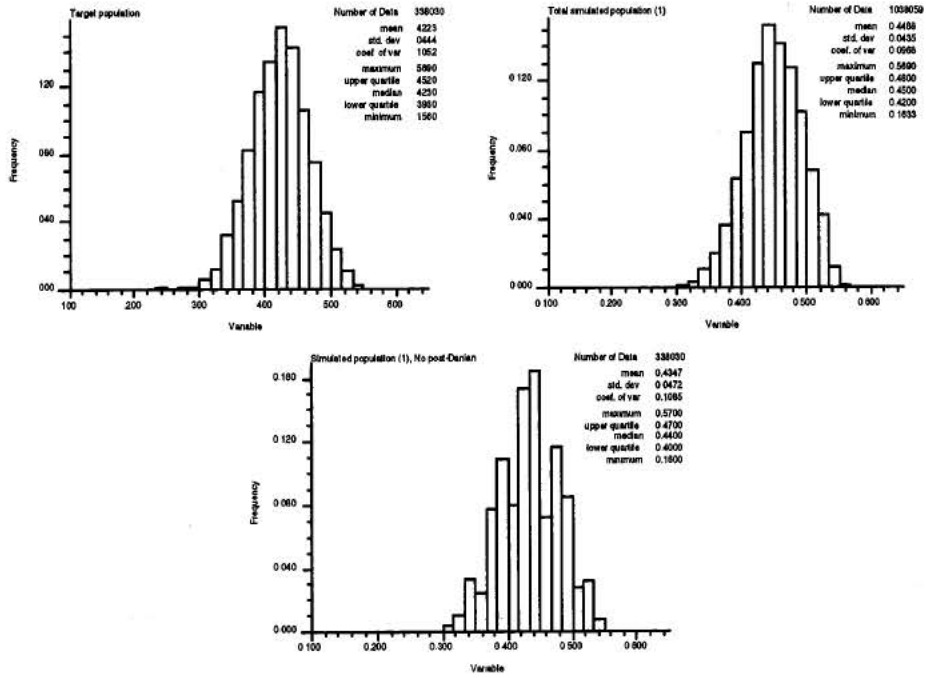


Figure 37: Histograms of the constructed target porosity (left), the resulting simulated porosity (middle), and the simulated porosity without the Post Danian (right).

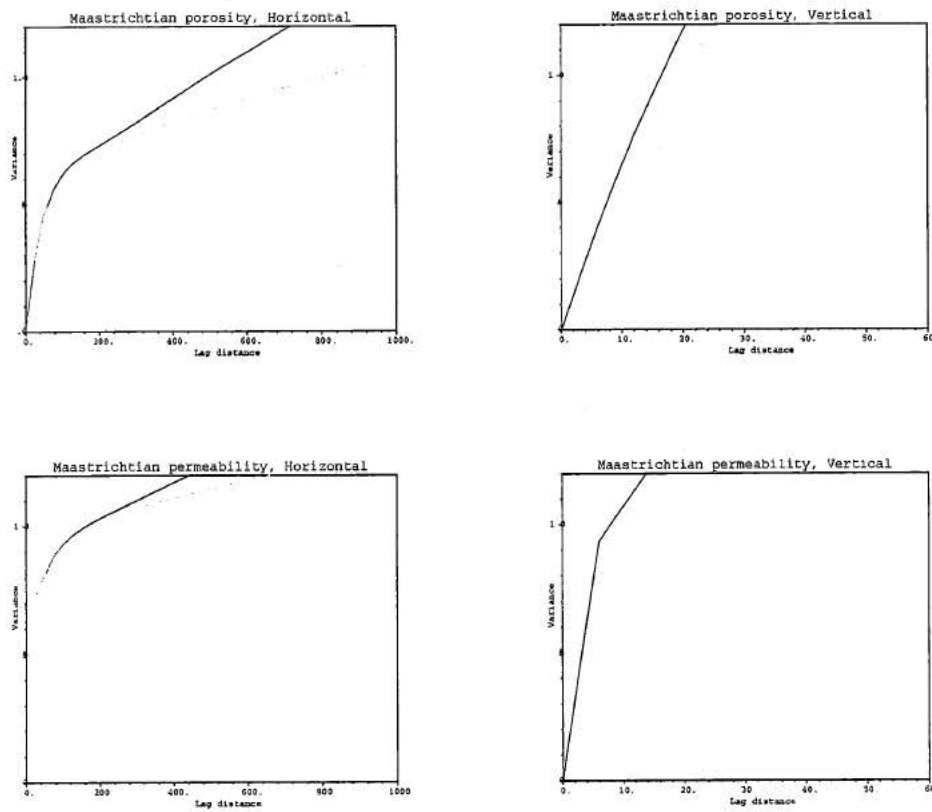
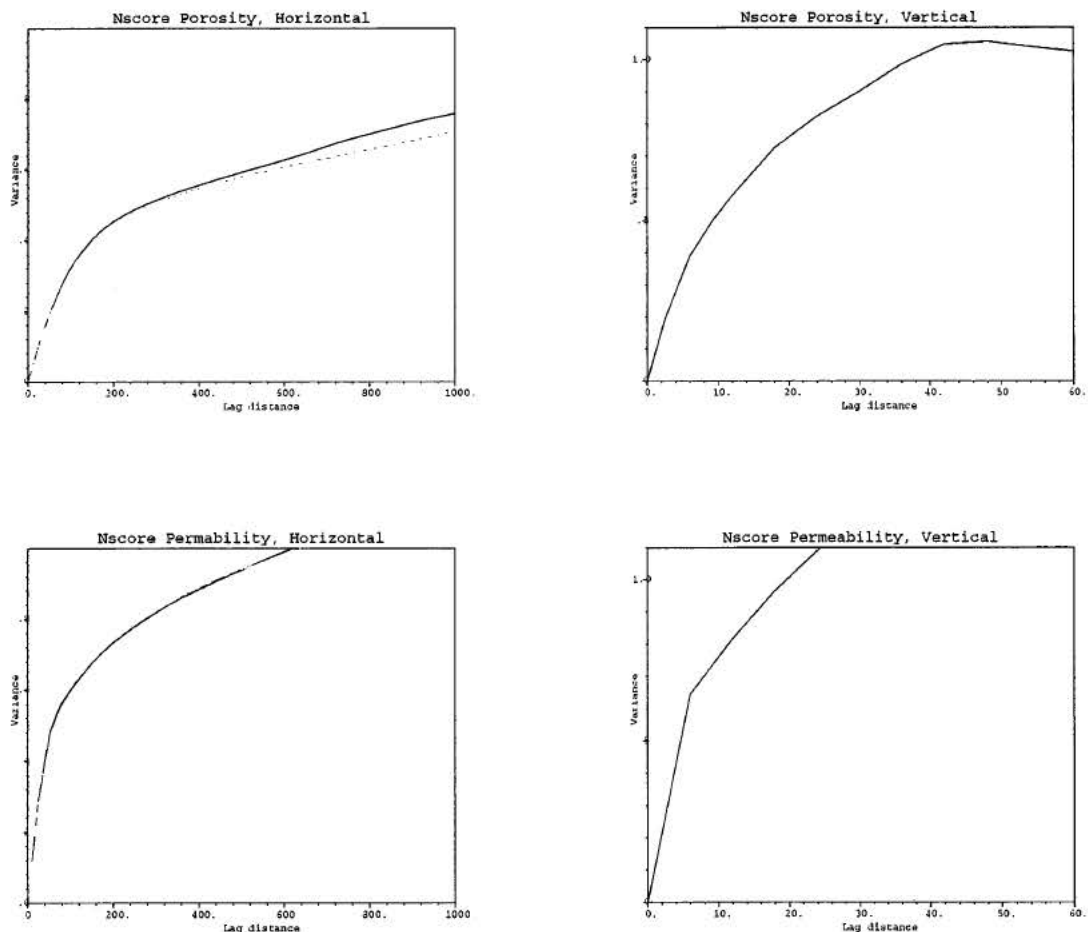


Figure 38: Variograms for the Maastrichtian calculated on simulation results. Compare with variograms specified in Table 7

With only two wells available, experimental variograms (especially the horizontal ones) are also bound to be very poor, and render model variograms ill supported. For this reason, the model variograms are based on comparison to data from other chalk fields; primarily the Dan Field (e.g. Vejrbæk and Kristensen 1999) combined with plots of the few available experimental variogram points. The resulting variograms are shown in Table 7.

**Table 7: Model variograms for porosity simulation based on normal score transformed data.**

Unit	Variogram type	Horizontal range	Vertical range	Sill
Danian	Spherical	180	10.8	0.476
	Exponential	1700	104	0.524
Maastrichtian	Spherical	100	25	0.786
	Exponential	1000	10	0.214



**Figure 39: Variograms for the Danian calculated on simulation results. Compare with variograms specified in Table 7.**

The resulting bivariate behaviour in the impedance porosity domain is not exactly honouring the constructed target population bivariate behaviour. However, since the SGCOSIM procedure is not explicitly conditioned on the bivariate population, this does not give cause for



major concern. The majority of the points are also within the designed decile bands, as indicated by the colour coded point densities. It is seen that the points falling outside the declustering design bands are point-clouds of low density (Fig. 40). Results of the porosity simulation are also illustrated with the porosity maps in Fig. 41 and 42, which represent vertical averages of the simulation result over the portion of the Maastrichtian that is located above the approximate gas oil contact, and the entire Danian respectively. It is noteworthy that porosities seems generally higher in the Danian, than in the Maastrichtian as is also seen from the histograms in Figs. 36 and 37.

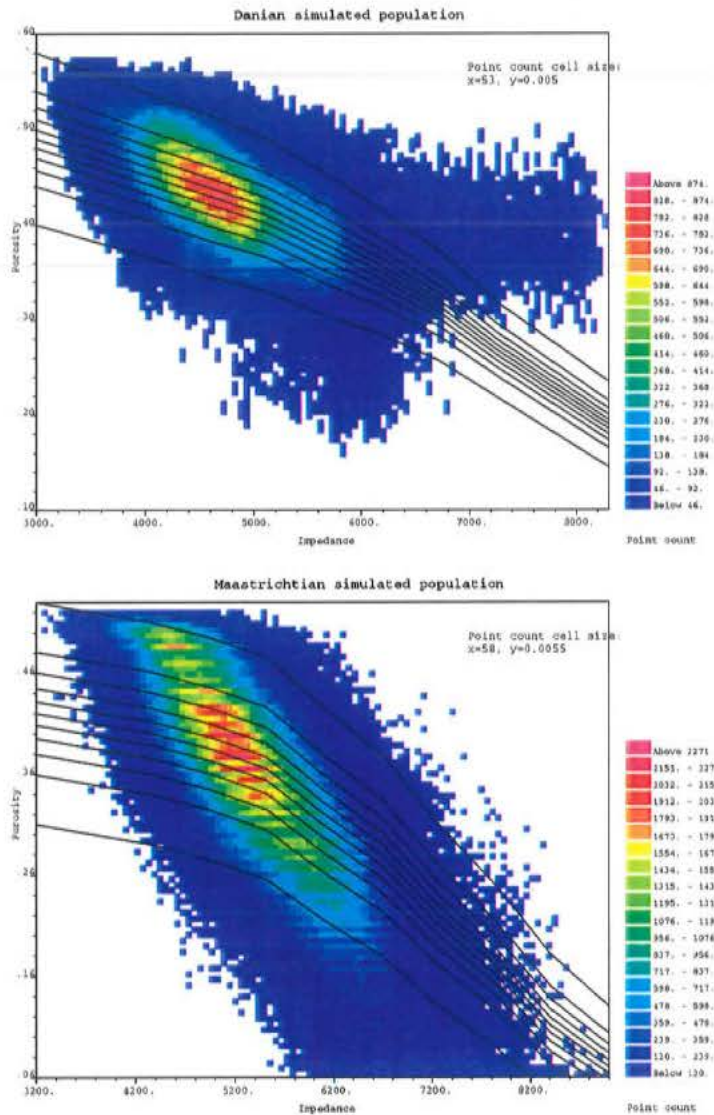


**Figure 40: Bivariate behaviour of the simulated porosity versus impedance.**

It is obvious that there is a tendency for higher porosity to occur in the southwestern portion of the central Roar reservoir; both for the Danian and the Maastrichtian unit. This may not be by mere chance, but because the crest of the field may have been shifted to the Southwest in Middle to Late Miocene times as discussed previously. An early hydrocarbon accumulation may thus have helped preserve porosity in that part of the field by curbing diagenesis. The higher porosities occurring Northeast of the field in the Maastrichtian unit may be identical to the channel feature previously recognised on the basis of seismic attribute analysis

(Abatsiz and Kerr 1989). These streaks of high porosity is thus explained by reworking of the chalk.

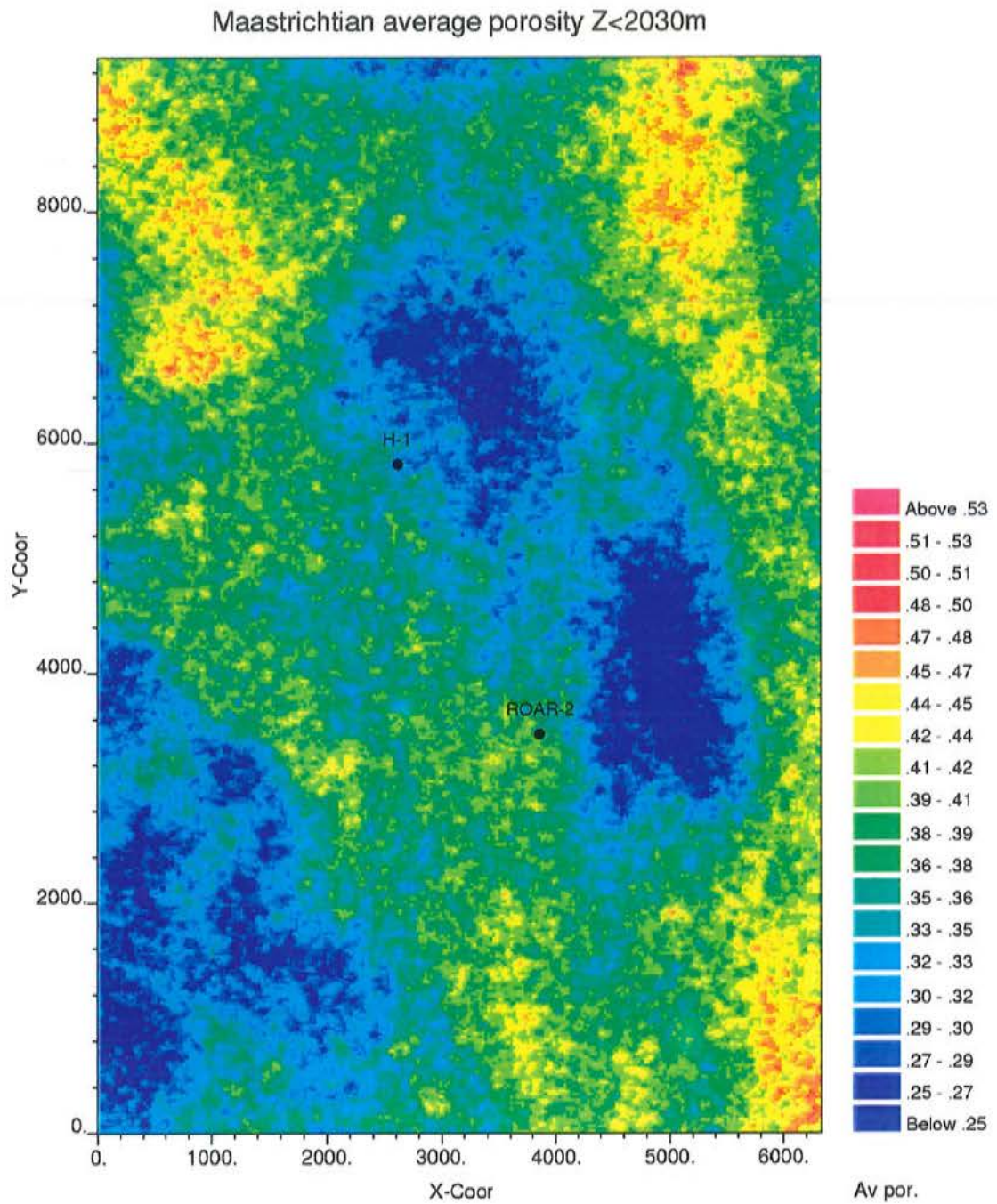
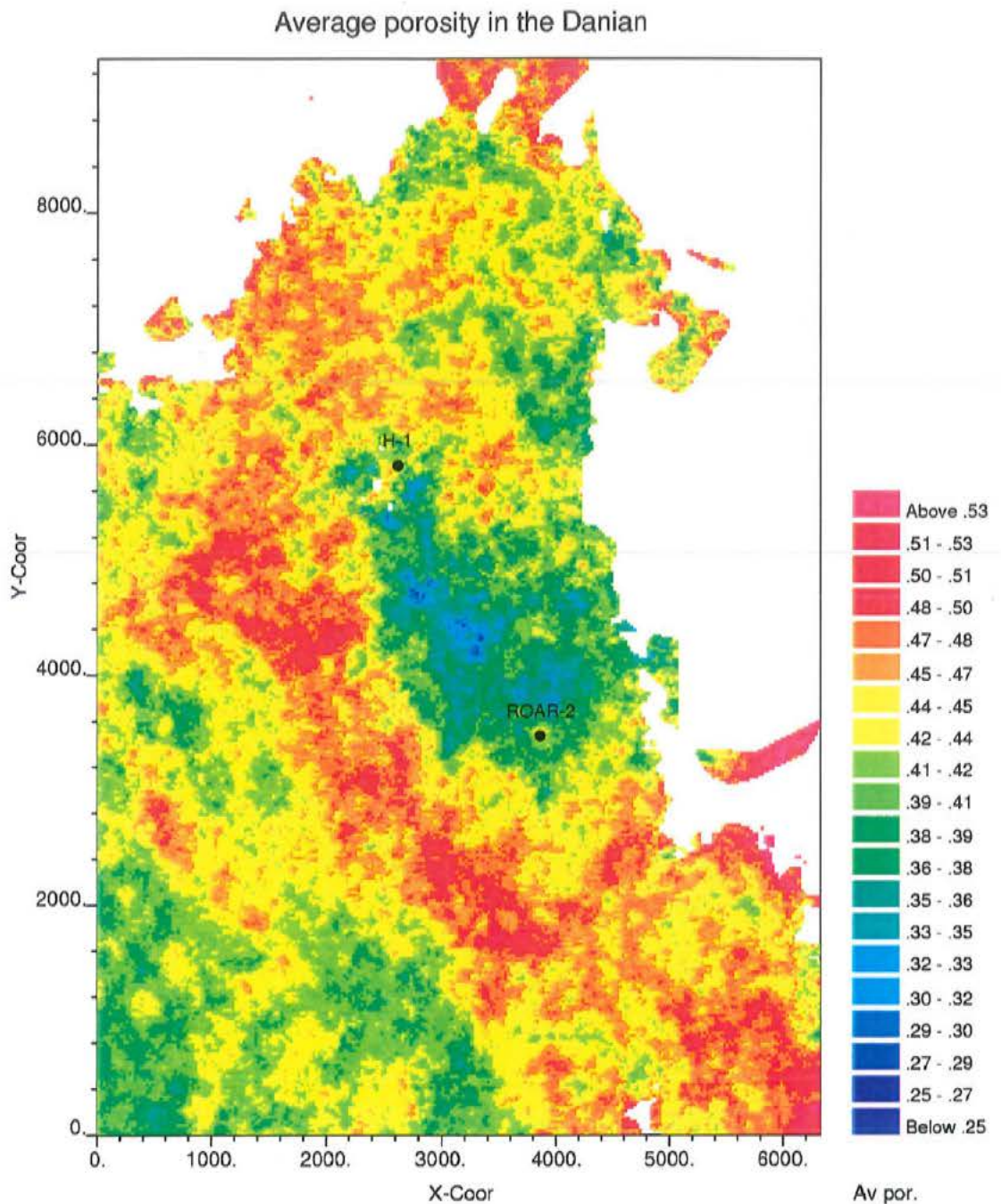


Figure 41: Maastrichtian simulated average porosity above 2030 m (app. the GOC; sim. 2).





**Figure 42: Danian simulated average porosity.**



## 5.2 Permeability

The simulation of the permeability fields is similar to the process involved with simulating the porosity, except that the soft data is constituted by the previously simulated porosity instead of seismic impedances. The availability of permeability data requires the availability of core material. Therefore the permeability data base is much more limited than porosity data, which are based on petrophysical log interpretation.

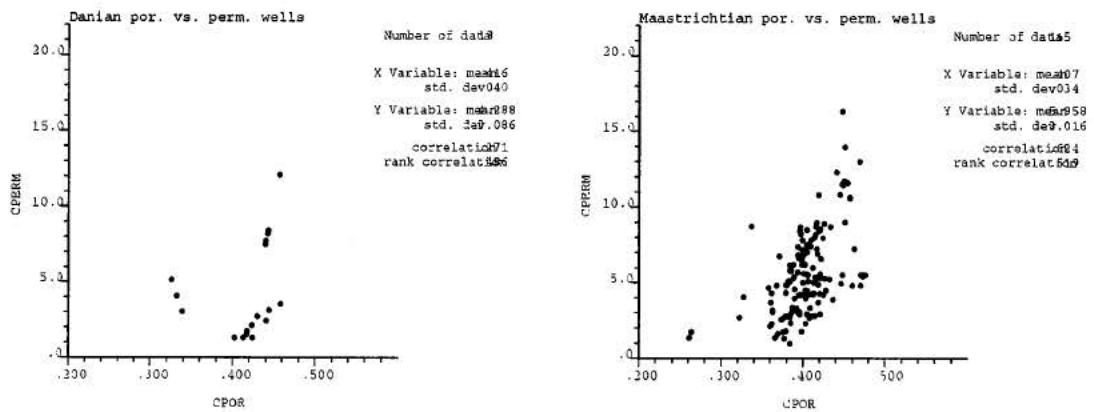


**Figure 43: Porosity versus permeability from core data.**

The core data from the Maastrichtian unit may give some hints on the shape of the bivariate population, whereas the Danian population is much too limited. It is, however clear that the Maastrichtian permeabilities have a higher mean than the Danian, as is also seen in other part of the North Sea (e.g. Frykman 1996).

Also in this case the target population is constructed with the use of the soft data population (Figs 44 and 45). The hard data are too few to guide the constructed declustering model, which is subjectively drawn on the basis of an assumed positive correlation with a tendency to a semi-logarithmic dependency. This is seen in the curved appearance of the designed decile bands.

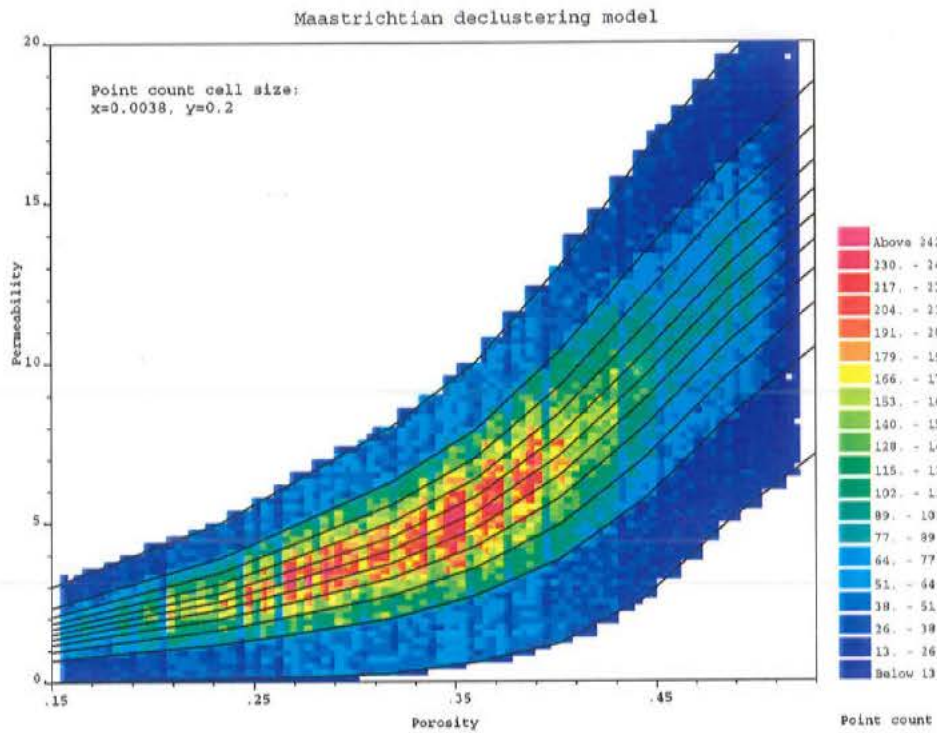


Figure 44: Construction of target population of permeability based on the simulated porosity population for the Maastrichtian.

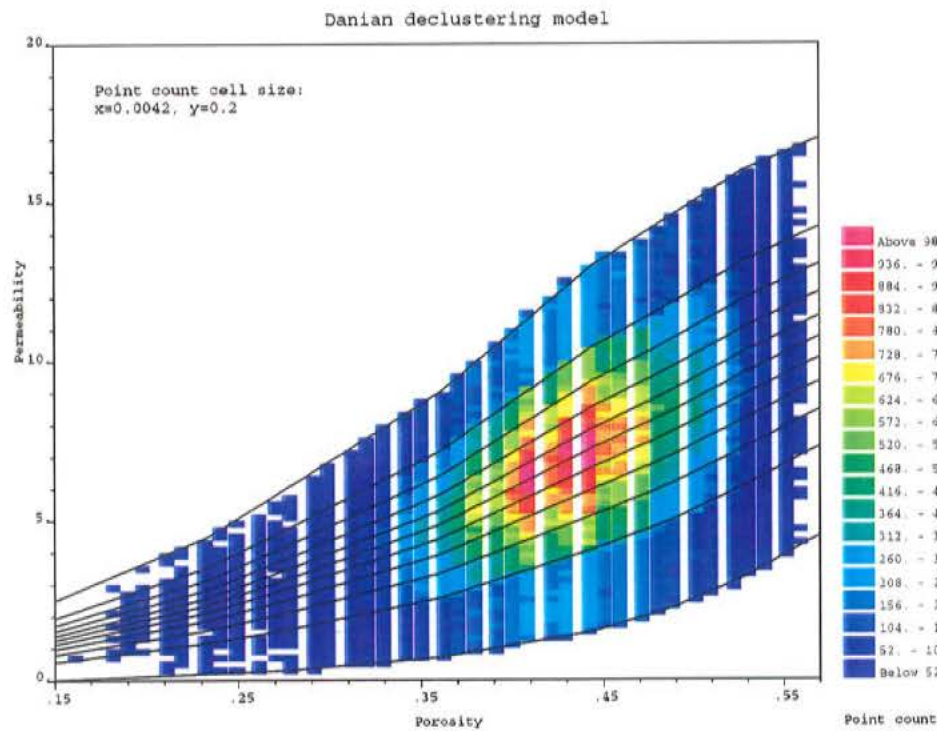


Figure 45: Construction of target population of permeability based on the simulated porosity population for the Danian.

The histograms resulting from the declustering are shown in Figs 46 and 47 together with the resulting modelled populations. The histograms are right skewed as is expected with the field being dominated by low permeable rocks. The simulated population has the same right skewed appearance, but apparently with “extra” data in the high and low ends. One main reason is that the simulated population is about 4 times larger than the constructed target population. Another reason is the influence of the soft data, which has a very wide distribution.

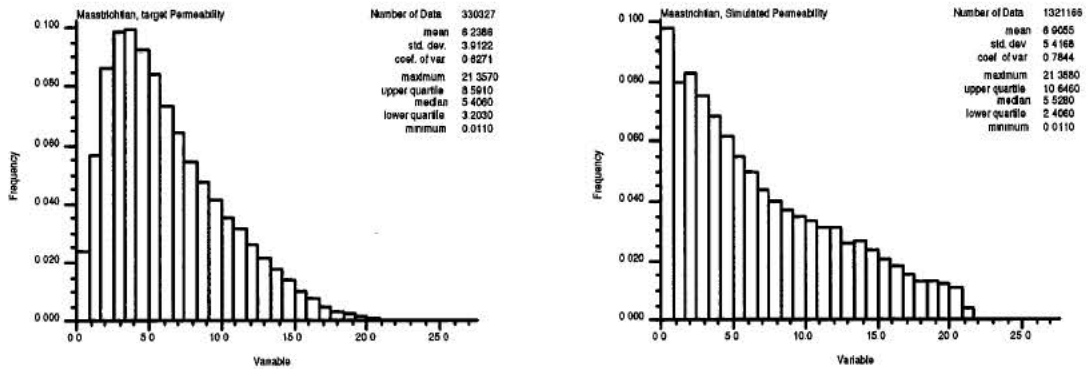


Figure 46: Histograms of the simulated and modelled Maastrichtian populations.

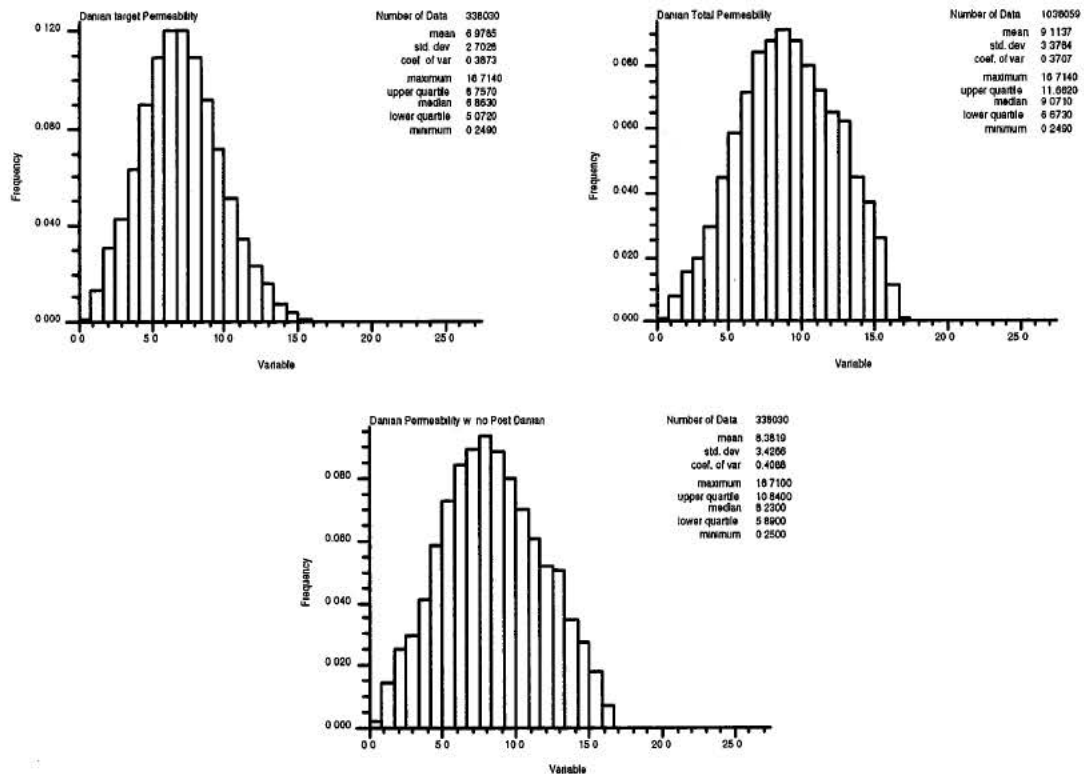


Figure 47: Histograms of the simulated and modelled Danian populations.

The permeability variograms are even worse defined than the porosity variograms and are set to have ranges about 1/3 of the porosity variograms based on experience.



**Table 8: Model variograms for permeability simulation based on normal score transformed data.**

Unit	Variogram type	Horizontal range	Vertical range	Sill
Danian	Spherical	60	3.6	0.476
	Exponential	566	34.66	0.524
Maastrichtian	Spherical	30	7.5	0.786
	Exponential	300	3	0.214

The resulting bivariate behaviour of the permeability simulations are shown in Fig. 48. It is seen that a rather wide scatter occur, especially with the Maastrichtian. Again this is attributed to strong trend in the porosity simulation, but also because of the wide scatter in the porosity simulation. It is, however, noteworthy that the main point densities (green to red colours) plot very similar to the Dan Field core data shown in Fig. 49.

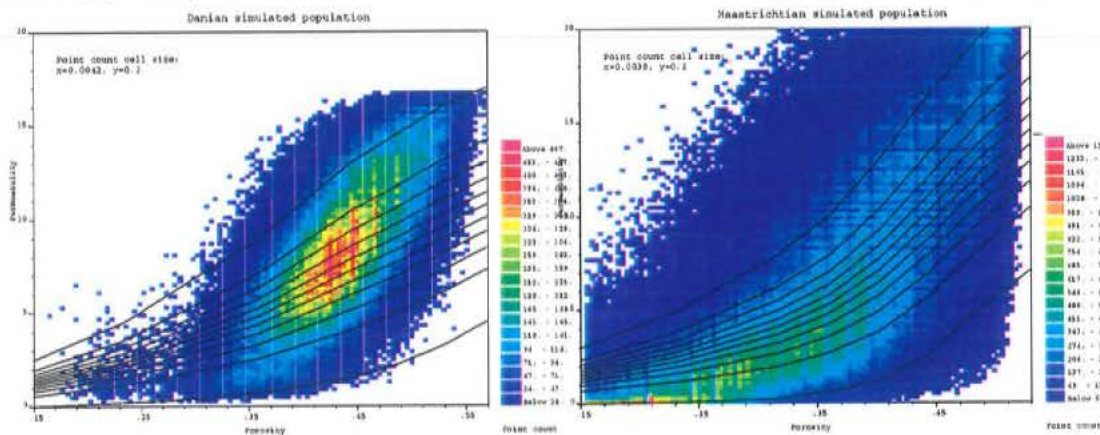


**Figure 48: Bivariate behaviour of the simulated permeability/ porosity populations.**

### 5.2.1 Permeability anisotropy

The resulting permeability maps represent arithmetic means of cells of the size 25-25-6m. These cells have a finer internal structure in nature, which is an important information that is lost by assuming uniform cells. As there is a correlation between porosity and permeability, a visual inspection of the porosity logs (see enclosures) leads to the supposition that the lost fine structure is a fine scaled horizontal layering. The lost fine scale structure is equivalent to the short range component in the vertical variograms. The fine structure is likely to introduce a permeability anisotropy on a scale of the simulated cells, because high permeable laminae will dominate horizontal flow whereas low permeable laminae will dominate vertical flow. The horizontal permeability ( $K_h$ ) is thus equivalent to the arithmetic mean of the permeability distribution within the cell:

$$K_h = \frac{1}{n} \sum_n K$$

which is exactly the result of the permeability simulation described above. The vertical permeability ( $K_v$ ) is however, equivalent to the harmonic mean:

$$\frac{1}{K_v} = \frac{1}{n} \sum_n \frac{1}{K}$$

which is not found directly through the simulation. This quantity is here estimated through the estimation of the  $K_v/K_h$  ratio. This is done through the following steps:

1. Porosity permeability relationships are estimated for the Danian and the Maastrichtian.
2. Permeability logs are calculated using these relationships on the basis of representative porosity logs for the Danian and the Maastrichtian.
3. Log blocking: The porosity logs are blocked using arithmetic means, and the permeability logs using both arithmetic and harmonic means. The blocks are 6 m high corresponding to the simulation cell size.
4. Calculate and plot the resulting  $K_v/K_h$  ratios versus blocked porosity.
5. Perform least squares approximation of the function that relates porosity to  $K_v/K_h$ .
6. Calculate  $K_v$  volumes using simulated porosity and permeability ( $K_h$ ) using the above function.

The functions used for the porosity to permeability relationship and the porosity to  $K_v/K_h$  relationship are all of the form:  $Y = aX^b$ . Due to the limited core analysis database on the Roar field, data from the Dan Field has been used for estimating the porosity permeability functions for the Danian and the Maastrichtian (Table 9; Fig. 49; Frykman 1996).

**Table 9: Coefficients for the porosity to permeability relationship functions.**

	a	b
Danian	$1.060919 \cdot 10^{-10}$	6.55
Maastrichtian	$1.85 \cdot 10^{-4}$	2.9

The function applies to permeabilities (Y) in  $mDarcy$  and porosity (X) in percent.

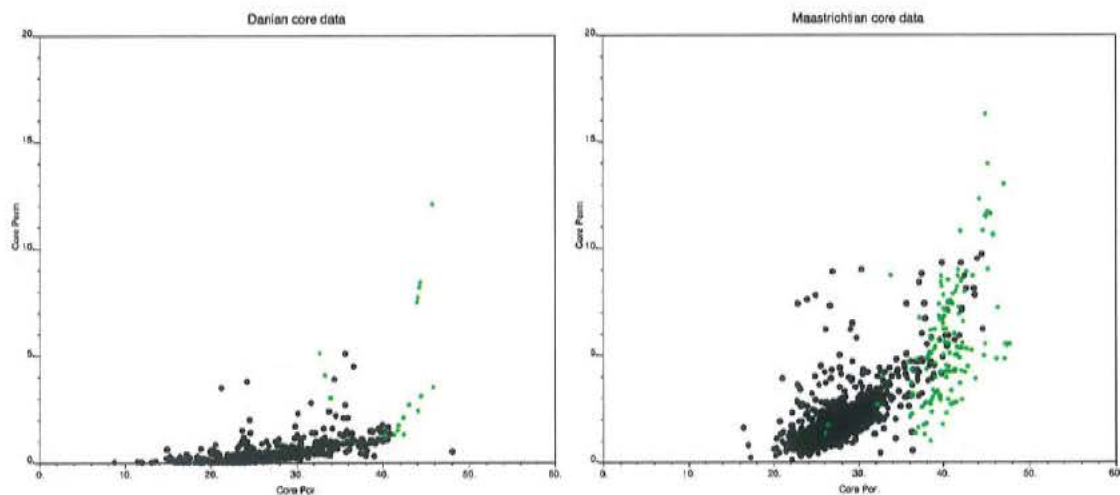


**Figure 49: Dan Field core data in black, and Roar Field core data in green. Compare Figs 48 and 50.**

Both representative logs from the Dan Field and the Roar Field were used to obtain a span in the in resulting porosity vs.  $K_v/K_h$  populations. The plot shown in Fig. 49 which shows Dan Field core analysis data for Dan units 1 through 4, and Maa units 1 through 6 (Kristensen et al. 1995) also demonstrate the remarkably high porosities and permeabilities found in the Roar Field as compared to the Dan Field. The two fields are located at similar depths. A possible explanation could be an earlier invasion of hydrocarbons in the Roar Field, which is closer to the major likely source area: The Tail End Graben.

With a sufficient span in data, the coefficients for the functions that relate Porosity (X) to  $K_v/K_h$  (Y) could be determined as listed in table 10.

**Table 10: Coefficients for estimating the  $K_v/k_h$  ratio.**

	a	b
Danian	0.3605267	0.2332772
Maastrichtian	0.8321941	0.04564551

As is evident from the plot of these functions, anisotropy is negligible in the Maastrichtian, but is quite important in the Danian, and may even contribute to a partial compartmentalization of the reservoir in a Danian and a Maastrichtian unit.

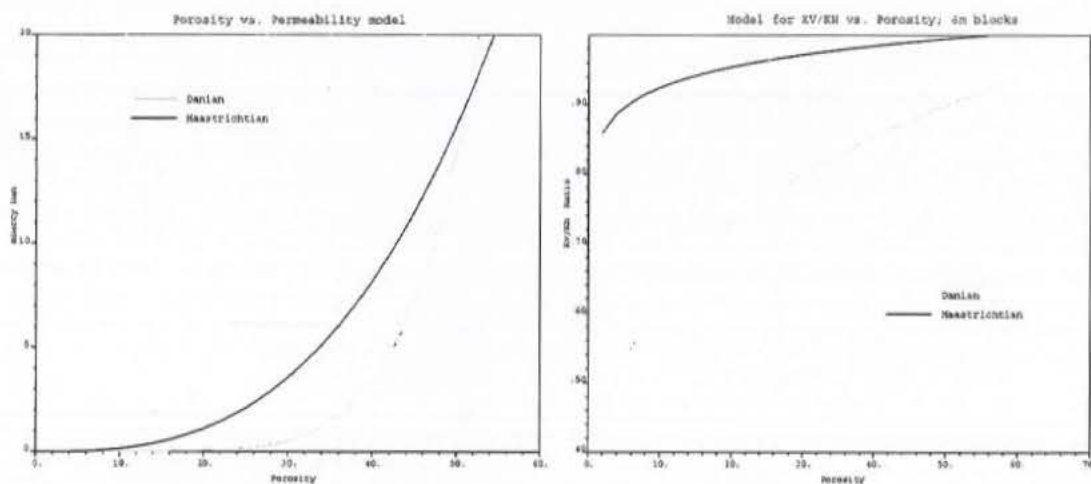


**Figure 50: Por.-Perm model used for permeability log construction and the resulting  $K_v/K_h$  porosity models.**

The effect of the anisotropy calculations is exemplified with the basal Danian permeability maps shown in Fig. 51. A general reduction in vertical permeabilities as compared to horizontal permeabilities is noted.



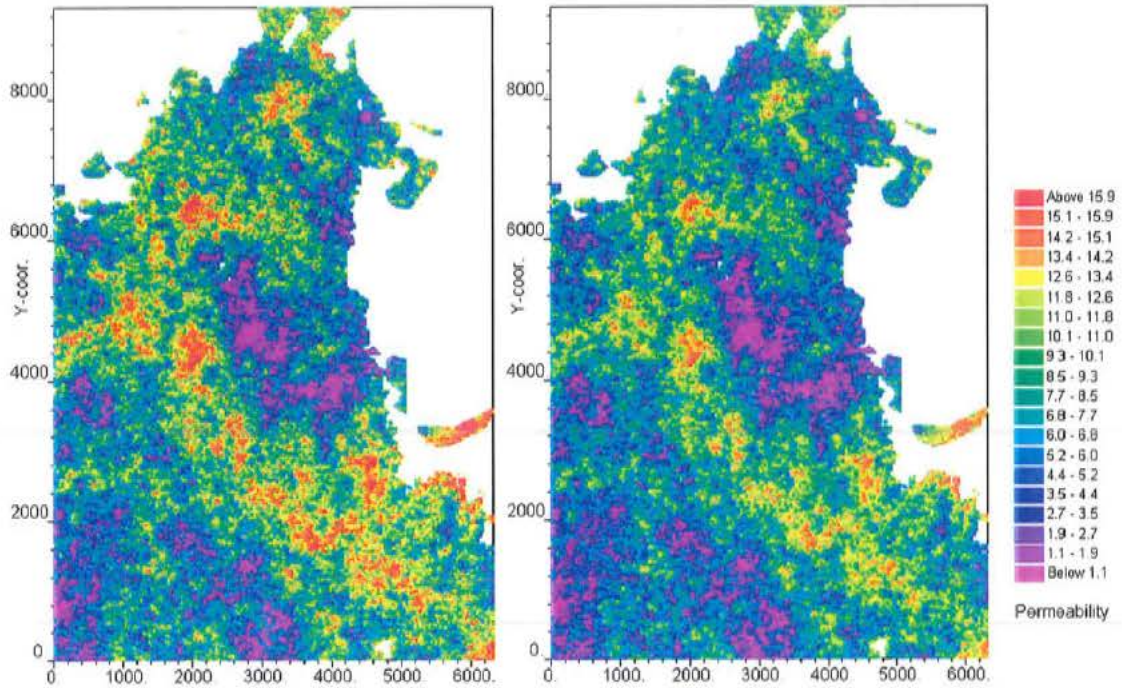


**Figure 51: Permeabilities 3m above the base of the Danian (basal cell layer). Horizontal to the left (Kh; arithmetic cell means), and vertical to the right (Kv; harmonic cell means).**

The thus deduced  $K_v/k_h$  ratios may, however, yield too low anisotropy values, because even the porosity logs represents a vertical averaging in the order  $\frac{1}{2}$ ' to 1' (0.3 to 0.6 m) at least. If sufficiently laterally continuous low/im-permeable layers exist below this thickness, then anisotropy may be even higher.

## 6. Saturation modelling

In order to investigate the impact of the variations between the reservoir models on estimates of hydrocarbons in-place, saturation modelling is done also. For this purpose, the normalized capillary pressure curve method, also called the equivalent radius method (EQR) as developed by Engstrøm (1995) for North Sea chalk is applied. This method performs very well on the very tight chalk reservoirs and seems to be universally applicable to Danish North Sea chalk reservoirs. The method addresses the observation that HC saturation in water wet chalk reservoirs seems to be significantly affected by:

- Porosity dependent irreducible wetting phase saturation (increasing with decreasing porosity).
- Porosity dependent capillary entry pressures (increasing with decreasing porosity).
- Capillary pressures depend on porosity rather than permeability.
- Chalk type; the above dependencies are different for Danian and Maastrichtian chalk.

According to Engstrøm (1995) Danian and Maastrichtian chalk in the Danish North Sea may be assumed to obey each their universal porosity dependent functions describing irreducible water saturations and describing capillary entry pressures.

The irreducible water saturation ( $S_{wir}$ ) is found to be related to porosity ( $\phi$  fractions) according to a function that may be described by:

$$S_{wir} = \left( \frac{a}{\phi} \right)^b$$

Likewise the capillary entry pressure ( $P_{ce}$ ) may be given by a similar function:

$$P_{ce} = \left( \frac{a'}{\phi} \right)^{b'}$$

Using these types of functions, the findings of Engstrøm (1995) can be matched using the constants  $a$ ,  $b$ ,  $a'$  and  $b'$  as listed in Table 11.

**Table 11: Constants for the  $P_{ce}$  and  $S_{wir}$  functions.**

	$a$ ( $S_{wir}$ )	$b$ ( $S_{wir}$ )	$a'$ ( $P_{ce}$ )	$b'$ ( $P_{ce}$ )
Danian	0.12641	2.45422	50.31562	1.16118
Maastrichtian	0.06596	2.19565	79.89612	0.96581

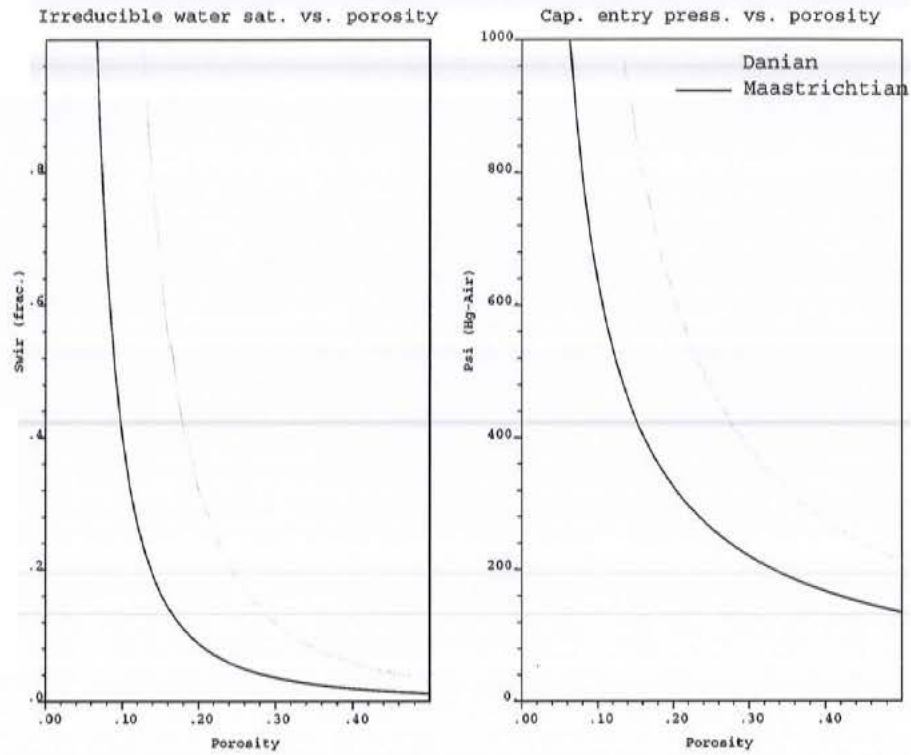


**Figure 52: Irreducible water saturation and capillary entry pressure (Hg-air system) models for the chalk.**

The shapes of the universal functions are shown in Fig. 52. The constants for the capillary entry pressure ( $P_{ce}$ ) function apply to a laboratory Hg-air system and need to be converted to the oil-water or gas-water systems of this study. In this study the interfacial tension ( $\sigma \cos \theta$ ) is assumed to be 367, 26 and 70 *dynes/cm* for the Hg-air, the oil-water and the gas-water systems respectively.

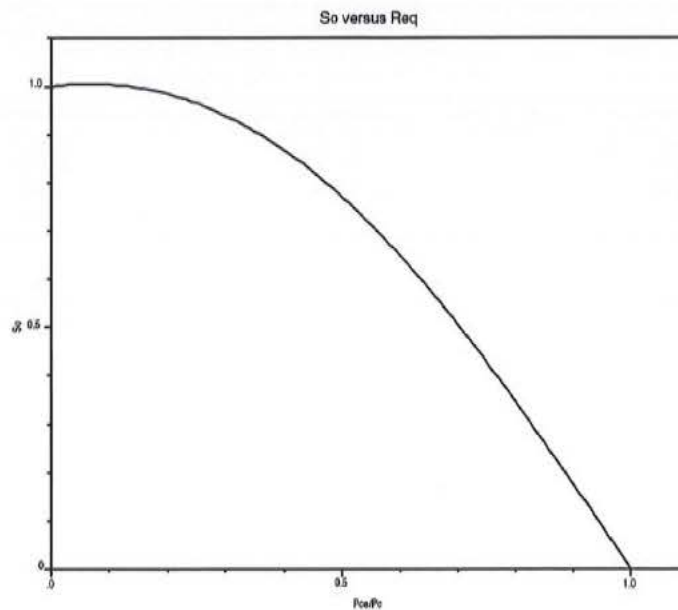


**Figure 53: Equivalent radius versus normalized non-wetting phase saturation.**



The first two interfacial tensions are standard CoreLab values, and the latter is fitted to data guided by comparison to literature values (Leverett 1940; McGaffery 1972). For simplicity, only two phase systems are assumed in the gas and oil zones of the reservoir.

Another assumption in the EQR method is that the ratio between capillary entry pressure and capillary pressure (the equivalent radius:  $r_{eq}(S_o) = P_{ce} / P_c$ ) is independent on porosity and chalk type, but only on the non-wetting phase saturation ( $S_{on} = (1 - S_w) / (1 - S_{wir})$ ).

This interdependency is determined from laboratory Hg-air experiments and converted to an oil-water system (Fig. 53). The results are fitted to a 6th order polynomial:

$$S_o(r_{eq}) = \sum_{n=0}^6 a_n r_{eq}^n$$

where the coefficients  $a_n$  are given in Table 12.

**Table 12: 6th. order polynomial coefficients to conversion function between Normalised non-wetting phase saturations and equivalent radius values.**

	$a_0$	$a_1$	$a_2$	$a_3$	$a_4$	$a_5$	$a_6$
$r_{eq}(1-S_o)$	0.99123	1.16999	0.77362	0.20941	-0.02337	-0.00629	0.00215
$S_o(r_{eq})$	0.99995	0.14049	-0.98882	-0.68924	0.42734	0.22699	-0.11668

The capillary pressure in  $Psi$  ( $P_c$ ) within the reservoir is found from the differential pressure between the two fluids:

$$P_c = (FWL - Z) * \frac{(\alpha_{br} - \alpha_{hc})}{0.3048}$$

where  $FWL$  is the free water level (in  $m$ ),  $Z$  is the depth (in  $m$ ),  $\alpha_{br}$  and  $\alpha_{hc}$  are brine and hydrocarbon pressure gradients (in  $psi/ft.$ ). RFT data from the Roar field shows that  $\alpha_{br}$  and  $\alpha_{hc}$  are 0.438 and 0.11  $psi/ft$  in the water and gas zones respectively. The oil zone does not show up on RFT data, which only display pressures consistent with brine densities. This may be due to low oil saturations in the oil zone. An estimate of 0.33  $psi/ft$  is used for calculating capillary pressures in the oil zone in this study.

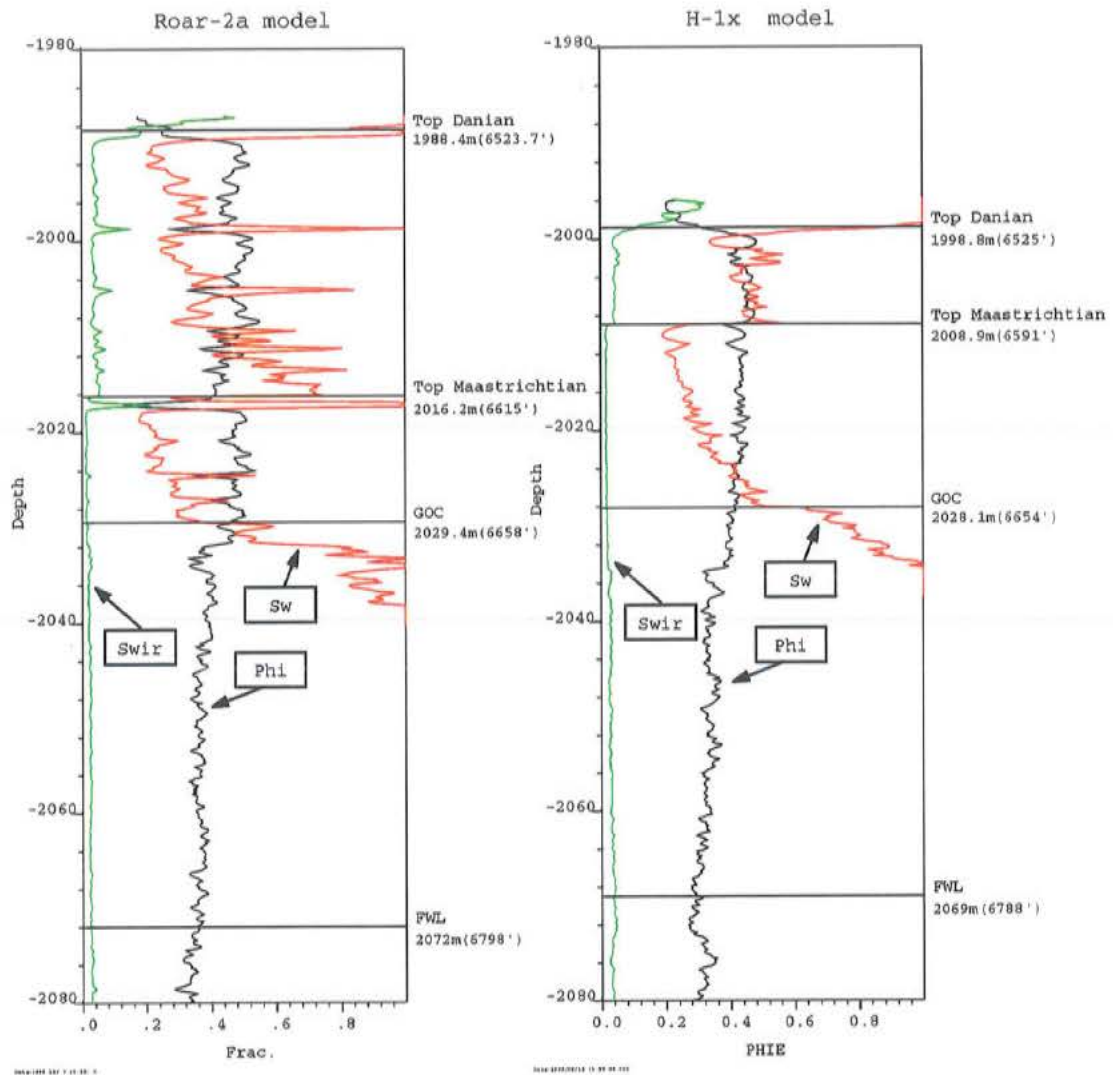


**Figure 54: Modelled Sw for the Roar -2a and H-1x wells.**

The model was first applied to the Roar-2a and H-1 wells in order to calibrate the parameters. Calculated saturations were found to be acceptable with FWLs of 2072 m (6798') 2069 m (6788') in the Roar-2a and H-1x wells respectively. This corresponds to a southerly dip of 3 m between the wells or approximately 12 m over the entire length of the model window (9.3 km). Similarly the GOC is dipping to the south about 1.3 m from 2028.1 m (6654') at H-1 to 2029.4 m (6658') at Roar-2a as reported from well observations. In order for these dips to be mutually consistent, the pressure difference resulting from 3 m difference in FWL (using oil and water pressure gradients) shall correspond to the pressure difference resulting from the GOC difference (using gas and oil pressure gradients). They do not correspond exactly with an error that can be estimated to either 0.008 psi/ft in the oil gradient, 0.3 m in the FWL, or 0.17 m in the GOC over a distance of 2.5 km. These discrepancies are all considered to be within acceptable limits.

Applied to the porosity simulation results, the hydrocarbon pore volumes (HPCV) are calculated for the combined Maastrichtian and Danian reservoirs as listed in Table 13. The hydrocarbon pore volume is calculated from :

$$HCPV = \sum_{i,j} \Delta x \cdot \Delta y \cdot (\sum_n \phi \cdot (1 - S_w) \cdot \Delta z)$$

where  $i,j$  is the number of cells in  $x$  and  $y$  dimensions,  $n$  is the number of layers and  $\Delta x$ ,  $\Delta y$  and  $\Delta z$  are the cell dimensions.

**Table 13: Hydrocarbon pore volumes calculated using the EQR-So model.**

Simulation no	1	2	3	4	5	6	7	8	9	10
HCPV ( $\cdot 10^6 m^3$ )	22.03	19.69	20.81	20.67	21.04	21.18	21.92	22.10	22.14	21.89

Most parameters are associated with uncertainty, but 3 are just unknown, that accordingly are used as calibration parameters. These 3 unknowns are the interfacial tension in the gas zone, the oil pressure gradient and the free water level. The results as listed in Table 13 show some scatter from 19.69 to 22.14  $\cdot 10^6 m^3$  with the same simulation and model conditions. The only difference being the seed numbers for the simulation.

An example of a HCPV map is shown in Fig. 55. Most hydrocarbons are clearly found in the southern part, which is mainly an effect of greater height of the hydrocarbon column that causes higher HC saturations. An effect of porosity variations is also seen in southern part of the field. The area with most hydrocarbons is slightly shifted to the Southwest relative to the axis of the structure which is an effect of southwestwards increasing average porosities (compare Figs. 41 and 42).

Due to the flatness of the structure as may be seen on the profile in enclosure 7, it is evident that these results are strongly susceptible to errors/uncertainties in depth conversion, determination of FWL, and GOC. With limited difference in porosity there is still large differences in saturations as seen in the well data (Fig. 54), which shows that there is not sufficient height above to FWL (and thus differential pressure) for the reservoir to be efficiently beyond the influence of significant capillary forces. Therefore small errors in the depth estimates may produce large differences in HCPV.



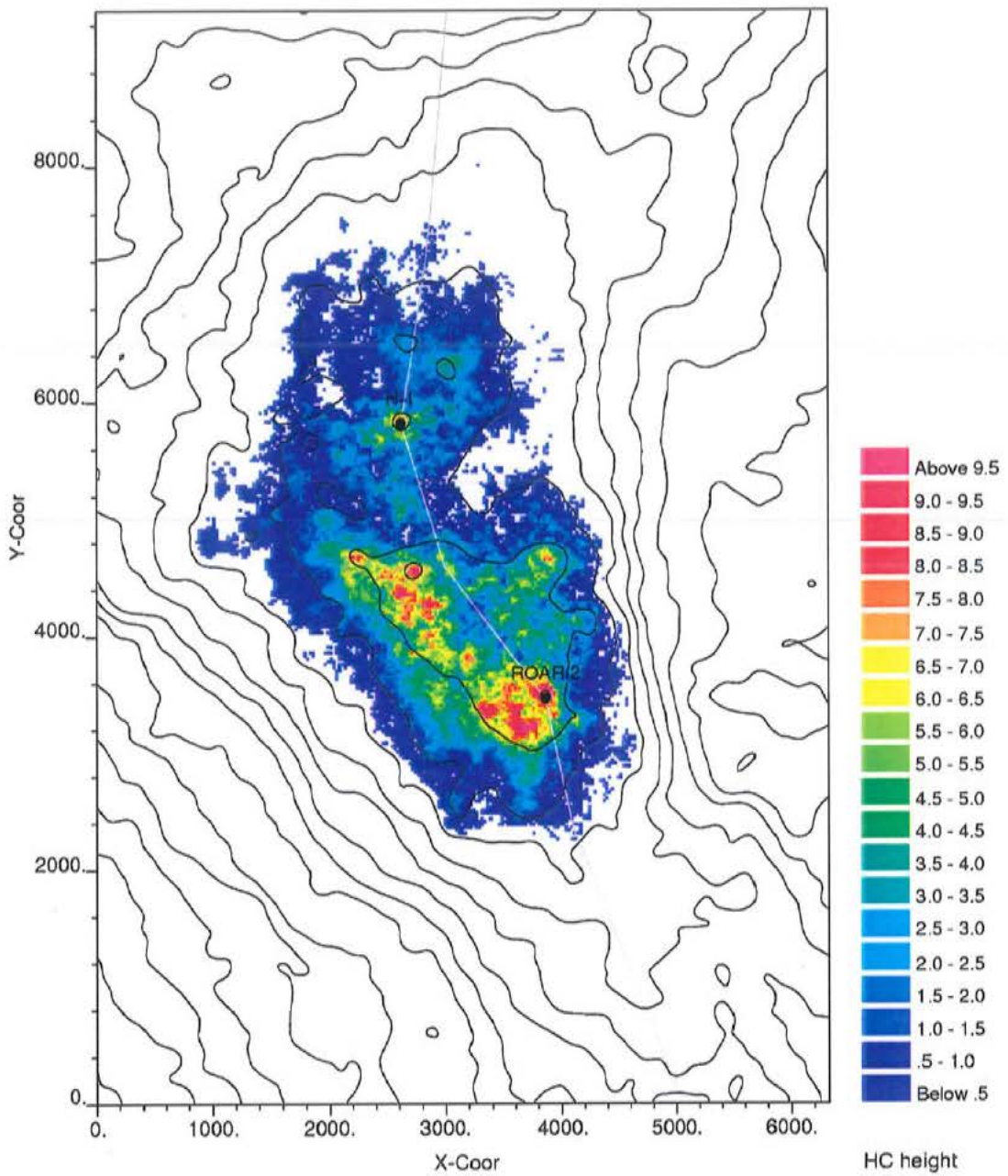


**Figure 55: Map showing a modelled hydrocarbon column in meters. The grey line shows the location of the profile in enclosure 7. Top Chalk depth contours (interval 15m) are also shown (compare Fig. 18).**

## 7. Summary

The Roar Field structure is a gentle low relief inversion chalk anticline with insignificant faulting. The Danian reservoir unit is thin or absent along the northern and eastern edges due to erosion. The erosion might have been initiated by slope instability remobilisation of the Danian chalk. The growth of the structure seems to have started penecontemporaneously with deposition and continued until mid Miocene times with subsequent regional subsidence and tilting. Prior to the tilting, the crestal area of the field is likely to have been shifted slightly to the Southwest, where early invasion of hydrocarbons is suggested to have caused preservation of the abnormally high porosities along the southwest flank of the field and a palaeo fluid contact visible in the seismic data.

The calculated hydrocarbon pore volume is a measure of the uncertainty in the stochastic simulation of the porosity field in the reservoir. This volume amounts to  $20.9 \pm 1.22 \cdot 10^6 \text{ m}^3$ . This small variability in the simulation results is an indication that seismic impedance data (the soft data) are strongly narrowing the solution space. Many steps in the stochastic simulation that are potential sources of increased uncertainty or error were kept as constants. These include the spatial variography and the constructed target populations of both porosity and permeability which due to a very small data base are considered to be very uncertain. Other sources of uncertainty that are kept out of the HCPV calculations include depth conversion velocities, FWL location, GOC location which can cause quite dramatic effects because of the rather modest topography of the field structure.

Contributions to uncertainty that are assumed to be of minor effect are attached to parameters for fluid substitution, and hydrocarbon saturation modelling. The fluid substitution calculation assumes that the porosity estimate obtained from direct porosity inversion (Wagner 1999) are sufficiently accurate for these calculations. It is furthermore assumed that the entire pore-volume shall be substituted from gas to brine in order to obtain the desired impedance unaffected by fluid variations. However, the saturation modelling shows that HC saturations generally are below 50%, especially towards the GOC. The fluid substitution calculation is therefore likely to produce too high impedances after correction, which causes porosity simulations, and thus HC saturation calculations that underestimate the porosities and saturations respectively.

## 8. References:

- Abatzis, I. and Kerr, J. 1989: New spatial visualization techniques in tectonic and stratigraphic interpretation optimize reservoir delineation of the Roar Field, Danish North Sea. 3 p.
- Andersen, C., and Doyle, C. 1990: Review of hydrocarbon exploration and production in Denmark. *First Break*, 8(5), May, 155-165.
- Britze, P., Japsen, P. and Andersen, C., 1995(a): The Danish Central Trough: Top Chalk and the Post Chalk Group. Two-way time and depth, thickness and interval velocity, Geological Survey of Denmark, Map Series, 47, 1:200,000, 2 p., 4 maps.
- Britze, P., Japsen, P. and Andersen, C., 1995(b): The Danish Central Trough: Base Chalk and the Chalk Group Two-way time and depth, thickness and interval velocity. Geological Survey of Denmark, Map Series, 48, 1:200,000, 2 p., 4 maps.
- Deutsch, C. V. and Journel, A. G. 1992: *GSLIB, Geostatistical software library and user's guide*. Oxford University press, New York, 340 p.
- Engstrøm, F. 1995: A new method to normalize capillary pressure curves. *International Symposium of the Society of Core analysts, San Francisco, 1995, SCA no. 9535*, 12p.
- ENS 1996: Oil and Gas Production in Denmark. Annual report. 1996. Danish Energy Agency. Ministry of Environment and energy, 64 p.
- ENS 1997: Oil and Gas Production in Denmark. Annual report. 1997. Danish Energy Agency. Ministry of Environment and energy, 78 p.
- ENS 1998: Oil and Gas Production in Denmark. Annual report. 1997. Danish Energy Agency. Ministry of Environment and energy, 94 p.
- Frykman, P. 1996: Report no. 3. Explorative data analysis of the Dan Field data set. Geological Survey of Denmark and Greenland Report no.25. 260 p.
- Frykman, P. and Deutsch, C. V. 1996: Reservoir modelling of the Dan Field accounting for areal trends and scaling of petrophysical properties. *Joint Chalk Research, Fifth North Sea Chalk Symposium*. 15 p.
- Jacobsen, F., Lieberkind, K. and Nygaard, E. 1982: Reservoir rocks. In Michelsen, O. (ed.): *Geology of the Danish Central Graben. Danmarks Geologiske Undersøgelse, Ser. B, 8*, 92-107.



Journel, A. G., Xu, W., and Tran, T. 1992: Integrating seismic data in reservoir modelling: the collocated cokriging alternative. Stanford Center for Reservoir Forecasting. Report 5, Stanford, 34 p.

Kristensen, L., Dons, T., Maver, K. G. and Schiøler, P., 1995: A multi-disciplinary approach to reservoir subdivision of the Maastrichtian chalk in the Dan Field (Danish North Sea). *Am. Ass. Petr. Geol. Bull.* 79(11).

Kristoffersen, F. Nyhuus, Bang, I. 1982: Cenozoic excl. Danian limestone. In Michelsen, O. (ed.): *Geology of the Danish Central Graben. Danmarks Geologiske Undersøgelse, Ser. B, 8, 62-71.*

Leverett, M. C. 1940: Capillary behaviour in porous solids. *Petroleum Technology*, august, 152-169.

Lieberkind, K., Bang, I., Mikkelsen, N. and Nygaard, E. 1982: Late Cretaceous and Danian Limestones. In Michelsen, O. (ed.): *Geology of the Danish Central Graben. Danmarks Geologiske Undersøgelse, Ser. B, 8, 45-49.*

Lisle, R. J. 1994: Detection of zones of abnormal strains in structures using gaussian curvature analysis. *American Association of Petroleum Geologists Bulletin* 78(12), 1811-1819.

Mavko, G., Chan, C. and Mukerji, T. 1995: Fluid substitution: Estimating changes in Vp without knowing Vs. *Geophysics* 60(6), 1750-1755.

Mavko, G., Mukerji, T., and Dvorkin, J. 1998: *The rock physics handbook.* Cambridge University Press, 329 p.

McCaffery, F. G. 1972: Measurements of interfacial tensions and contact angles at high temperatures and pressures. *The Journal of Canadian Petroleum Technology*, July-September, 26-32.

Megson, J. 1992: The North Sea Chalk Play: examples from the Danish Central Graben. In Hardman, R. F. P. (ed): *Exploration Britain: Geological insights for the next decade.* *Geol Soc. Spec. Publ.*, 67, 247-282.

Munthe, K. L., Omre, H., Holden, L., Damsleth, E., Heffer, K., Olsen, T. S. and Watterson, J. 1993: Sub-seismic faults in reservoir description and simulation. *SPE 26500*, Houston, 8 p.

Nielsen L. H. and Japsen, P. 1991: Deep wells in Denmark 1935-1990. *Danmarks Geologiske Undersøgelse, Series A, 31, 177 p.*

Nygaard, E., Lieberkind, K. and Frykman, P. 1983: Sedimentology and reservoir parameters of the Chalk Group in the Danish Central Graben. - In: J. P. H. Kaasschieter and T. J. A. Reijers (eds.): *Petroleum geology of the southeastern North Sea and the adjacent onshore areas.* (the Hague 1982). - *Geol. Mijnbouw vol. 62, pp. 177-190.*

Thomasen, J. B. and Jacobsen, N. L. 1994: Dipping fluid contacts in the Kraka Field, Danish North Sea. SPE 28435, 763-772.

Vejbæk, O. V. 1995: Stochastic modelling of porosity using seismic impedances on a volume of chalk in the Dan Field. Report to project EFP-95 1313/95-0005. Geological Survey of Denmark and Greenland Report no.61. 45 p.

Vejbæk, O. V. 1996: Annealing cosimulation of Dan Field chalk matrix permeability with simulated porosity. Report to project EFP-95 1313/95-0005. Geological Survey of Denmark and Greenland Report no. 16.,22 p.

Vejbæk, O. V. and Kristensen, L. 1999: Downflank hydrocarbon potential identified using seismic inversion and geostatistics. Upper Maastrichtian reservoir unit, Dan Field, Danish Central Graben. Petroleum Geoscience, xx,xx

Wagner H. 1999: Seismic inversion for acoustic impedance of the Tyra/Roar 3D Marine survey 1992 using the ISIS Software Package. Report 98.661, 87 p. Ødegaard a/s, Copenhagen.

Walls, J. D., Dvorkin, J., and Smith, B. A. 1998: Modeling Seismic Velocity in Ekofisk Chalk. 1998 SEG Expanded abstracts, 4 p.

Xu, W., Tran, T., Srivastava, R. M. and Journel, A. G. 1992: Integrating seismic data in reservoir modelling: the collocated cokriging alternative. paper SPE 24742, 833-842.

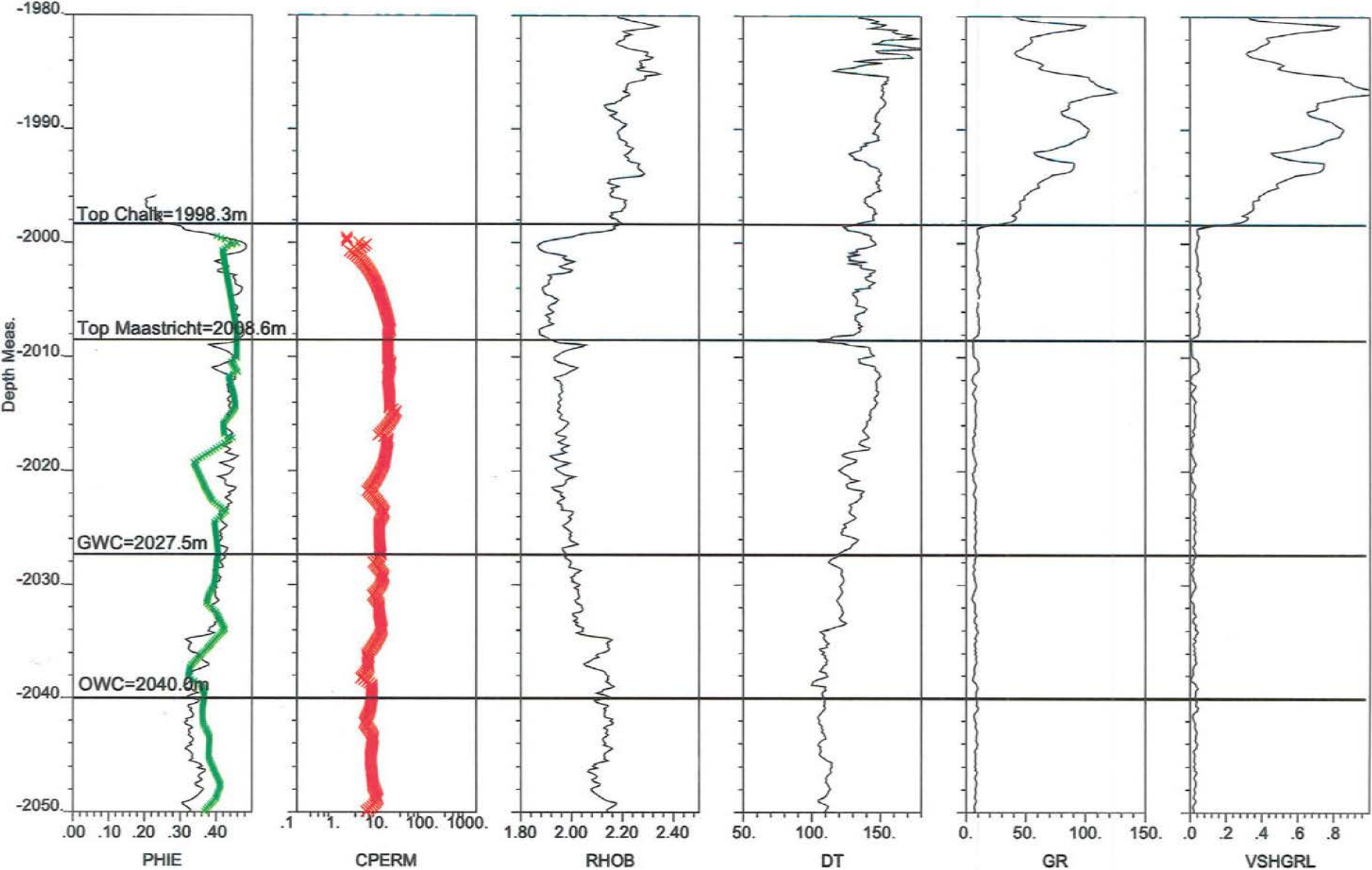
## 9. Enclosures

1. H-1x logs plotted versus depth
2. H-1x logs plotted versus time with synthetic seismograms. Red lines are exact ties, and green lines are the levels picked in the seismic data. Blue traces are from the seismic data and black traces are synthetics.
3. Roar-2 logs plotted versus depth
4. Roar-2 logs plotted versus time with synthetic seismograms. Red lines are exact ties, and green lines are the levels picked in the seismic data. Blue traces are from the seismic data and black traces are synthetics.
5. Top Chalk Depth structure map. Grey box shows the location of the simulation volume. Grey curve shows the intercept between the Top Chalk and the DHI reflector.
6. Top Maastrichtian Depth structure map
7. South to North profile across the field showing seismic impedances, simulated porosity, simulated permeability and modelled hydrocarbon saturation.
8. East west profile across the H-1x well showing seismic impedances, simulated porosity, simulated permeability and modelled hydrocarbon saturation.
9. East west profile across the Roar-2 well showing seismic impedances, simulated porosity, simulated permeability and modelled hydrocarbon saturation.
10. Colour coding for enclosures 7, 8, and 9.
11. Example of Porosity simulation parameter file
12. Example of permeability simulation parameter file



WELL: H-1X 603303.8 6182306, KB=122.050'

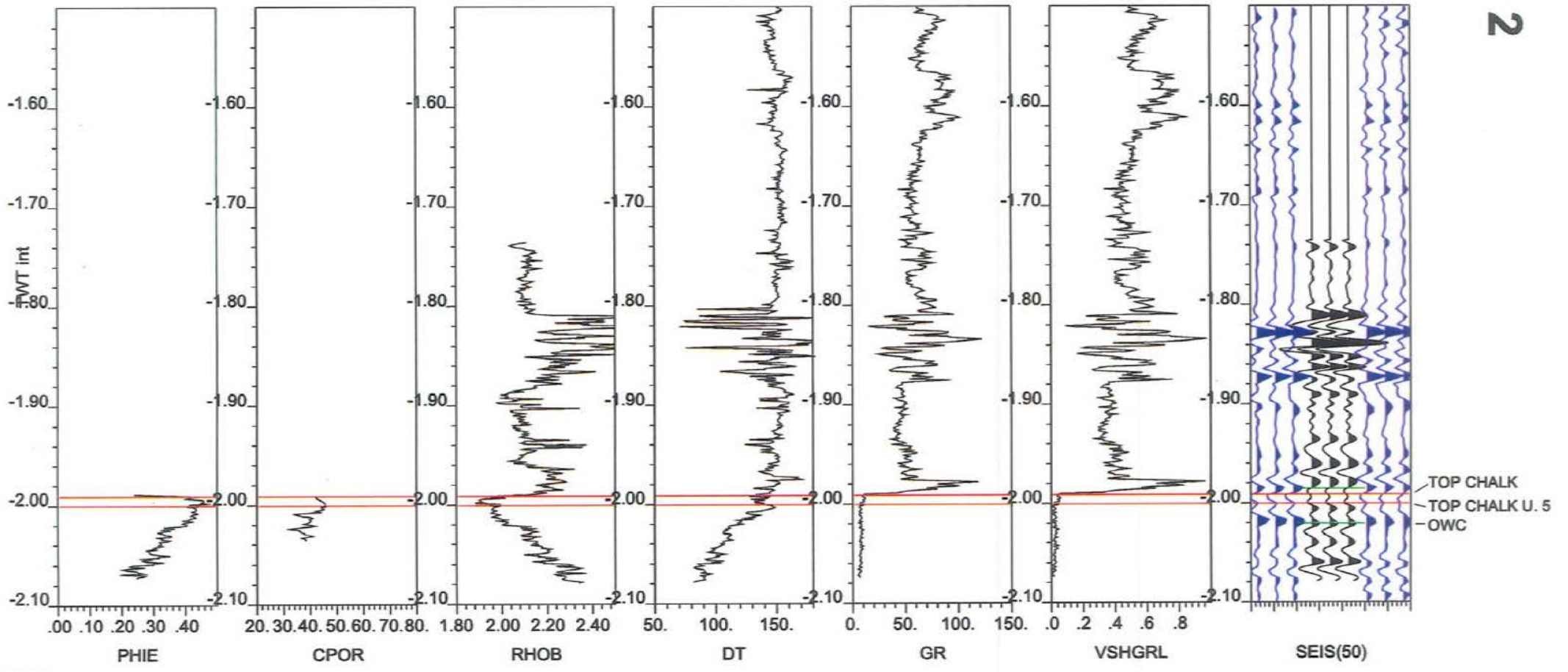
H-1X.LAS



9.1 Enclosure 1

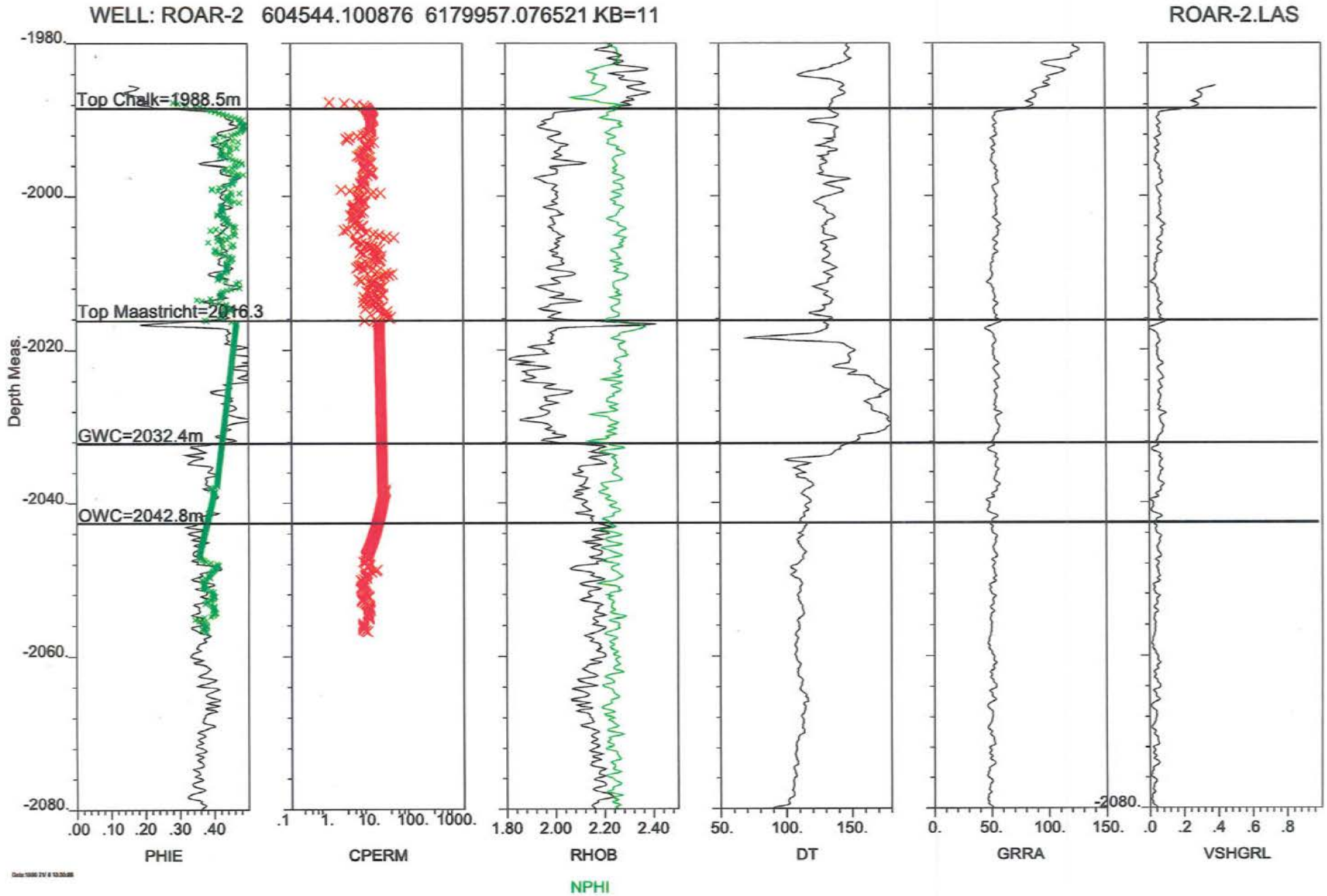
# 9.2 Enclosure 2

WELL: H-1X 603303.8 6182306, KB=122.050'



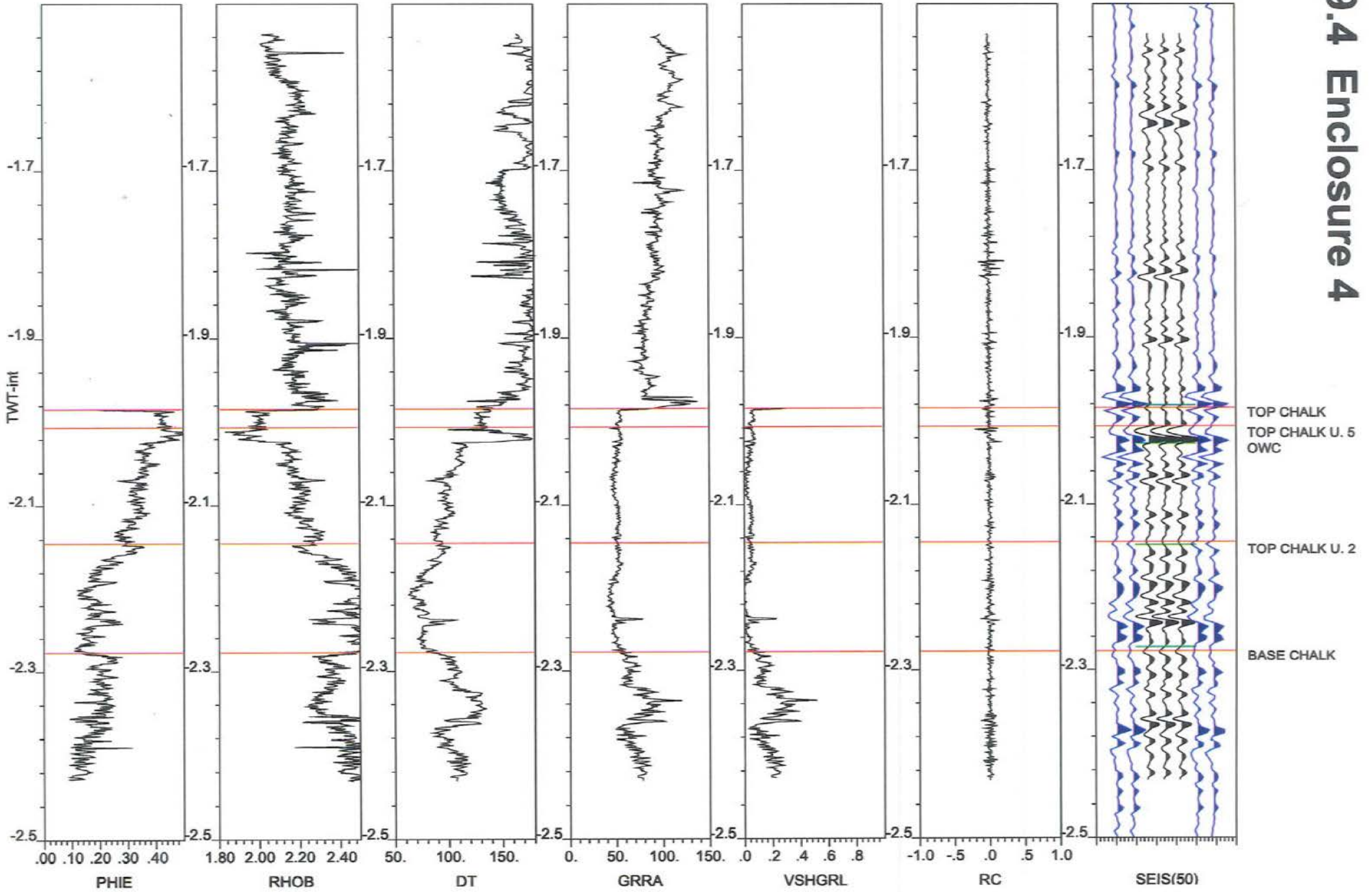
04/08/2010 08:23:28

# 9.3 Enclosure 3



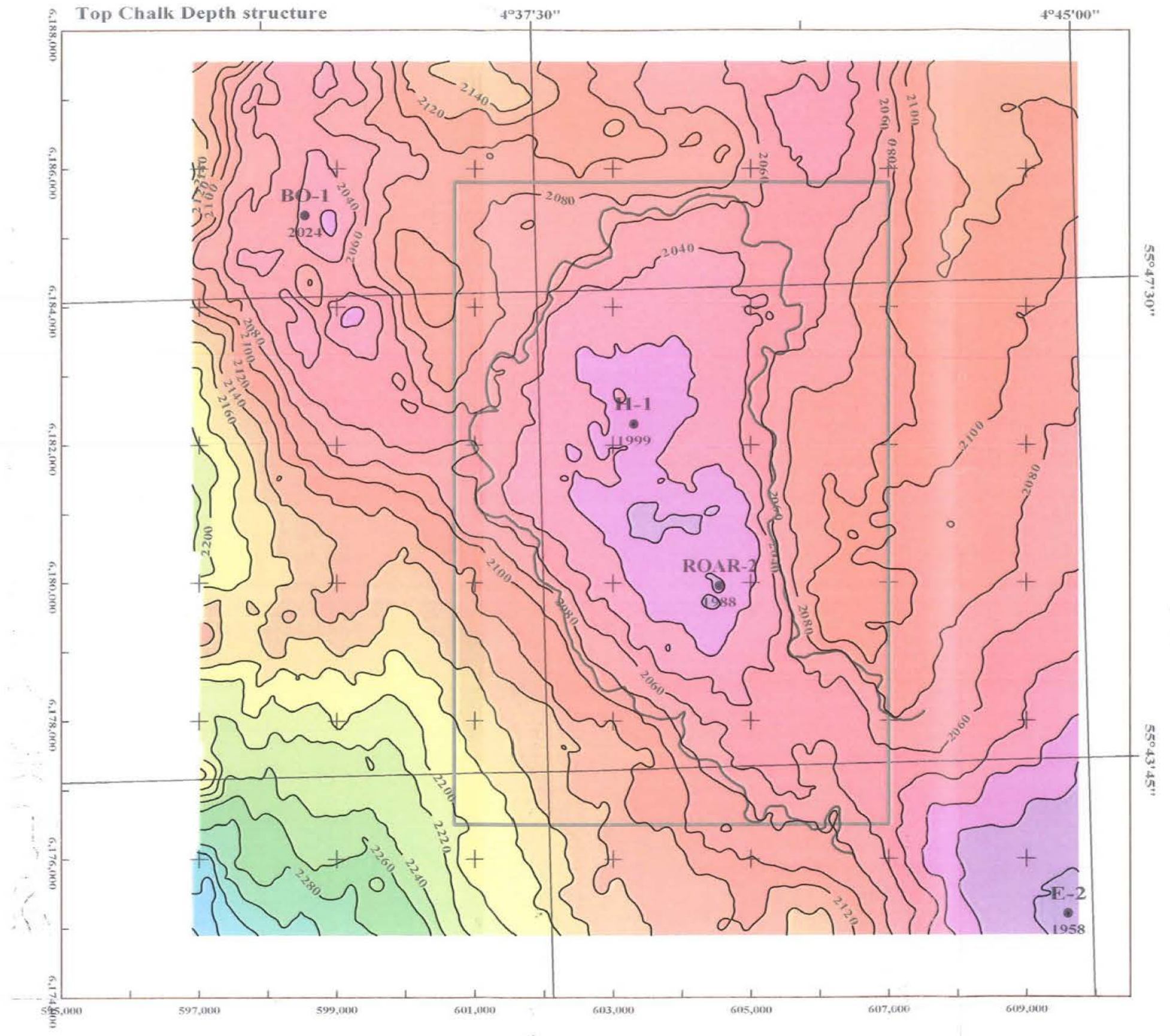


WELL: ROAR-2 604544.1, 6179957.1 1.16'



# 9.4 Enclosure 4

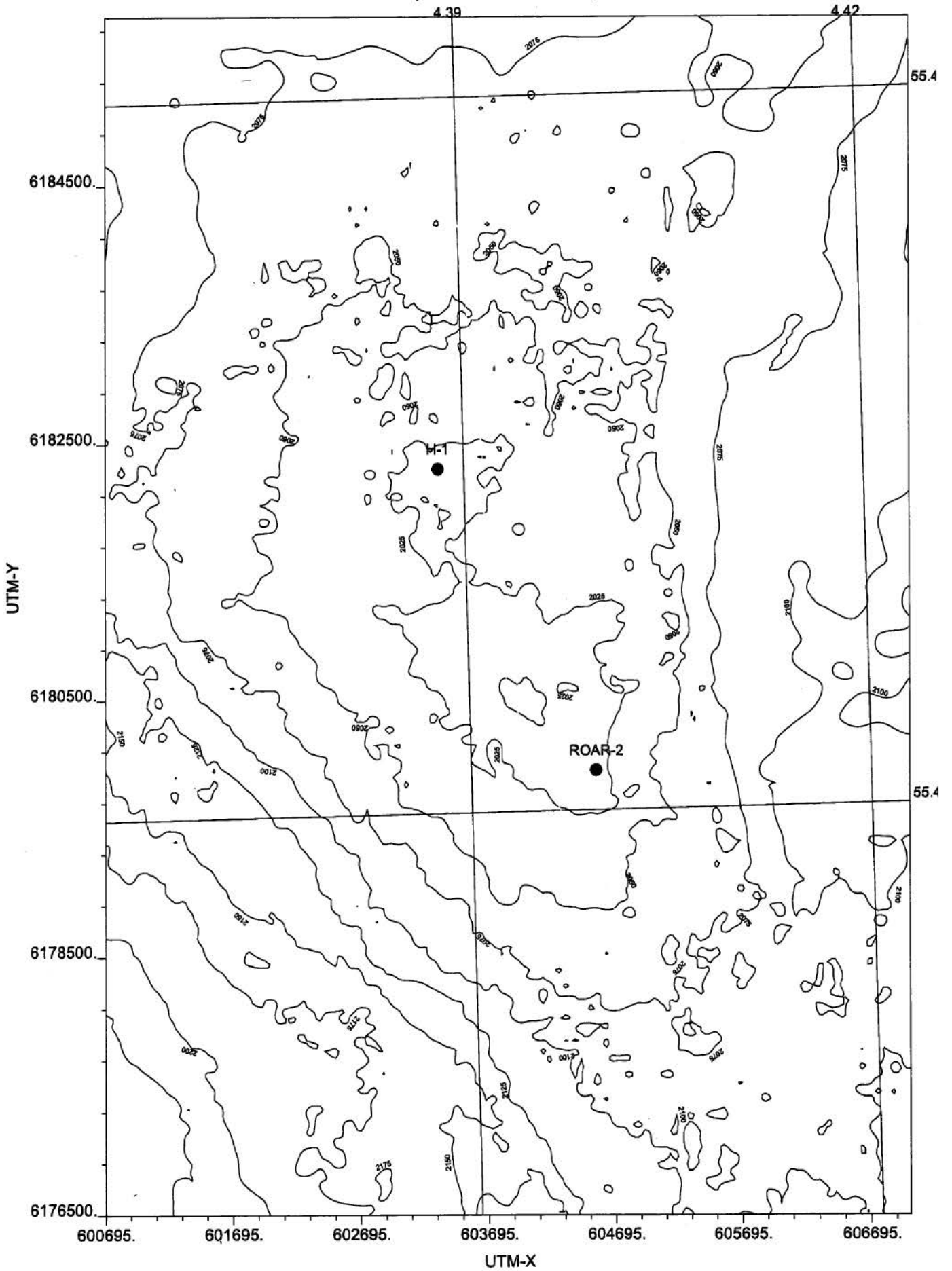
9.5 enclosure 5



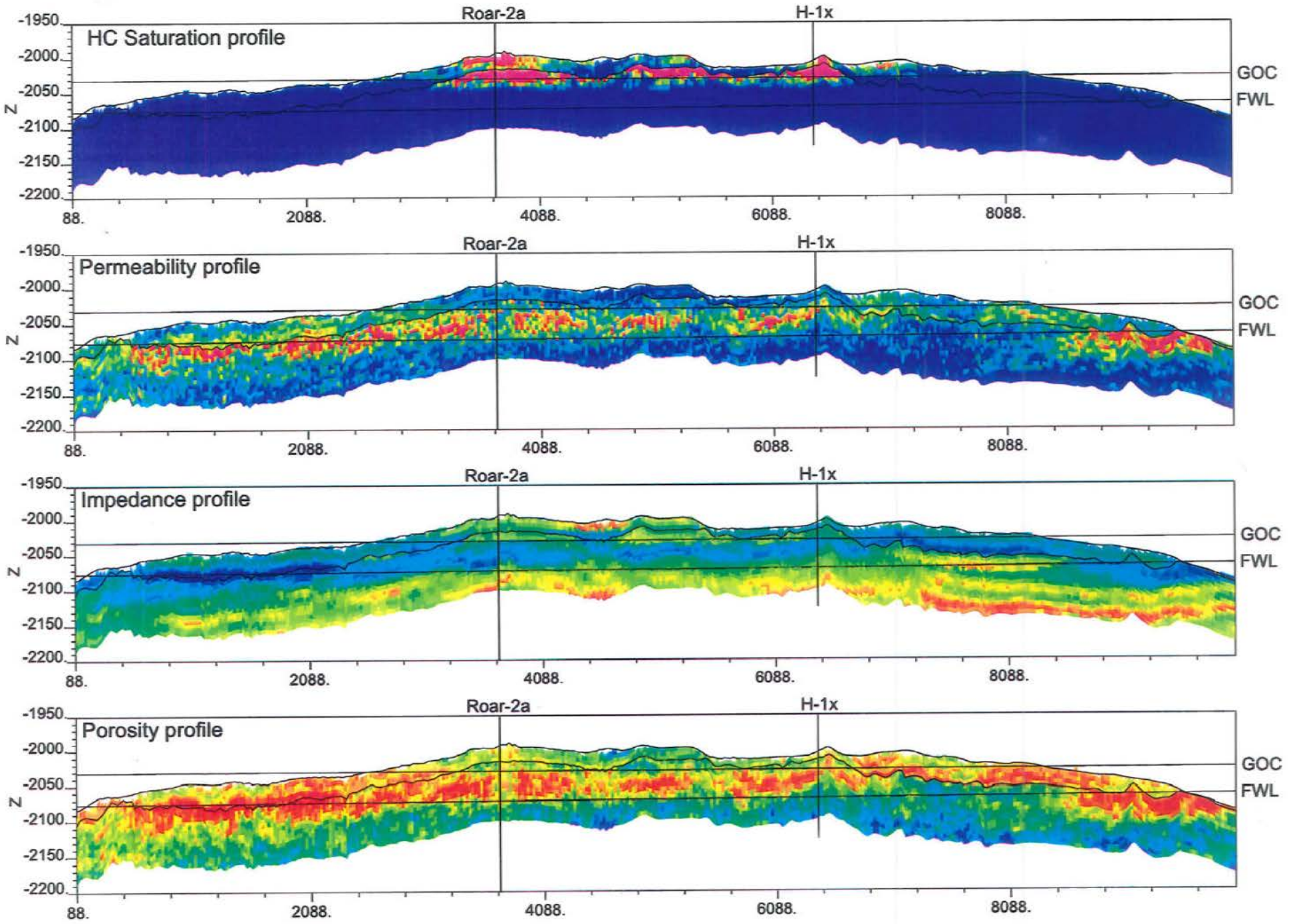


# 9.6 Enclosure 6

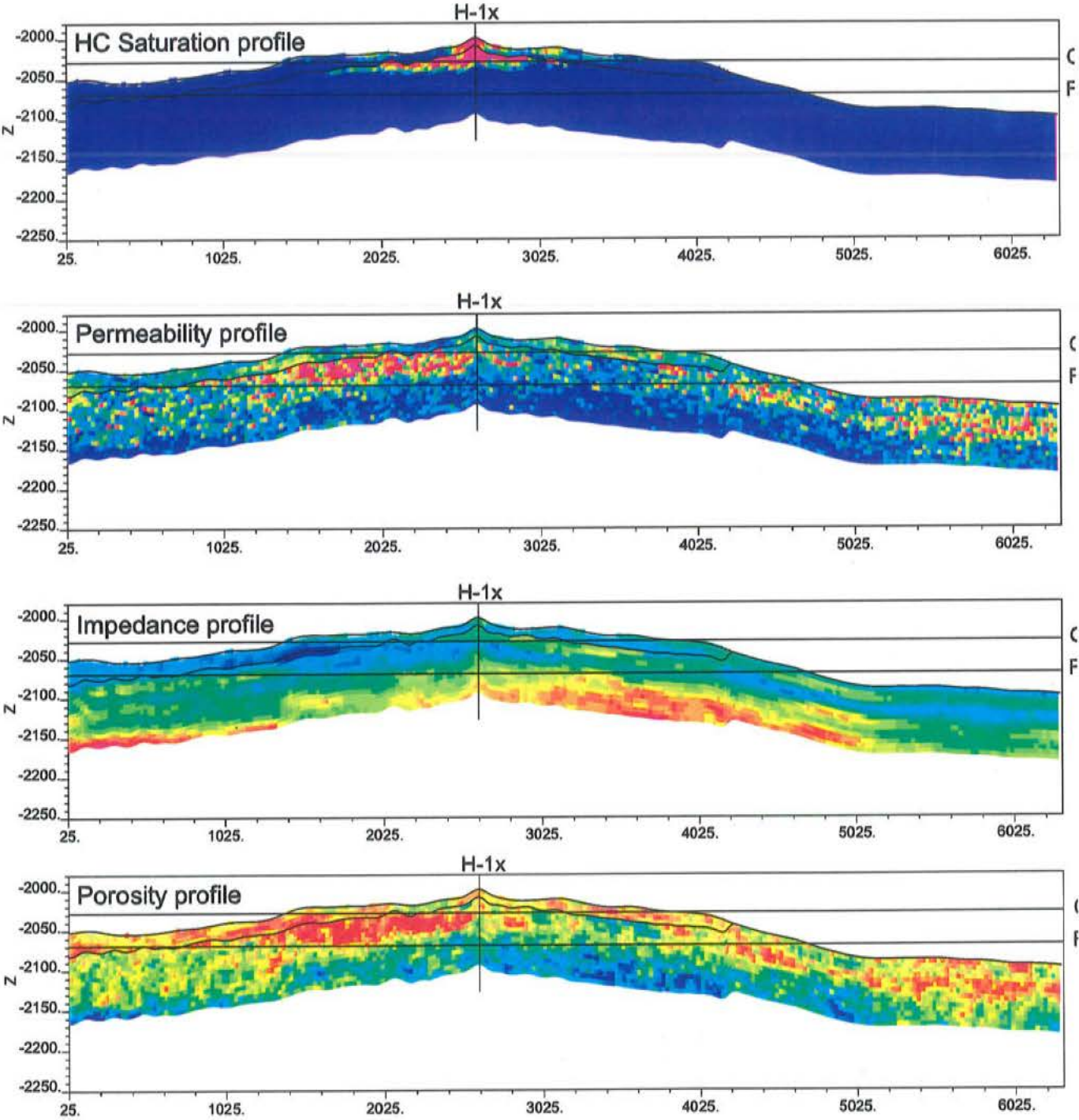
Top Maastrichtian depth





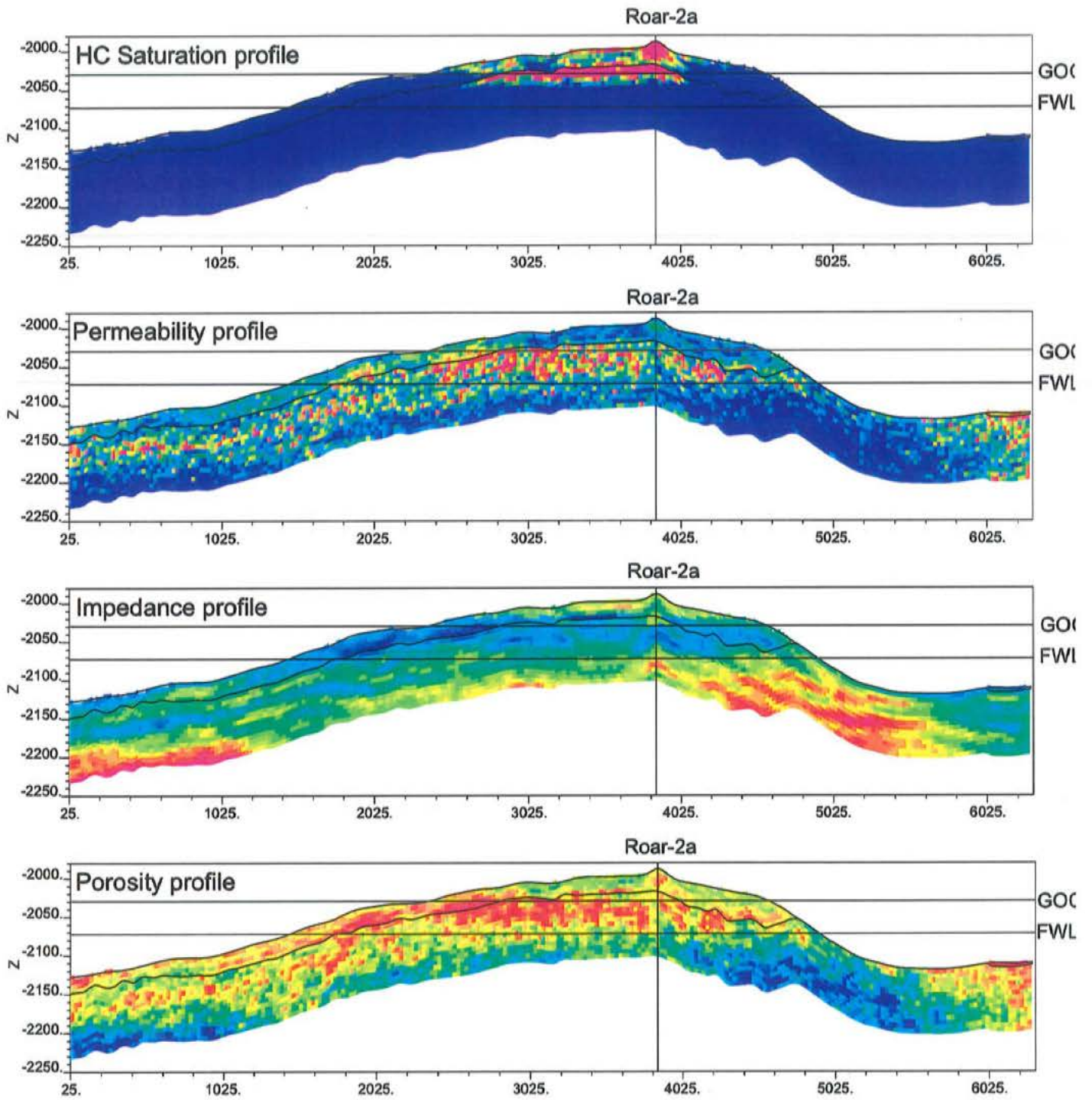


# 9.8 Enclosure 8

























# 9.9 Enclosure 9





## 9.10 Enclosure 10

### Colour scale translation

	Above 19.	Above .48	Above 7300.	Above .55
	18. - 19.	.45 - .48	7100. - 7300.	.52 - .55
	17. - 18.	.43 - .45	6900. - 7100.	.50 - .52
	16. - 17.	.40 - .43	6700. - 6900.	.48 - .50
	15. - 16.	.38 - .40	6500. - 6700.	.45 - .48
	14. - 15.	.35 - .38	6300. - 6500.	.43 - .45
	13. - 14.	.33 - .35	6100. - 6300.	.41 - .43
	12. - 13.	.30 - .33	5900. - 6100.	.38 - .41
	11. - 12.	.28 - .30	5700. - 5900.	.36 - .38
	10. - 11.	.25 - .28	5500. - 5700.	.33 - .36
	9. - 10.	.23 - .25	5300. - 5500.	.31 - .33
	8. - 9.	.20 - .23	5100. - 5300.	.29 - .31
	7. - 8.	.18 - .20	4900. - 5100.	.26 - .29
	6. - 7.	.15 - .18	4700. - 4900.	.24 - .26
	5. - 6.	.13 - .15	4500. - 4700.	.22 - .24
	4. - 5.	.10 - .13	4300. - 4500.	.19 - .22
	3. - 4.	.08 - .10	4100. - 4300.	.17 - .19
	2. - 3.	.05 - .08	3900. - 4100.	.15 - .17
	1. - 2.	.03 - .05	3700. - 3900.	.12 - .15
	Below 1.	Below .03	Below 3700.	Below .12
	mDarcy	So (frac.)	Impedance	Porosity

## 9.11 Enclosure 11

Porosity simulation parameter file:

Gaussian Sequential Simulation  
\*\*\*\*\*

```

START OF PARAMETERS:
danwell.blk          \Data File in GEOEAS format
1 1                  \Number of hard and soft var.
1 2 3 9 7 0         \column: x,y,z,vhard(i),wt
1                    \0=transform the data, 1=don't
hard.trn             \Transf. table(for each var.)
-99.0 9999.0         \min./max. val.(missing) for var.1
-4.6737 4.6737      \Min. and Max. val. for tails (Nscore val)
1 1.50              \Lower tail option and parameter
1 0.5               \Upper tail option and parameter
sgcosim.out          \Output File for simulation
1                    \Debugging level: 1,2,3
sgcosim.dbg          \Output File for Debugging
52027                \Random number seed
impdan2.oub          \Gridded Secondary Variable
2                    \columns for soft variables (Nscore val.)
sgcosim.cal          \Calibration parameter file
1                    \Number of simulations
253 12.5 25.0        \nx,xmn,xsiz
373 12.5 25.0        \ny,ymn,ysiz
11 3.0 6.0           \nz,zmn,zsiz
1                    \0=two part search, 1=data-nodes
0                    \max per octant (0 -> not used)
2000.0              \maximum search radius
0.0 0.0 0.0 1.0 0.02 \sang1,sang2,sang3,sanis1,sanis2
0 8                 \min, max data for simulation
12                  \number simulated nodes to use
2 0.0               \nst, nugget effect VARIAB. 1
1 180.0 0.476       \it,aa,cc: STRUCTURE 1
90. 0.0 0.0 1.0 0.06 \ang1,ang2,ang3,anis1,anis2:
2 1700.0 0.524      \it,aa,cc: STRUCTURE 2
90.0 0.0 0.0 1.0 0.06 \ang1,ang2,ang3,anis1,anis2:

```

The calibration parameter file (sgcosim.cal):

```

Correlation coefficient matrix
2
Porl
Impedances
1.0 -0.45
    1.0

```

## 9.12 Enclosure 12

Permeability simulation parameter file:

Gaussian Sequential Simulation  
\*\*\*\*\*

START OF PARAMETERS:

```
DANwell.PER          \Data File in GEOEAS format
1 1                  \Number of hard and soft var.
1 2 3 7 0           \column: x,y,z,vhard(i),wt (Nscore val.)
1                    \0=transform the data, 1=don't
hard.trn             \Transf. table(for each var.)
-99.0 9999.0         \min./max. val.(missing) for var.1
-4.67369 4.67369    \Min. and Max. val. for tails (Nscore val.)
1 1.50              \Lower tail option and parameter
1 0.5               \Upper tail option and parameter
SGDAPE2.out          \Output File for simulation
1                    \Debugging level: 1,2,3
sgcosim.dbg          \Output File for Debugging
111068              \Random number seed
SGCOSI2.out          \Gridded Secondary Variable
1                    \columns for soft variables (Nscore val.)
sgcosim.cal          \Calibration parameter file
1                    \Number of simulations
253 12.5 25.0        \nx,xmn,xsiz
373 12.5 25.0        \ny,ymn,ysiz
11 3.0 6.0           \nz,zmn,zsiz
1                    \0=two part search, 1=data-nodes
0                    \max per octant (0 -> not used)
2000.0              \maximum search radius
0.0 0.0 0.0 1.0 0.02 \sang1,sang2,sang3,sanis1,sanis2
0 8                  \min, max data for simulation
12                  \number simulated nodes to use
2 0.0                \nst, nugget effect VARIAB. 1
1 60.0 0.476         \it,aa,cc: STRUCTURE 1
90. 0.0 0.0 1.0 0.06 \ang1,ang2,ang3,anis1,anis2:
2 566.0 0.524       \it,aa,cc: STRUCTURE 2
90.0 0.0 0.0 1.0 0.06 \ang1,ang2,ang3,anis1,anis2:
```

The calibration parameter file (sgcosim.cal):

```
Correlation coefficient matrix
2
Por1
Impedances
1.0 0.45
    1.0
```